METHYL ELIMINATION CHANNEL OF THE PHOTODISSOCIATION OF ALLYL RADICAL: SEMI-CLASSICAL SIMULATION AND VELOCITY-MAP-IMAGING

A Dissertation

Presented to the Faculty of the Graduate School

of Cornell University

in Partial Fulfillment of the Requirements for the Degree of

Doctor of Philosophy

by

David Yokdiong Lee

August 2011

METHYL ELIMINATION CHANNEL OF THE
PHOTODISSOCIATION OF ALLYL RADICAL:
SEMI-CLASSICAL SIMULATION AND VELOCITY-MAP-IMAGING

David Yokdiong Lee, Ph.D.
Cornell University 2011

Allyl radical is one of the most important stable radicals in the study of hydrocarbon combustion chemistry. Most of the competing dissociation channels for allyl radicals excited with a specific internal energy yield atomic or molecular hydrogen. Little was known about the methyl elimination channel, except its contribution of ~ 10% to the total yield, until recent time-of-flight study (*J. Chem. Phys.* **128**, 151101, 2008) revealed unusual product energy distribution which violated the RRKM prediction. In this thesis methyl products with specific internal energy were experimentally investigated by velocity-map-imaging of photolytically generated allyl with rotational temperature below 20 K. An anisotropic angular distribution of the the methyl product was observed from dissociation of this cold allyl radicals, in contrast to previous studies starting with pyrolytically generated allyl radicals. The source of the unusual methyl product energy distribution was investigated by classical trajectory simulation on an ab-initio potential energy surface of the ground electronic state of allyl. This theoretical study revealed a new high energy transition state with vinylidene, $H_2C{=}C$, as the intermediate that accounts for the observed energy distribution.

BIOGRAPHICAL SKETCH

I came to the United States from Taiwan as a high school senior in 1997. After earning my B.S. degree in chemistry and M.S. degree in synthetic organic chemistry from the Rochester Institute of Technology, I entered the graduate school of Cornell University in 2003. Soon after realizing my passion to pursue advanced studies in organic chemistry had faded away, I joined the Paul Houston research group in 2004 and started learning how to work with high vacuum chambers, optics, molecular beams and lasers. I had solid training in experimental physical chemistry in the following years at Cornell and was also given an opportunity to do research in molecular dynamics simulations at the CCMR computing facility. 2008 was a tough year for the Houston group members as Paul became the Dean of Science of Georgia Institute of Technology. We at last survived in moving all the chambers, pumps and lasers and made good progress in collecting experimental and computational data here in Atlanta. Although the relocation might have delayed my graduation, it provided me a valuable opportunity in designing and assembling an experimental research facility that I for sure will be benefited in the future. After earning my Ph.D. degree I will join the Alex Kandel group as a postdoctoral research associate at the University of Notre Dame working on the gas-surface reactions using molecular beams and scanning tunneling microscopy.

This document is dedicated to my grandfather and grandmother,

黃金水 先生　及　黃林彩桑 女士 .

ACKNOWLEDGEMENTS

I profoundly thank my thesis advisor, Prof. Paul L. Houston, for the guidance through my entire graduate study. Immediately after I joined the group, we held meetings every week for just two of us discussing basic sciences and research ideas that sped up my learning process a lot. He always made himself available whenever we would like to discuss research, even through the internet when he was in sabbatical. As much as I have tried to come up with all the possible solutions for each problem we encountered, he could always think of a better solution or provide me with a totally different perspective. The allyl project he assigned to me was very challenging but gave me an invaluable training in both experimental and theoretical physical chemistry.

I also thank research scientists of the Houston group, Dr. Mark Lambert and Dr. Jun Chen, for teaching me mostly everything and helping me solve all of the technical problems in the laboratory. I am grateful to Prof. Gregory Ezra for helping me learn molecular symmetry and spectroscopy through the difficult book by Bunker and Jensen, without such knowledge the last part of this thesis could never have been written. I acknowledge many beneficial research discussions with Prof. H. Floyd Davis in joined group meetings. Finally I say thanks to Mr. Benjamin Stangfeld for countless days of working (and struggling) together in the lab.

TABLE OF CONTENTS

LIST OF TABLES

LIST OF FIGURES

CHAPTER 1

INTRODUCTION

1.1 Background

Resonantly stabilized, unsaturated hydrocarbon radicals have received great attention in combustion chemistry research due to their abilities to form polycyclic aromatics, which eventually might lead to the formation of soot. The simplest among them are propargyl ($C_3H_3\bullet$) and allyl ($C_3H_5\bullet$) radicals that can form aromatics in only one bimolecular step.[1,2] As a result of their relative high thermal stability and their slow reaction with molecular oxygen, these radicals can build up high concentrations in combustion systems under fuel-rich conditions.[3] The apparent relative stabilities of allyl and propargyl radicals vary according to the particular reaction studied; however, measurements of bond dissociation energies and rates of decomposition of their peresters (allyl-COOOR or propagyl-COOOR) indicated that allyl radicals are somewhat more stable than propagyls.[4] Allyl itself is also a particularly important intermediate in propane (C_3H_8), butane (C_4H_{10}), butene (C_4H_8) and some dialkene-rich flames.[5,6] In the fundamental research of combustion chemistry, we would like to understand how the substance of interest in the fuel responds (especially dissociates) in a burning flame (or when being excited with certain amount of energy), and consequently what the products (specifically, dissociated fragments) are formed and how they are formed (the product energy and spatial distribution). Data on the unimolecular dissociation of allyl helps predict its kinetic models which are sensitive to the rates of producing atomic and molecular hydrogens and methyl radicals in the combustion reactions.

The electronic ground state allyl radical is a planar asymmetric top molecule belonging to the C_{2v}(M) molecular symmetry (MS) group. Adopting the Mulliken II^r convention, the three principal axes (a, b, c), which coincide with the molecular fixed axes (x, y, z), are assigned such that if the molecule is oriented in the yz plane, *z(b)* is along the central C-H bond, *x(c)* can be chosen pointing either out or in to the plane, and then *y(a)* is assigned by the right-hand-rule of $z(\vec{b}) \times x(\vec{c})$. Based upon the simple molecular orbital theory, there is a bonding b_1 orbital, a nonbonding a_2 orbital, and an antibonding b_1* orbital in the π-orbitals of the ground electronic state. The ground electronic configuration is (doubly occupied σ orbitals)$(b_1)^2(a_2)$, which gives an $\widetilde{X}\ ^2A_2$ state. The geometry of this ground state, along with the three equilibrium rotational constants A_e = 1.801769 cm^{-1}, B_e = 0.3463440 cm^{-1}, and C_e = 0.2902374 cm^{-1}, was determined by high-resolution IR spectroscopy on the ν_1, ν_{11}, and ν_{13} fundamentals.[7,8] The C_{2v}(M) symmetry was also confirmed by the nuclear spin statistics on the intensity variation of the rotational transitions on the IR spectra.[8] The degree of asymmetry κ = ($2B_e$ - A_e - C_e)/(A_e - C_e) ≈ - 0.93 indicates that this ground state structure can be approximately treated as a near-prolate symmetric top molecule.

The absorption spectrum of the allyl $\widetilde{A}\ ^2B_1 \leftarrow \widetilde{X}\ ^2A_2$ transition was first observed by Currie and Ramsay[9] in the 380 nm to 410 nm region. Chen and coworkers later reported rotational simulations and dissociation dynamics of this $\widetilde{A}\ ^2B_1$ state.[10] Hudgens and Dulcey were the first to observe the one-photon forbidden $\widetilde{B}\ ^2A_1 0_0^0 \leftarrow \widetilde{X}\ ^2A_2$ transition at 249.5 nm by 2 + 2 resonance enhanced multi-photon ionization (REMPI),[11] and this assignment was later confirmed by two other groups.[12,13] Allyl absorption in the 250 nm to 210 nm region was first measured by Callear and Lee without assignment,[14] and the strong one-photon

allowed transition at 248.14 nm was later assigned by the Chen group in 1992 to be the $\widetilde{C}\ ^2B_1 0^0$ state.[15] Recently in 2009, the Chen group re-investigated this transition by employing the 1+1 REMPI, UV/UV electronic ground state depletion and pulsed-field-ionization zero-kinetic-energy photoelectron (PFI-ZEKE) spectroscopy on allyl radicals produced by flash pyrolysis of 1,5-hexadiene and 266 nm photolysis of allyl iodide.[16,17] The photolytic production of allyl showed a significantly different spectrum from the pyrolytic one, and pyrolysis was the method of generating allyl radicals in all of their previous publications. Rotational temperature of T_{rot} = 264 K for pyrolysis and T_{rot} = 5.5 K for photolysis gave the best simulation to the experimental data (Fig. 1.1). They re-assigned this 248.14 nm transition to be $\widetilde{B}\ 12_0^1 \leftarrow \widetilde{X}$ with $\nu = 12$ being the conrotatory twist of the terminal methylene groups, and 240.58 nm to be the true one-photon $\widetilde{C}\ ^2B_1 0_0^0 \leftarrow \widetilde{X}$ transition. The transition from the vibrationless electronic ground state with $\Gamma_{ve}'' = A_2$ to the $\widetilde{B}\ 12^1$ vibronic state with $\Gamma_{ve}' = \Gamma_v' \otimes \Gamma_e' = B_1 \otimes A_1 = B_1$ is one-photon allowed, which might be the reason why people have mistakenly assigned this to be the $\widetilde{C}\ ^2B_1 0_0^0 \leftarrow \widetilde{X}$ transition. The experimental spectrum in Fig. 1.1(a) has a dominant strong central peak and fairly weak wings that implicates a *Type a* transition. Using the symmetry of the two vibronic states and the C_{2v}(M) MS character table,[18] we have $\Gamma_{ve}' \otimes \Gamma_{ve}'' = B_1 \otimes A_2 = B_2 \supset \Gamma(\mu_a)$, indicating that the transition moment is along the *y(a)* axis. Indeed, simulation as a *Type a* band was most consistent with the observed structure.

The first photodissociation study on allyl was performed by Stranges *et al*[19] who used molecular beam photofragment translational spectroscopy to examine products following UV excitation of allyl radicals by 248 and 351 nm photons. Two primary channels were detected following the 248 nm excitation: H-atom loss (84%) and CH_3 elimination (16%). Based on the energy release,

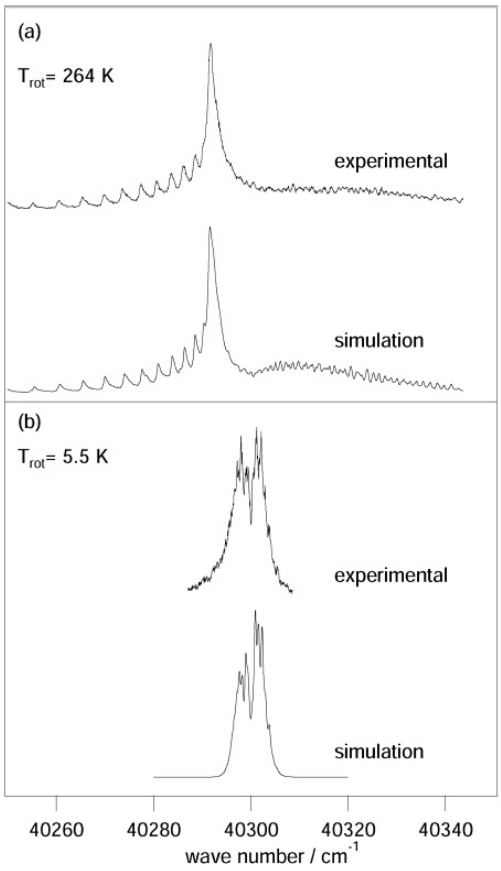

Figure 1.1: The 1+1 REMPI spectra of the 248.14 nm vibronic transition of the allyl radical and a simulation of the absorption spectrum for (a) T_{rot} = 264 K and (b) T_{rot} = 5.5 K.[16]

the authors proposed that the CH_3 was eliminated directly from a four-member cyclic transition state. Since then nearly all studies on photodissociation of allyl focused on the H elimination channel from different eletronic excited states of allyl, and most results were contributed by the Chen group. A review article published in 2002[6] summarized their work performed on allyl by various laser techniques (including multiphoton ionization, time and frequency resolved spectroscopy of reaction products, photoelectron and ZEKE spectroscopy) and described a comprehensive picture of the processes occurring in allyl upon photoexcitation, along with references to their prevously published articles.

1.2 Purpose of Research

Not very much attention has been paid to the methyl elimination channel of the dissociation of allyl since the publication of Chen's review article in 2002. This thesis research follows the experiment performed in collaboration between the Houston group of Cornell and the Stranges group at the University of Rome in 2007.[20] After being given 115 kcal/mole (248nm) in energy by a KrF excimer laser, allyl radicals are excited to the $\widetilde{B}$ electronic state, followed by internal conversion in about 22 ps to the $\widetilde{X}$ ground electronic state.[21] There are six thermochemically accessible product channels for allyl with this amount of energy: three give H-atom and various hydrocarbons (cyclopropene, allene, and propyne), two give H_2 and cyclopropenyl or propargyl, and one gives methyl with acetylene (Fig. 1.2).[22] The focus of the experiment performed in Rome was on the methyl elimination channel which, as shown by quantum mechanical calculations,[20,23] can occur by two mechanisms with the same intermediate, 1-propenyl CH=CH-CH_3 (between states A and B; between states D and E, in Fig. 1.3). In the first mechanism, a 1,3 hydrogen shift takes place to give 1-propenyl, which then dissociates to yield CH_3 + HCCH. In the other mechanism, designated as double-1,2 hydrogen shifts, CH_2-C-CH_3 first forms, followed by rearrangement into 1-propenyl, then finally dissociates to give CH_3 + HCCH.

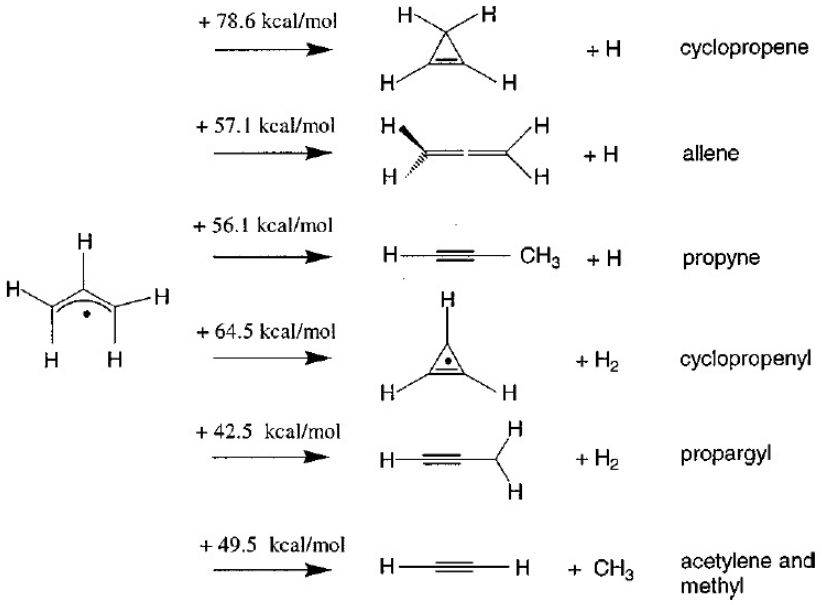

Figure 1.2: Possible reaction channels thermochemically accessible for the allyl radical at an energy of 115 kcal/mole together with their standard heats of formation relative to allyl.[22]

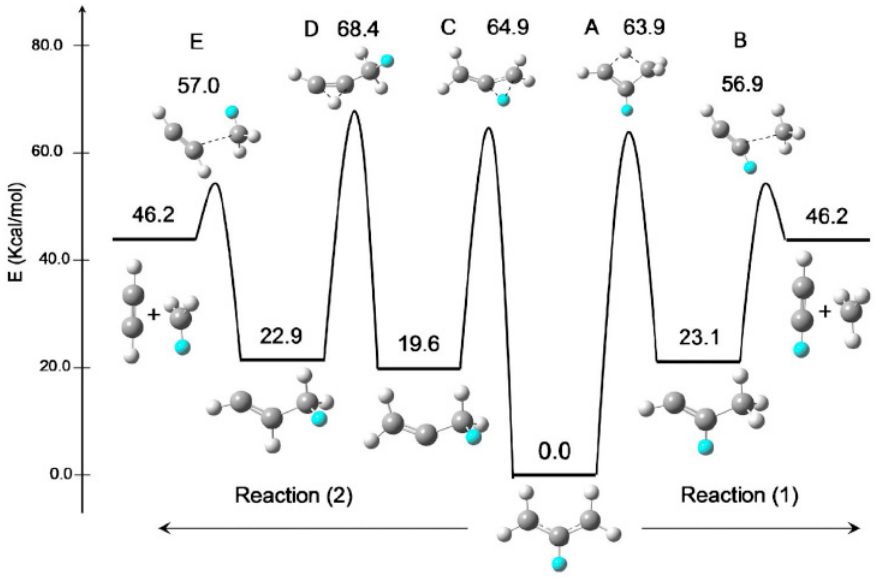

Figure 1.3: Potential energy barriers describing the 1,2 and 1,3 H/D atom shift mechanisms and C-C bond breaking channels in the CH_2CDCH_2 system with D-atoms colored.[20]

As shown in Fig. 1.3, deuterating the central hydrogen atom helps distinguish the two methyl elimination paths. The apparatus in Rome consisted of an electron impact ionization region, a quadrupole mass spectrometer, and a "door knob" detector assembly. Fig. 1.4 shows the arrival time distributions for DCCH and HCCH as well as the translational energy distributions for the two product mechanisms from the deuterated allyl. The $P(E_{trans})$ distributions for the two mechanisms were successfully used to simulate the HCCH arrival time distribution from the non-deuterated allyl (Figure 1.5), and to calculate (see ref. 20 for the detailed procedure) the branching ratios of the two mechanisms. For the deuterated allyls the branching ratio of the two mechanisms was BR_D = (1)/(2) = 1.6 ± 0.1. For the non-deuterated allyls, BR_H = 1.0 ± 0.1. However, the closest (by adjusting potential barrier heights in Fig. 1.3 within their individual uncertainties) ratios predicted by the Rice-Ramsperger-Kassel-Marcus (RRKM) theory were BR_D = 3.76 and BR_H = 2.2. This result was surprising because both pathways go through the same intermediate, and the RRKM theory assumes complete randomization in energy in any potential well regardless of previous paths to reach there,[24] so that one would expect the two isotopically different products to have nearly the same kinetic energy distribution. The disagreement between the measured ratios and the ones predicted by the RRKM theory was the starting point of the theoretical part of this research project.

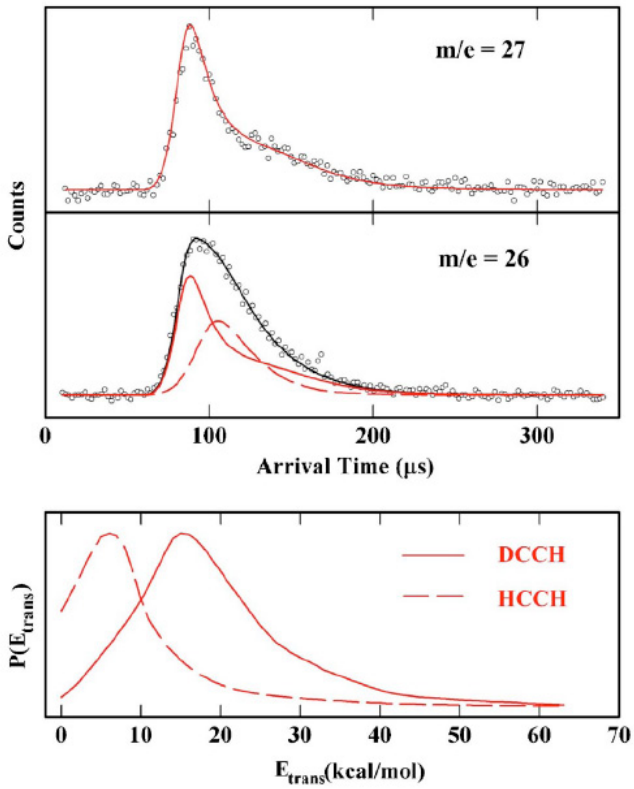

Figure 1.4: Arrival Time and P(E_{trans}) distributions for DCCH and HCCH. In the arrival time distribution for HCCH, the total signal is composed of two components, one from cracking of DCCH and one from production of HCCH. The arrival time data is shown for scattering at 15°, whereas the P(E_{trans}) distributions are based on data collected at all angles and are normalized to unit area.[20]

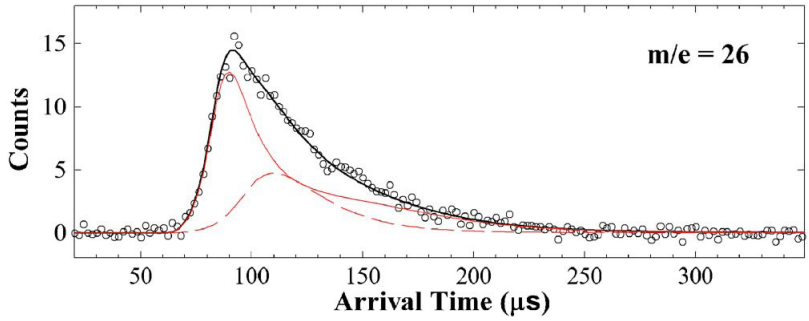

Figure 1.5: Arrival time distribution of m/e=26 ions taken at laboratory angle of 15° following photodissociation of the H_2CCHCH_2 radical. The full line shows the contribution of the reaction(1) while the dotted line shows that of reaction(2) of Fig. 1.3. The P(E_{trans}) distributions used in the simulations are those shown in Fig. 1.4.[20]

1.2.1 VMI vs. TOF

The time-of-flight apparatus in Rome could not distinguish between methyl radicals with different internal energies. Based on the change of geometry from pyramidal to planar, it was reasonable to expect the methyl radicals to have vibrational energy in the out-of-plane "umbrella" bending mode ($v = 2$). Methyl radicals are detected in this velocity-map-imaging project by resonance-enhanced multi-photon ionization (REMPI), and the 2+1 REMPI spectra for vibrational states v = 0, 1, 2 in the umbrella mode have already been previously determined by our group (Fig. 1.6).[25] Another improvement in this imaging project is the production of allyl radicals. As mentioned before in previously photodissociation studies,[6,19,20] allyl radicals were produced pyrolytically and were ~ 50 K in rotational temperature in the reaction region. In this imaging experiment allyl radicals are produced by 266 nm photolysis of allyl iodide at the tip of the nozzle, which gives ~ 5 K in rotational temperature after supersonic expansion (see Fig. 1.1). Since both previous experiments[19,20] indicated the methyl channels to be isotropic ($\beta = 0$), it would be interesting to see if some anisotropy can be detected by further cooling the allyl radicals before excitation.

1.2.2 *VENUS / NWChem*

As experimentalists the first step we took toward the non-RRKM aspect of the project was to incorporate a general chemical dynamics program called *VENUS* (developed by William Hase of the Texas Tech University[26]) to perform classical trajectory simulations with *NWChem* (an *ab-initio* computational chemistry software package from the Pacific Northwest National Laboratory[27]) which

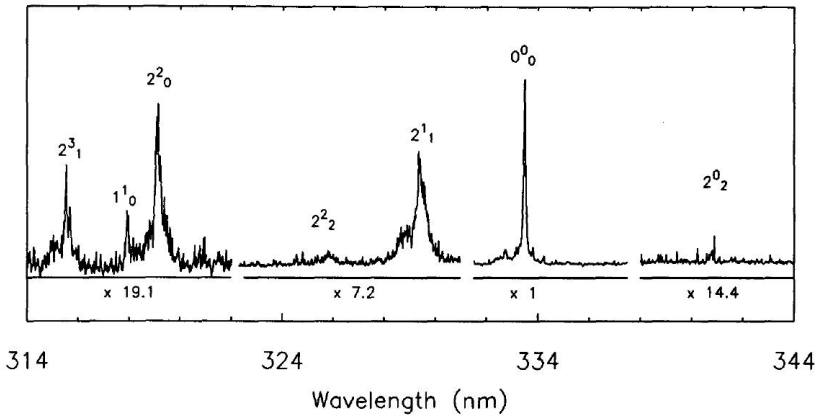

Figure 1.6: Previously published 2+1 REMPI spectra of methyl radical produced in the 226 nm photodissociation of CH_3I and probed on the $3p\,^2A_2'' \leftarrow 2p\,^2A_2''$ transition.[25]

provided the necessary quantum mechanical methods and basis sets. For each trajectory simulation, *VENUS* was first given a starting geometry/energy and a random number which indicated the "direction" on the 2-D potential surface to start. It then calculated the potential energy as the trajectory proceeded, *i.e.* it virtually turned a 2-D problem into a 1-D step-by-step calculation. The speed of calculation depended on the size of the steps and mostly on the level of quantum mechanical theories and basis sets. We chose B3LYP/cc-pVTZ as the adequate balance between accuracy and computational time and started the trajectories from the last transition states before dissociation (states B and E of Fig. 1.3). We saw no difference between the two methyl elimination mechanisms, *i.e.* the invalidity of RRKM has to come from either state A or states C and D. Fig. 1.7 shows the simulated $P(E_{trans})$ along with the experimental results from Fig. 1.4.

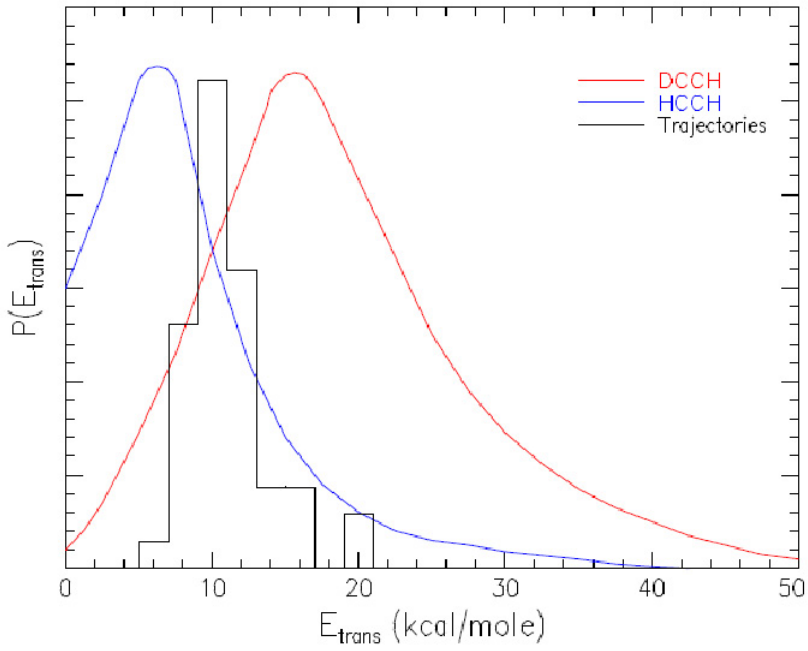

Figure 1.7: VENUS/NWChem B3LYP/cc-pVTZ simulation of P(E_{trans}) starting at states B and E of Fig. 1.3. The result is compared to the experimental P(E_{trans}) distributions from Fig. 1.4 and indicates that there is no difference between the two methyl elimination mechanisms from the last barriers.

The next step would be to start trajectories at transition states A, C or D. However, ~ 30 kcal/mole barrier heights such as those before transition states B and E were already too high for *VENUS* to efficiently jump over. Even at a low UHF/6-31G* level *VENUS* spent a long time oscillating in the wells between states A and B or D and E before it reached to products; and in most cases it just could not accomplish the leap. At this point collaboration with a theory group to perform efficient and accurate simulations was necessary, and calculations on a pre-calculated PES by the Bowman group of Emory University will be discussed at length in Chapter 2.

1.3 Velocity-Map-Imaging (VMI): General Concept

The method of charged particle imaging was first invented by Chandler and Houston in 1987.[28] Ten years later, Eppink and Parker discovered the ability of a simple electrostatic lens to map ions with the same velocity regardless of their points of formation in space.[29] A comprehensive description of this powerful VMI technique, along with its history of development and image analysis methods, can be found in the first four chapters of the book edited by Whitaker.[30] In dissociation of a chemical bond, •-◦ + $h\nu$ → • + ◦ (• and ◦ can be either an atom or a molecular fragment), two partner fragments are created in each photodissociation event. They fly in opposite directions with equal translational momentum in the center-of-mass frame. The fragments build up spherical distributions, so-called Newton spheres, in velocity space if we repeat the same event for many times. Fig. 1.8[30] outlines the experimental steps in VMI of a photodissociation reaction: (a) photodissociation of molecules in a molecular beam by using a linearly polarized laser with the polarization direction parallel to the detector surface, (b) conversion of the photofragment atoms or molecules making up the Newton spheres into ions by laser ionization, (c) projection of the ion spheres onto a two-dimensional detector, and (d) mathematical transformation of the 2-D image back to the 3-D data of step (a). Application of steps (a) and (b) specifically to our study on allyl radicals will be discussed in detail in Chapter 3; here we show the ability of VMI that gives better resolved images in step (c) and discuss the concepts of reconstruction methods in step (d).

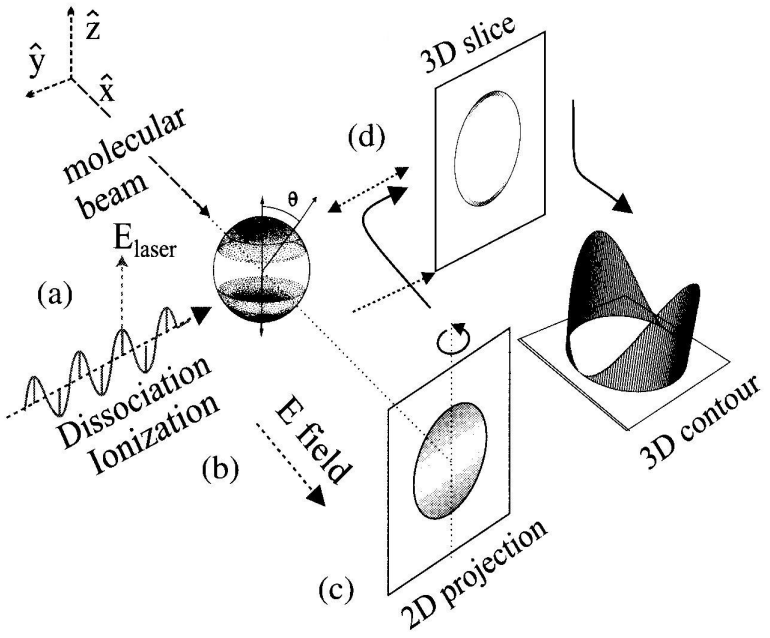

Figure 1.8: Schematic diagram of the photofragment imaging approach to measuring Newton spheres from photodissociation. See text for detailed description.[30]

1.3.1 The Power of VMI

The power of VMI can be demonstrated by the ion trajectory simulation in Fig. 1.9[29] : Panel-(i)a shows the total overview with repeller voltage = 1000V and extractor voltage = 750V. The laser propagates along the y direction, causing a line source of 3.0 mm length. In Panel-(i)c there are three different starting positions spaced 1 mm apart. From each starting point eight trajectories are displayed with the same kinetic energy but of 45° elevation angle difference, as illustrated in panel-(i)b. At the focusing plane, panel-(i)d, ion trajectories of the same ejection angle but different starting positions come together, where numbers 1, 2 and 3 correspond to ejection angles of 0/180° (x direction), 45/135° and 90° (y-direction), respectively. Panel(ii) shows an image of O^+ ions from

the photodissociation of O_2 $3d\pi(^3\Sigma_{1g}^-)$(v = 2, N = 2) Rydberg molecules around 225 nm by ion-imaging; and Panel(iii) shows the improvement by using VMI to collect data from the same process. The laser polarization, *i.e.* axis of cylindrical symmetry, is vertical in both images.

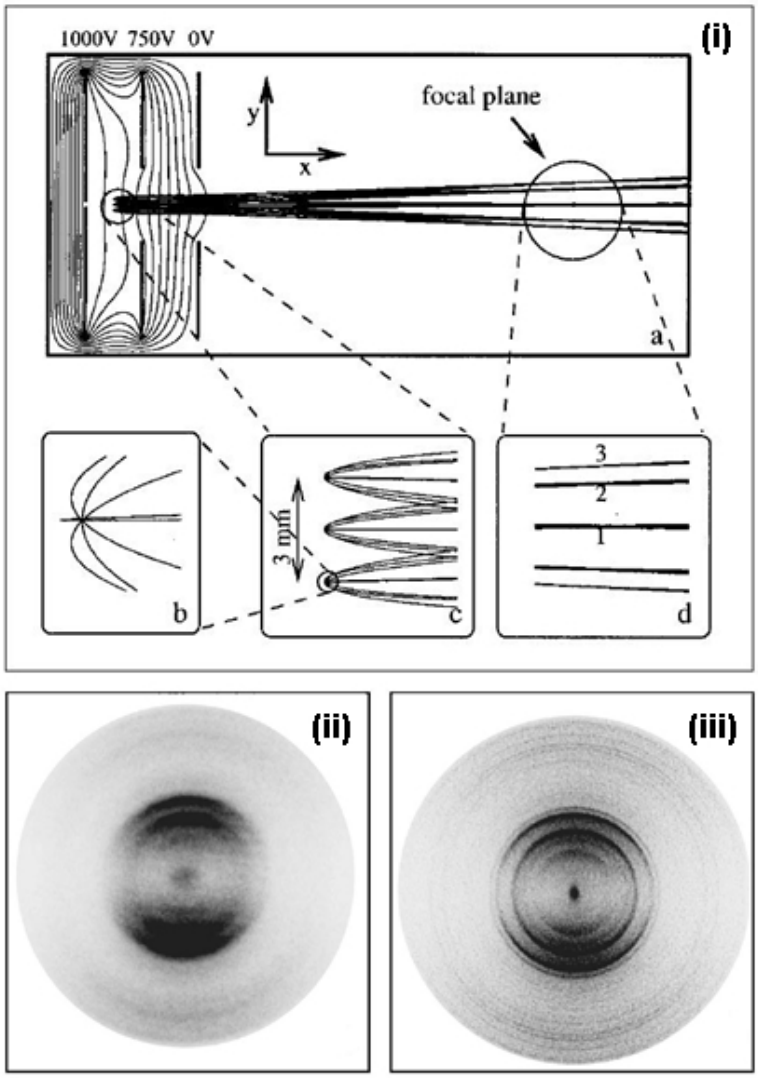

Figure 1.9: (**i**) Ion trajectory simulations for the velocity-mapping setup with 'Simion'. (**ii**) Ion-imaging of O^+ ions from the photodissociation of O_2 $3d\pi(^3\Sigma_{1g}^-)$(v = 2, N = 2) Rydberg molecules around 225 nm. (**iii**) VMI of the same process in (ii). See text for detailed description.[29]

1.3.2 Reconstruction Methods

The basic concepts of image reconstruction can be found in Chapter 3 of ref. 30, which we follow in this section using the v = 0 methyl radical image from the I*($^2P_{1/2}$) channel of 248 nm dissociation of methyl iodide as an example and discuss in detail the PBASEX algorithm. All the reconstruction methods for cylindrically symmetrized images are based upon a mathematical procedure called the inverse Abel transform. Here we only consider methods used in our data analysis procedures. We need first to define some physical quantities, mostly vectors and angles, by adopting the space-fixed coordinates (X, Y, Z) and labels used by Schmiedl et al.[31] and shown in Fig. 1.10. $\mathbf{k}_D$ is the propagating direction of the dissociation laser, and its electric polarization is $\mathbf{E}_D$. $\mathbf{v}$ is the recoil velocity of the fragment of interest and θ is defined by $\cos^{-1}[\mathbf{v} \cdot \mathbf{E}_D]$. We choose the space-fixed Z-axis to be along $\mathbf{E}_D$ and X-axis to be pointing opposite to $\mathbf{k}_D$. $\mathbf{k}_p$ is the propagating direction of the probing laser, and the new space-fixed coordinate is defined by rotating around the X-axis through an angle θ' so the new z′ axis is pointing opposite to $\mathbf{k}_p$.

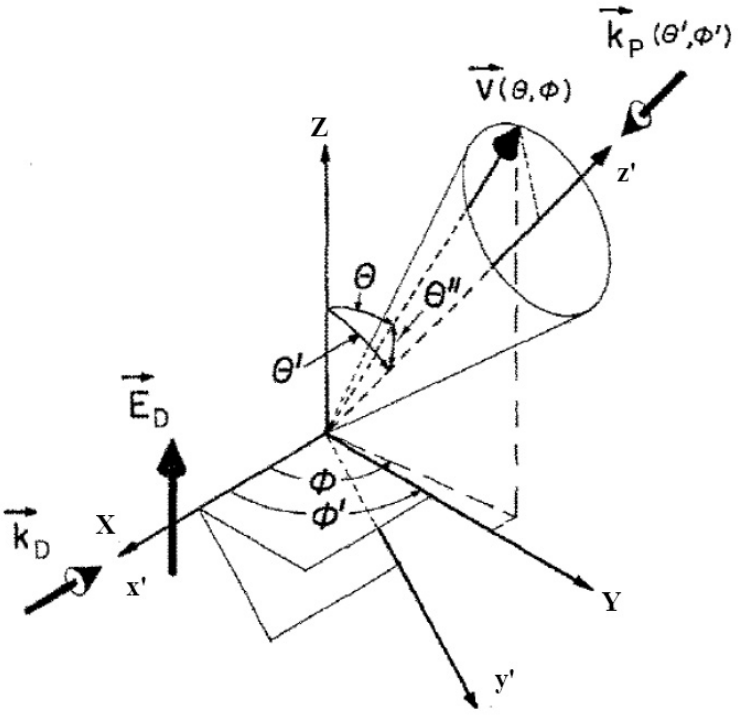

Figure 1.10: Definition of photodissociation spatial coordinates and orientations. See text for explanation.[31]

Fig. 1.11(a) shows the raw image of v = 0 methyl radicals in the I*($^2P_{1/2}$) channel of 248 nm dissociation of methyl iodide. The dissociation happened obviously via a parallel transition as indicated by the direction of $\mathbf{E}_D$. We designate the velocity distribution of the photofragment in the space-fixed coordinate by h(X, Y, Z), and the image shown in Fig. 1.11(a) is a collection of ion spheres collapsed in the -X direction:

$$F(\mathrm{Y},\mathrm{Z}) = \int_{-\infty}^{+\infty} h\,(\mathrm{X},\ \mathrm{Y},\ \mathrm{Z})\,d\mathrm{X}\ . \tag{1.1}$$

We first consider arbitrarily one row of the image with Z coordinate Z_{arb}, as indicated by the blue line:

$$f(\mathrm{Y}, \mathrm{Z} = \mathrm{Z_{arb}}) = \int_{-\infty}^{+\infty} h\,(\mathrm{X},\ \mathrm{Y},\ \mathrm{Z} = \mathrm{Z_{arb}})\, d\mathrm{X}$$
$$= 2\int_{0}^{+\infty} h\,(\mathrm{X},\ \mathrm{Y},\ \mathrm{Z} = \mathrm{Z_{arb}})\, d\mathrm{X}\ . \qquad (1.2)$$

This row is plotted in Fig. 1.11(c), and our task here is to recover $h(\mathrm{X}, \mathrm{Y}, \mathrm{Z} = \mathrm{Z_{arb}})$ from the measured $f(\mathrm{Y},\ \mathrm{Z} = \mathrm{Z_{arb}})$. A simple change of variables $r^2 = \mathrm{X}^2 + \mathrm{Y}^2$ re-writes Eq. 1.2 in polar coordinates as

$$f(\mathrm{Y}, \mathrm{Z} = \mathrm{Z_{arb}}) = 2\int_{\mathrm{Y}}^{\infty} \frac{h(r)r}{\sqrt{r^2 - \mathrm{Y}^2}}\, dr\ . \qquad (1.3)$$

By applying the Fourier transform convolution theorem to Eq. 1.3 $h(r,\ \mathrm{Z} = \mathrm{Z_{arb}})$ can be recovered from $f(\mathrm{Y},\ \mathrm{Z} = \mathrm{Z_{arb}})$:

$$h(r,\ \mathrm{Z} = \mathrm{Z_{arb}}) = \frac{1}{\pi}\int_{r}^{\infty} \frac{df/d\mathrm{Y}}{\sqrt{\mathrm{Y}^2 - \mathrm{r}^2}}\, d\mathrm{Y}\ . \qquad (1.4)$$

Eq. 1.3 is the Abel transform and Eq. 1.4 is the inverse Abel transform. Solving Eq. 1.4 is difficult in practice because of the singularity at $r^2 = \mathrm{Y}^2$ and the noise-sensitive $df\ /\ d\mathrm{Y}$ in the integrand. The 480 × 640 pixel image data in Fig. 1.11(a) was collected as a 480 × 640 matrix with each matrix element indicating intensity, as shown by the vertical bars in Fig. 1.11(c). In order for Eq. 1.4 to be applicable the `discrete` data points have to be fitted by some computationally maneuverable `continuous` functions. The program we employed in data analysis was developed by Garcia et al. named PBASEX (**P**olar **BA**sis **S**et **EX**pansion).[32] The original algorithm, named BASEX, was invented Dribinski et al. [33] who expanded the experimental projection data over a set of Cartesian basis functions that were analytical projections of known well-behaved functions. We can extend Eq. 1.3 to the whole 2-D distribution by replacing $f(\mathrm{Y},$

$Z = Z_{arb}$) by $F(Y, Z)$ and $h(r)$ by $H(r, Z)$, which leads to the digitized $N_Y \times N_Z$ projection function **P** for the experimental data image:

$$\mathbf{P}_{ij} = 2 \int K(Y - Y_i,\ Z - Z_j)\, dY dZ \int_{|Y|}^{\infty} \frac{r\, H(r,\ Z)}{\sqrt{r^2 - Y^2}}\, dr \ , \tag{1.5}$$

where K defines the instrumental function which makes little influence to the final results and has been suggested by Dribinski et al. to be approximated by the Dirac δ function. Assume we have a basis set $\{q_m(r, Z) = \rho_m(r)\zeta_n(Z)\}$ for ($m = 0, \ldots, N_Y - 1$, and $n = 0, \ldots, N_Z - 1$) and their corresponding projection basis functions $\{\mathbf{T}_m\}$, and $\mathbf{T}_{mij}$ is related to $q_m(r, Z)$ through Eq.1.5 as $\mathbf{P}_{ij}$ is related to $H(r, Z)$. If the basis set is appropriate for making a complete representation of **P**, and if the basis functions are well-behaved under the Abel transform, we may expand $H(r, Z)$ and $\mathbf{P}_{ij}$ as

$$\begin{aligned} H(r,\ Z) &= \sum_{m=0}^{N_Y-1} \sum_{n=0}^{N_Z-1} C_{mn}\, \rho_m(r)\, \zeta_n(Z) \ , \\ \mathbf{P}_{ij} &= \sum_{m=0}^{N_Y-1} \sum_{n=0}^{N_Z-1} C_{mn}\, \mathbf{R}_{mi}\, \mathbf{S}_{nj} \ ; \end{aligned} \tag{1.6}$$

with

$$\begin{aligned} \mathbf{R}_{mi} &= 2 \int K_Y(Y - Y_i)\, dY \int_{|Y|}^{\infty} \frac{r\, \rho_m(r)}{\sqrt{r^2 - Y^2}}\, dr \ , \\ \mathbf{S}_{nj} &= \int K_Z(Z - Z_j)\, \zeta_n(Z)\, dZ \ . \end{aligned} \tag{1.7}$$

The basis sets $\{\rho_m(r)\}$ and $\{\zeta_n(Z)\}$ are optimal if they are able to account for sharp features of the order of one pixel and to be smooth on a smaller scale. In BASEX, the following radial basis set has been chosen that satisfies these conditions:

$$\rho_m(r) \;=\; \left(\frac{e}{m}\right)^{m^2} \left(\frac{r}{\sigma}\right)^{2m^2} e^{-\left(\frac{r}{\sigma}\right)^2} \quad , \tag{1.8}$$

where σ is of the order of the distance between the pixels and m = (0, . . . , $N_Y/2 - 1/2$). The $\zeta_n(Z)$'s are chosen to be the same as the radial basis functions, thus $\zeta_n(Z) = \rho_n(Z)$, which leads to $\mathbf{S}_{nj} = \rho_n(Z_j)$ for n = (0, . . . , $N_Z/2 - 1/2$). The $\{\rho_m(r)\}$ have their maximum at $r = m\sigma$ and are practically indistinguishable from the Gaussian functions, *i.e.* $\rho_m(r) \approx \exp[-2(r/\sigma - m)^2]$ for sufficiently large m. With these specially chosen basis sets, BASEX converts the ill-posed inverse problem into a simple problem of finding expansion coefficients, C_{mn} in Eqs. 1.6 and 1.7, a procedure that requires only matrix multiplication.

In PBASEX, Garcia et al. employed computational procedures very similar to BASEX but realized that polar coordinates, (r, θ), would be a more intuitive choice to perform image inversion since it corresponds to the symmetry of photon-matter interaction. PBASEX converts the detected images to polar coordinates prior to inversion which makes itself less sensitive to the noise coming from the detector's Cartesian grid, therefore better energy and angular resolution can be achieved. The basis sets ρ in PBASEX are written as products of Gaussian functions (to model the energy distribution) and Legendre polynomials (to model the angular distribution with respect $\mathbf{E}_D$), *cf*. Eq. 1.8,:

$$\rho_{k,l}(r,\theta) \;=\; e^{-(r\,-\,r_k)^2/\sigma} P_l(\cos\theta) \quad , \tag{1.9}$$

where P_l is the Legendre polynomial of order l and r_k represents the center of the kth Gaussian with k preset to k_{max} = 128. The basis functions in PBASEX, *cf*. the $\mathbf{R}_{mi}\mathbf{S}_{nj}$ term in Eq. 1.6, are the limiting steps of the inversion procedure, but they are only computed once and stored in the hard disk for future use since

they are data independent. Also, for one-photon dissociation by a linearly polarized light, as in our study of allyl, only two angular terms $l = 0, 2$ are needed. The detailed computational parameters used in our data analysis will be specified in Section 3.1.5; here we show the PBASEX inverted images of Fig. 1.11(a) in Fig. 1.11(b) as an example with a representative slice in Fig. 1.11(d).

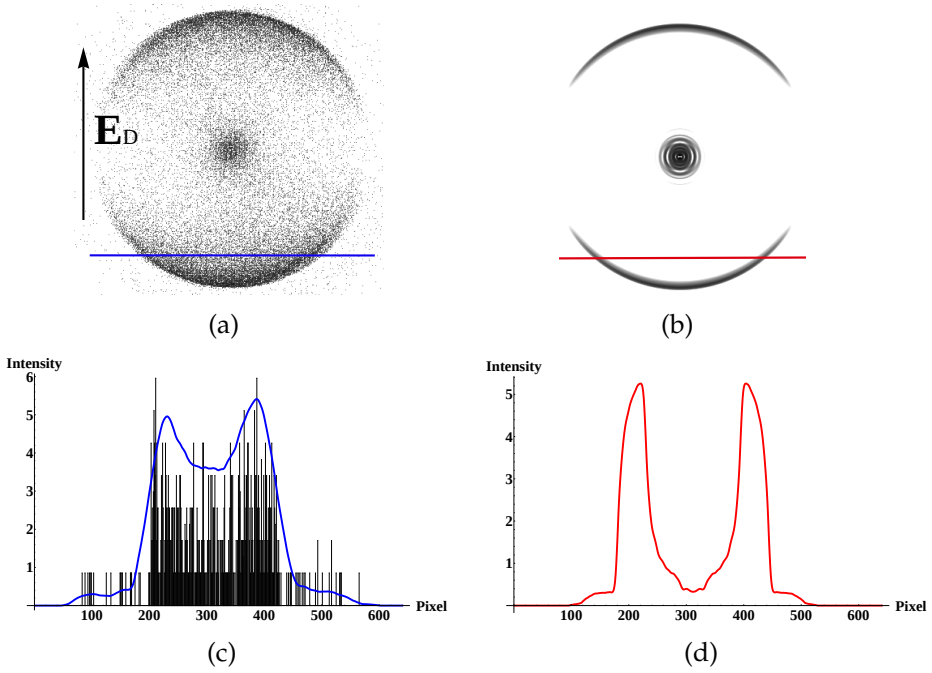

Figure 1.11: **(a)** Raw 480 × 640 pixels image of methyl radicals with v = 0 from the I($^2P_{3/2}$) channel of 248 nm photodissociation of methyl iodide, **(b)** reconstructed image of (a) transformed by PBASEX, **(c)** a representative slice of row pixel #113 of the raw image (a), and **(d)** a representative slice of row pixel #113 of the reconstructed image (b).

1.3.3 Interpretation of the Photodissociative VMI Data

In a photodissociation event, mass-selective ionization happens immediately when the fragment of interest is created, and the time-of-flight (TOF) is between ionization and detection. The `position` of a ring, *i.e.* its distance from the center of the image, divided by the TOF gives us the speed of the fragment after dissociation, usually in a few thousand meter per second. This can be easily calculated if the detection system is properly calibrated (see Sec. 3.1.4). The `shape`, *e.g.* if the ring appears to be a whole circle or just a fraction of it, and the `alignment`, *e.g.* if the ring appears on the "equator" or at the "north/south poles" or at one of the four quadrants, are far more complicated to interpret. Fig. 1.10 shows as much as we need to say about things fixed in space; what is not shown in Fig. 1.10 are things dependent on the parent molecule, among them the most important of all: the transition dipole moment $\boldsymbol{\mu}$. Let us start with the simplest photochemical reaction: dissociation of a diatomic molecule A—B with a polarized light. The absorption probability is greatest when the transition dipole moment $\boldsymbol{\mu}$ is aligned with the electric vector $\mathbf{E}_D$ of the light. Zare and Herschbach [34] first pointed out that the vector correlation between $\boldsymbol{\mu}$ and velocity of the product $\mathbf{v}$ can lead to an anisotropic distribution of the photofragments. For diatomics, there were only four cases to consider because $\boldsymbol{\mu}$ is either *parallel* or *perpendicular* to the molecular axis, and $\mathbf{v}$ can be either along the initial direction of the molecular axis (the *axial recoil*) or perpendicular to it (the *transverse recoil*). Using the direction cosine matrix $\Lambda_{S\,M}(\theta, \phi, \chi)$ to correlate molecular-fixed axis $_{(M)}$ to space-fixed axis $_{(S)}$ via Euler angles (θ, ϕ, χ), the absorption probability is proportional to $| \boldsymbol{\mu} \cdot \mathbf{E}_D |^2 = \mu^2 \, {E_D}^2 \, | \Lambda_{S\,M}(\theta, \phi, \chi) |^2$. By choosing the molecular-fixed z-axis to be the departing direction of the atom of interest, say atom A, the differential cross section per unit solid angle is $I_{S\,M}(\theta, \phi)$

$= 1/2\,\pi \int_0^{2\pi} |\,\Lambda_{SM}(\theta, \phi, \chi)\,|^2\, d\chi$. The dependence on ϕ is further eliminated if the space-fixed Z-axis is chosen to be along $\mathbf{E}_D$. Zare and Herschbach discovered that in all four cases $I(\theta)$ appeared in simple mathematical forms, and Zare [35] later reported the most important equation in photodissociation dynamics:

$$I(\theta) \;=\; \frac{1}{4\pi}\,[\,1 + \beta\, P_2(\cos\theta)\,] \qquad (-1 \le \beta \le 2)\;\;, \tag{1.10}$$

where $P_2(\cos\theta) = 1/2\,(\,3\cos^2\theta - 1\,)$ is the second Legendre polynomial, and $1/4\,\pi$ normalizes the function for the full solid angle. The anisotropy parameter β which defines the angular distribution can be further expressed as an average over the distribution of angle γ between $\boldsymbol{\mu}$ and $\mathbf{v}$:[36]

$$\beta \;=\; 2\,\langle\, P_2(\cos\gamma)\,\rangle\;\;. \tag{1.11}$$

As γ decreases from $\pi\,/\,2$ to zero, β increases from -1 to 2; in other words, β = -1 describes the perpendicular ($\boldsymbol{\mu} \perp \mathbf{v}$) transition, $\beta = 2$ describes the parallel ($\boldsymbol{\mu} \parallel \mathbf{v}$) transition, and for $\beta = 0$ the angular distribution is isotropic in space. In order to observe the complete effect of Eq. 1.10 the dissociation needs to happen much faster than the rotational period of the parent molecule, otherwise the observed θ is contaminated by the parental rotation.

The orientation of the probing laser becomes important if the fragment of interest can come from multiple channels due to different internal states of the other fragment. Schmiedl et al. [31] studied 266 nm photodissociation dynamics of H—I that occurred in two channels, one gave H + I*($^2P_{1/2}$) via a parallel transition and the other produced H + I($^2P_{3/2}$) via a perpendicular transition. They monitored the Doppler profile of the ground state H atom from both channels

by VUV laser induced fluorescence (LIF), and the results were heavily dependent on the angle θ' of the probing laser. For a fragment, H atom in this case, with a speed distribution $f(|\mathbf{v}|) = \delta(|\mathbf{v}| - v_0)$, the LIF excitation frequency is given by $\nu = \nu_0 (1 \pm w/c)$; where c is the speed of light and the Doppler shift of ν away from ν_0 is characterized by $w = v_0 \cos\Delta$. The velocity distribution is of course $F(\mathbf{v}) = f(|\mathbf{v}|)\ I(\theta)$, and the Doppler profile $I(\Delta)$ can be described by $\int F(\mathbf{v})\ d^3v$, which leads to

$$I(\Delta) \ = \ \frac{1}{4\pi} [\ \beta\ P_2(\cos\theta')\ P_2(\cos\Delta)\ ] \quad . \tag{1.12}$$

Things get more complicated if the fragment of interest possesses either molecular or electronic angular momentum **J**. Eq. 1.10 and Eq. 1.12 describe the so-called **E**-$\boldsymbol{\mu}$-**v** correlation, and more phenomena are possible with the introduction of **J**, *e.g.* **E**-$\boldsymbol{\mu}$-**J**, **v**-**J**, and **E**-$\boldsymbol{\mu}$-(**v**-**J**) correlations. Angular momentum theories, from simple rotational matrix $D^J_{MM'}(\theta, \phi, \chi)$ to the more complicated bipolar harmonics B_{KQ}(k, k'), were used to study photodissociation dynamics involving **J** and will be further discussed in later chapters when needed. When VMI was not available people studied these correlations by monitoring the Doppler profiles;[37–41] now these dynamics involving angular momentum can be directly exposed in the velocity-mapped images. A single VMI measurement can reveal the polarization effects from multiple Doppler experiments. An demonstrative example would be the VMI study of O(^{1}D) from photodissociation of molecular oxygen with total excitation energy of 7.71 eV.[42] Fig. 1.12 shows the image collected with the probing laser polarized in the same direction as the excitation lasers. Because of the strong angular momentum alignment of the atomic electronic angular momentum **J** perpendicular to **v**, the vertically moving atoms could not be efficiently ionized, and therefore holes were observed at the poles.

Without the knowledge of **v-J** correlation Eq. 1.10 could have predicted this image to have a simple $\cos^2\theta$ angular distribution.

The Doppler shift still plays an important role in VMI: consider a dissociation event that produces the fragment of interest flying forward and backward in the propagating direction of the probing laser. In order to detect all the fragments with equal frequency it is thus necessary to scan the probing laser over a wavelength range that covers the forward and backward Doppler shifts.

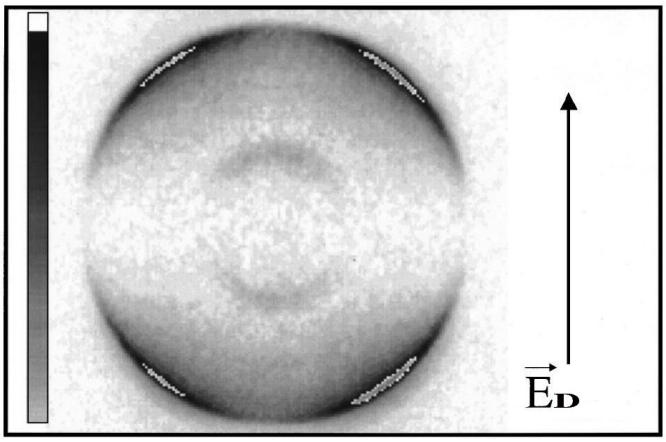

Figure 1.12: Velocity map image of $O(^1D)$ from photodissociation of molecular oxygen at excitation energy of 7.71 eV. Signal levels are indicated by the gray bar. The dissociation and probing laser polarization lie in the vertical axis. The unusual angular distribution observed was due to the **v-J** correlation.[42]

CHAPTER 2

SEMI-CLASSICAL TRAJECTORY SIMULATION

2.1 Publications and Credits

"*Evidence for Vinylidene Production in the Photodissociation of the Allyl Radical*"

The Journal of Physical Chemistry Letters, volume 1, pages 1875–1880

"*The Dynamics of Allyl Radical Dissociation*"

The Journal of Physical Chemistry A, volume 115, pages 6797–6804

Chao Chen, **Bastiaan Braams** and **Joel M. Bowman**,

Department of Chemistry, Emory University

David Y. Lee and **Paul L. Houston**

Department of Chemistry

Cornell University / Georgia Institute of Technology

Domenico Stranges

Dipartimento di Chimica, Universit La Sapienza, Rome, Italy

2.2 Computational Methods

2.2.1 Construction of the Potential Energy Surface

The construction of the PES employed procedures developed previously in the Bowman research group.[43–45] Briefly, the research of PES construction was started by using a conceptually straightforward function in terms of internuclear distances instead of the required degrees of freedom in various coordinates to describe the true PES,

$$V(x_1, ..., x_d) = \sum_{i_1 ... i_d} C_{i_1 ... i_d} S \left\{ x_1^{i_1} \cdots x_d^{i_d} \right\} , \quad (2.1)$$

where the x_i are functions of internuclear distances and the symbol S indicates a symmetrization operator so that the symmetrized monomial $S\{\cdots\}$ is invariant with respect to interchange of any two identical nuclei. However, for instance, C_3H_5 has 720 (3!5!) terms in $S\{\cdots\}$ which make V quite large and expensive to evaluate. In the next stage of research the basis $S\{\cdots\}$ was replaced by the polynomials of Morse-type variables y_{ij} given by $y_{ij} = exp(-r_{ij} / \lambda)$, where r_{ij} is the internuclear distance between nuclei i and j.

In constructing the allyl ground electronic PES, the associated 3308 coefficients were obtained by standard linear-least squares fitting to a data set of 97418 *ab initio* energies, computed at the coupled cluster single, double, and perturbative treatment of triple excitations (CCSD(T)) with the augmented correlations-consistent polarized triple basis set (aug-cc-pVTZ) as implemented in MOLPRO.[46] The configurations included regions of the complex C_3H_5, the separated $CH_3 + C_2H_2$ and the product channels for each of the C_3H_4

isomers and hydrogen. Additional energies of about 20,000 fragment configurations were obtained by separating the fragments by about 8 Bohr, and assigning the energy as the sum of their fragment energies. The RMS fitting error was 2.4 kcal/mole for energies up to 63 kcal/mole.

Stationary points describing the CH_3 + HCCH formation on the PES have already been calculated and reported along with the experimental results obtained in Rome.[20] Castiglioni et al. [10] have constructed a more comprehensive description of stationary points covering the C_3H_4 + H region. Those points were used to check our fitted PES. Fig. 2.1 shows the schematic representation of the total C_3H_5 PES. It contains a global minimum (GM), 3 local minimum (LM), 9 saddle points (TS) and 4 fragment channels (CH_3 + HCCH and H + three C_3H_4 isomers). The hydrogen loss channels are not barrierless but have saddle points connecting local minima and fragment configurations. As previously mentioned, there exist two mechanisms in the methyl elimination channel, one passes through LM1 and the other does not (both shown in black dotted lines). In addition to these two mechanisms, our PES also showed an unusual mechanism starting from LM1 in which the CH_3CCH_2 dissociates directly into CH_3 and CCH_2, highly excited vinylidene, then easily isomerized to internally hot acetylene via a small barrier (shown in red dotted lines). This isomerization from CCH_2 to HCCH has been carefully checked to behave well via a known saddle point.[47] Overall, the stationary points on our fitted PES agree quite well with other *ab-initio* results in terms of geometry, potential energy and harmonic frequencies. Table 2.1 gives the potential energy comparison between our PES and other *ab-initio* results.[10,20,47]

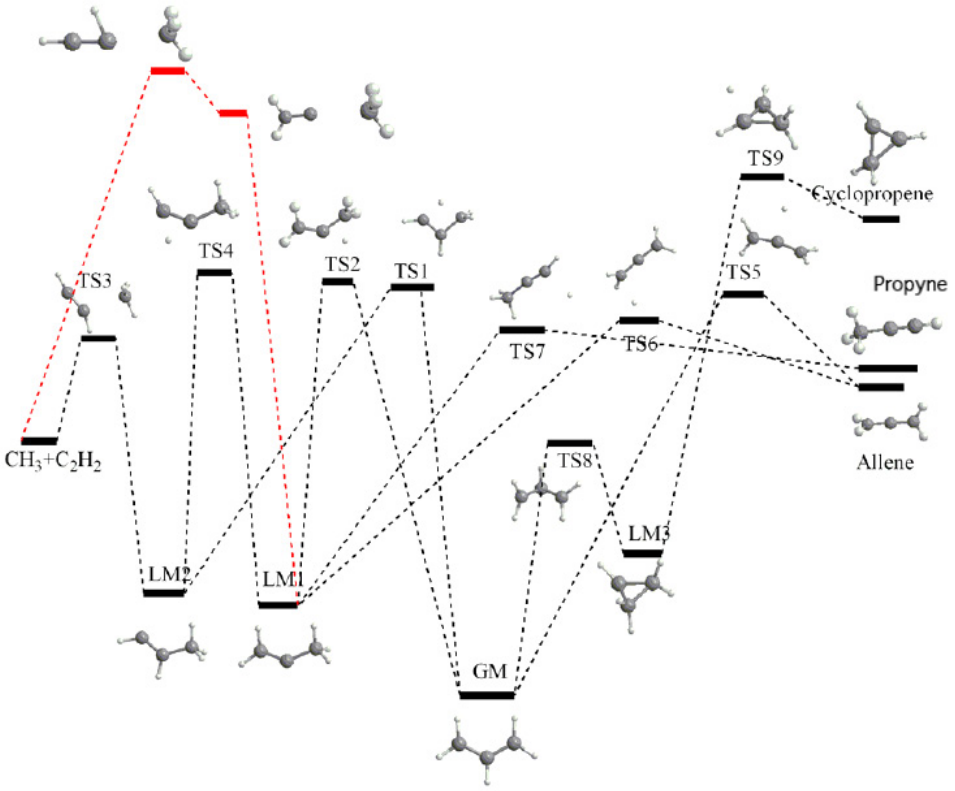

Figure 2.1: Schematic representation of the allyl *ab-initio* potential energy surface including the vinylidene channel.

2.2.2 Trajectory Calculations

The semi-classical trajectory calculations were performed using methods similar to those published before.[48] Calculations were done in a space-fixed frame using microcanonical sampling of initial momenta subject to the zero total angular momentum constraint. Roughly 19,000 trajectories were initiated at the global minimum, with a total energy corresponding to 248 nm excitation plus harmonic zero point energy. The integration was done using time steps of 0.1205 fs and were run for typically 200,000 steps or 24.1 ps (in some cases 100,000 steps or about 12 ps).

Table 2.1: (a) Comparison of our fitted potential energy surfaces and *ab-initio* benchmark electronic energy calculations for selected stationary points on the C_3H_5 surface relative to allyl global minimum (kcal/mole). (b) Part of the C_3H_5 surface describing vinylidene and acetylene isomerization relative to vinylidene local minimum (kcal/mole).

(a)

	QCISD(T)[20]	**CCSD(T)**[10]	**Our PES**
GM	0		0
LM1	19.9		20.4
LM2	23.3		25.0
LM3		32.1	29.5
TS1	67.4		69.6
TS2	67.5	67.2	70.5
TS3	60.8		62.5
TS4	72.0		70.9
TS5		66.9	69.4
TS6		65.1	66.4
TS7		64.3	63.5
TS8		53.2	51.9
TS9		86.1	86.7
CH_3 + HCCH	52.6		52.4
Allen + H		62.4	62.9
Propyne + H		61.1	58.4
Cyclopropene + H		84.5	83.5

(b)

	CCSD(TQ)/cc-pvtz[47]	**CCSD(T)/ANO**[47]	**Our PES**
CH_3 + H_2CC	0	0	0
TS	2.67	2.87	2.26
CH_3 + HCCH	-45.61	-44.10	-45.1

2.2.3 Analysis Methods

Trajectories were analyzed by first assigning a structure to the products. A program automatically classified the final configuration into several categories, such as H + allene, H + propyne, H + other C_3H_4 products, and CH_3 + C_2H_2. Since the trajectories kept track of the identities of the different carbons and hydrogens, it was possible to further categorize the results. Thus, for the CH_3 + C_2H_2 category, the products were examined to see whether they were consistent with a 1,3 hydrogen shift mechanism or a double 1,2 hydrogen shift mechanism. There were multiple variants for each reaction depending on which hydrogens were transferred. Once the final structure has been determined, it was a simple matter to determine the relative velocity of the two fragments in the center-of-mass frame. This velocity was used to determine the kinetic energy distribution.

The total orbital angular momentum was determined from the final value of $\mathbf{r} \times \mathbf{p}$ in the allyl center of mass frame. In addition, the angular momentum of each fragment in its own frame could be similarly determined, and all angular momentum can then be converted into units of $\hbar$. Since the starting angular momentum was zero, the vector sum of the orbital momentum and the two fragment angular momenta must also be zero.

It was also possible to determine from the trajectory the projection of the angular momentum of each non-atomic fragment onto the direction of recoil, since this direction was known from the directions of the linear momenta of the fragments. This projection is sometimes called the **v**-**J** correlation; it ranges from $\mathbf{v} \parallel \mathbf{J}$ for helicopter-like motion to $\mathbf{v} \perp \mathbf{J}$ for frisbee-like motion. The **v**-**J** correlation does not depend on the rates of dissociation and parent molecule rotation[39] because it is not made until the instant of dissociation. Again, before the availabil-

ity of the imaging technique, this correlation was studied based on the Doppler profile of individual fragment rotational transitions, as discussed in the review article of ref. 39. Conventionally, it is simple to use the notation developed by Dixon,[40] who expanded the correlated angular momentum and velocity distribution in terms of the renormalized bipolar harmonics, β_Q^K(k k′). Bipolar harmonics often appear in problems involving two directions.[49] The general definition of bipolar harmonics, $B_{KQ}(k, k')$, can be found in ref. 49, which is simply a contraction of two modified spherical harmonics, $C_{kq}(\theta, \phi)$, in a Clebsch-Gordan type coupling equation:

$$B_{KQ}(k,k') \;=\; \sum_{q} \langle kq, k'q' | KQ \rangle \; C_{kq}(\theta,\phi)\, C_{k'q'}(\theta',\phi') \;\; . \tag{2.2}$$

Fig. 2.2 illustrates Dixon's notation of using renormalized bipolar harmonics to represent the spatial relationships between three important vectors: (1) $\boldsymbol{\mu}$ the parent molecule transition moment, (2) **v** the fragment recoil velocity, and (3) **J** the fragment angular momentum. For correlation between **v** and **J**, five renormalized bipolar harmonics can be used in describing the specific **v-J** orientations in the molecular fixed axis system of the parent molecule. Since we are only interested in the relationship between **v** and **J** after dissociation, the **v-J** correlation can be described by $\beta_0^0(22)$, which distinguishes **v** ∥ **J** from **v** ⊥ **J** in Fig. 2.2 regardless of the parent molecule orientation. Mathematically,

$$\beta_0^0(22) \;= P_2(\mathbf{v}\cdot\mathbf{J}) \quad , \tag{2.3}$$

where P_2 is the second Legendre polynomial, and $\beta_0^0(22)$ = - 1/2 for **v** ⊥ **J** and $\beta_0^0(22)$ = +1 for **v** ∥ **J**. Note that if one of the fragments, such as H, carries no angular momentum, then **J** for the second fragment must be antiparallel to the

orbital angular momentum, **L**. Since **L** by definition is perpendicular to the recoil velocity, **J** must be as well.

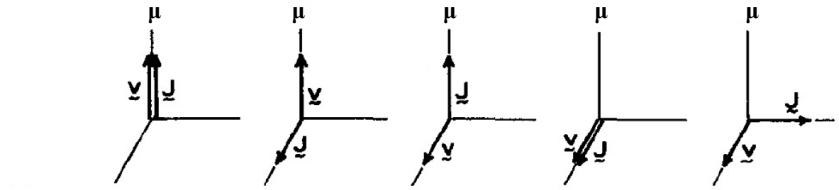

	(a)	(b)	(c)	(d)	(e)
$\beta_0^2(20)$	+1	+1	$-\frac{1}{2}$	$-\frac{1}{2}$	$-\frac{1}{2}$
$\beta_0^2(02)$	+1	$-\frac{1}{2}$	+1	$-\frac{1}{2}$	$-\frac{1}{2}$
$\beta_0^2(22)$	+1	$-\frac{1}{2}$	$-\frac{1}{2}$	+1	$-\frac{1}{2}$
$\beta_0^2(22)$	−1	$+\frac{1}{2}$	$+\frac{1}{2}$	$+\frac{1}{2}$	−1
$\beta_0^2(42)$	+1	$-\frac{1}{2}$	$+\frac{3}{8}$	$-\frac{1}{2}$	$+\frac{1}{8}$
$\beta_0^2(24)$	+1	$+\frac{3}{8}$	$-\frac{1}{2}$	$-\frac{1}{2}$	$+\frac{1}{8}$

Figure 2.2: The values of the lower-order renormalized bipolar harmonics for some limiting orientations of **v** and **J** of a photofragment in the molecular fixed axes of the parent molecule. μ is the parent molecule transition moment.[40]

The anisotropy parameter, β, in Eq. 1.10 and Eq. 1.11 can also be determined from the trajectories. This parameter β is equivalent to $2\beta_0^2(20)$. By ignoring the **J** vectors we see from the first row of Fig. 2.2 that $\beta_0^2(20) = +1$ when $\boldsymbol{\mu} \parallel \mathbf{v}$ and $\beta_0^2(20) = -1/2$ when $\boldsymbol{\mu} \perp \mathbf{v}$. As noted in Chapter 1, the allyl $B_1 \leftarrow A_2$ excitation at 248 nm has been assigned by Minsek et al. [15] as being due to a parallel transition with the transition moment along the *y(a)* axis. Each trajectory was performed in a space-fixed frame, where the the *y(a)* axis was initially located parallel to the space-fixed Z axis, and the product recoil velocity vector was identified to make a specific angle, γ, with respect to the *y(a)* axis, as described by Eq. 1.11. Collection of all the trajectories performed gave a distribution of β, from which an average may be determined.

2.3 Results and Discussion

2.3.1 General Overview

A general overview of the results was taken from a summary of 18,627 trajectories for C_3H_5 and 53,398 trajectories for CH_2CDCH_2 starting from the global minimum. The trajectories were stopped when a dissociation occurred or when they had run for 24 ps. Of these trajectories, ~18% / 28% did not react for C_3H_5 / CH_2CDCH_2, respectively, whereas 72% / 59% dissociated to give identifiable products. The dissociation product distribution is shown in the histogram of Fig 2.3. The other 10% / 13% visited problematic regions of the potential surface or gave products not easily identified by our computer algorithm. The PES does contain unphysical regions, usually associated with short internuclear distances. In these very high energy regions, *ab-initio* data may be very sparse or nonexistent, and the nature of the fit may yield unphysical deep negative values. These regions are usually very isolated; however, a small fraction of trajectories do find them. Such trajectories were discarded. Of the trajectories that did dissociate to identifiable products, 80% / 75% gave allen, 12% / 15% gave propyne, 5% / 8% gave methyl + acetylene via an apparent 1,3 hydrogen shift mechanishm, 1% / 1% gave methy + acethylene via an apparent double-1,2 hydrogen shift mechanishm, and the other 1% / 2% produced a C_3-containing producet that was not readily identified as allene or propyne. In some cases for this last group, the structure was that of cyclopropene, whereas in others, it was simply a tretched version of allene or propyne.

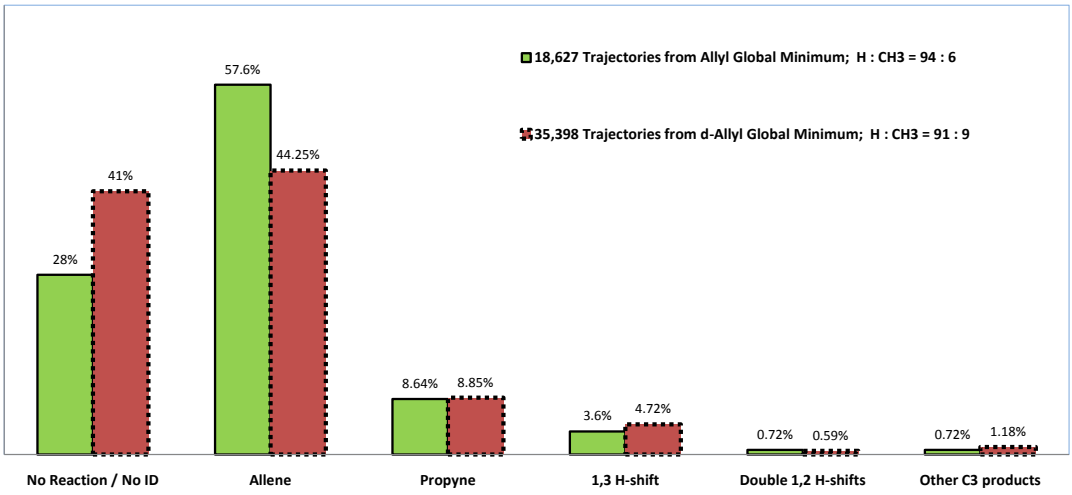

Figure 2.3: Histogram of the products from all the trajectories performed. 18,627 trajectories were started from the C_3H_5 global minimum and 35,398 trajectories were started from the CH_2CDCD_2 global minimum.

The trajectory results are generally in very good agreement with experimental data, although there may be some significant differences. The quantum yields (and branching ratios) for hydrogen and methyl elimination have been measured in Rome as 95% and 5% (BR = 19.0) for C_3H_5, which were in excellent agreement with the trajectory results of 94% and 6% (BR = 15.7) for C_3H_5 and 91% and 9% (BR = 10.1) for CH_2CDCH_2. Specifically for the mehtyl elimination channel, the experiment in Rome found the ratio of (1,3 hydrogen shift) : (double-1,2 hydrogen shifts and vinylidene) to be $\approx$ 1 : 1 / 1.6 : 1, whereas the trajectory results give 5.1 : 1 / 6.1 : 1 for C_3H_5 / CH_2CDCH_2. If acetylene produced via the vinylidene mechanism were more easily ionized than those being produced directly because of greater internal excitation, the experiment in Rome would underestimate this ratio. A summary of these results including those for the hydrogen atom loss channels is provided in Table 2.2.

Table 2.2: Comparison of trajectory results with previous experimental data.

Property	**C_3H_5 Trajectories**	**CH_2CDCH_2 Trajectories**	**Experimental**
allene QY	0.80	0.75	0.50 - 0.75[13]
propyne QY	0.12	0.15	0.50 - 0.25[13]
CH_3 (1,3)	0.05	0.08	0.05[20]
CH_3 (double 1,2 + H_2CC)	0.01	0.01	0.05[20]
dissociation time (ps)	16	23	1000 - 1000,000[22,50]
H : CH_3 elimination	94 : 6	91 : 9	95 : 5[20]
D : H elimination		2.9 : 1	2 : 1 - 3 : 1[13]
1,3 : double 1,2 + H_2CC	5.6 : 1	6.1 : 1	1 : 1[20]

2.3.2 Vinylidene Formation in the Methyl Elimination Channel

The methyl elimination channels starting from C_3H_5 and CH_2CDCH_2 were very similar; the kinetic energy distributions were nearly identical except for a slight shift to smaller energies for the deuterated compound, as expected from the slightly larger mass. Methyl elimination mechanisms were identified by examining the final products to see whether they were consistent with a 1,3 hydrogen shift mechanism or a double 1,2 hydrogen shift mechanism. The kinetic energy distributions for these two groups were determined separately and compared to the experimental data collected in Rome. The top panel in Fig. 2.4 shows that, indeed, the distribution for the dissociation of allyl via the 1,3 hydrogen shift peaked at a higher kinetic energy (~14 kcal/mole) than did the distribution for dissociation via the double 1,2 hydrogen shift. The distributions from

the trajectory results were in reasonable agreement with the experimental data. As noted in Section 1.2, this was particularly surprising on the RRKM grounds since the presumed two different hydrogen shift mechanisms both traverse LM2 of Fig. 2.1 before dissociation.

In trying to account for the difference in distribution between the two mechanisms, we ran trajectories starting from LM1 and LM2 of Fig. 2.1. For all of the trajectories that produced methyl, we determined the kinetic energy distribution in each case. These were plotted in the middle panel of Fig. 2.4. As can be seen from a comparison of the top and middle panels, the distributions obtained starting in these local minima were similar to those found for trajectories starting at the global minimum. Thus, for diagnostic purposes, it was sufficient to run trajectories from LM1 and LM2 of Fig. 2.1.

Trajectories that started from LM1 and proceed via a second 1,2 shift (and isomerize to LM2) produced, as expected, a nearly identical kinetic energy distribution to that for trajectories producing products but starting from LM2. Both distributions had average energies of about 18 kcal/mole. It thus appears that the RRKM assumption was correct; trajectories passing through the LM2 potential energy well did produce nearly identical kinetic energy distributions, regardless of how they got to this potential energy well.

The surprising result, which explained the paradox of why the two kinetic energy distributions were not identical, came from close examination of the trajectories starting from LM1. Those producing methyl were of two kinds, the ones that underwent the second 1,2 hydrogen shift and those that dissociated directly to vinylidene, representing a third pathway:

$$CH_3CCH_2 \longrightarrow CH_3 + \mathbf{H_2CC} \quad . \tag{2.4}$$

In more than half of the trajectories starting from LM1, CH_3CCH_2, the C—C bond broke well before a hydrogen from the CH_2 group migrated to the center carbon. Although the trajectories typically stopped soon after the C—C bond was broken, the H_2CC clearly had sufficient energy to rearrange to HCCH. On the other hand, the acetylene produced from vinylidene was created with a very large degree of vibrational energy, leaving much less energy available as kinetic energy of recoil. The kinetic energy distribution for acetylene produced from the combination of double 1,2 hydrogen shift and vinylidene was therefore peaked at lower energy than that for acetylene produced from a configuration consistent with the 1,3 hydrogen shift. Most of those that produce vinylidene did isomerize to highly excited acetylene. The kinetic energy distribution for those C_3H_5 trajectories starting at LM1 that produced vinylidene peaked near zero and had an average kinetic energy of only 6.4 kcal/mole. Those that produced acetylene via the second 1,2 shift had a translational energy distribution nearly identical to that for trajectories producing products but starting from LM2, as shown in the bottom panel of Fig. 2.4.

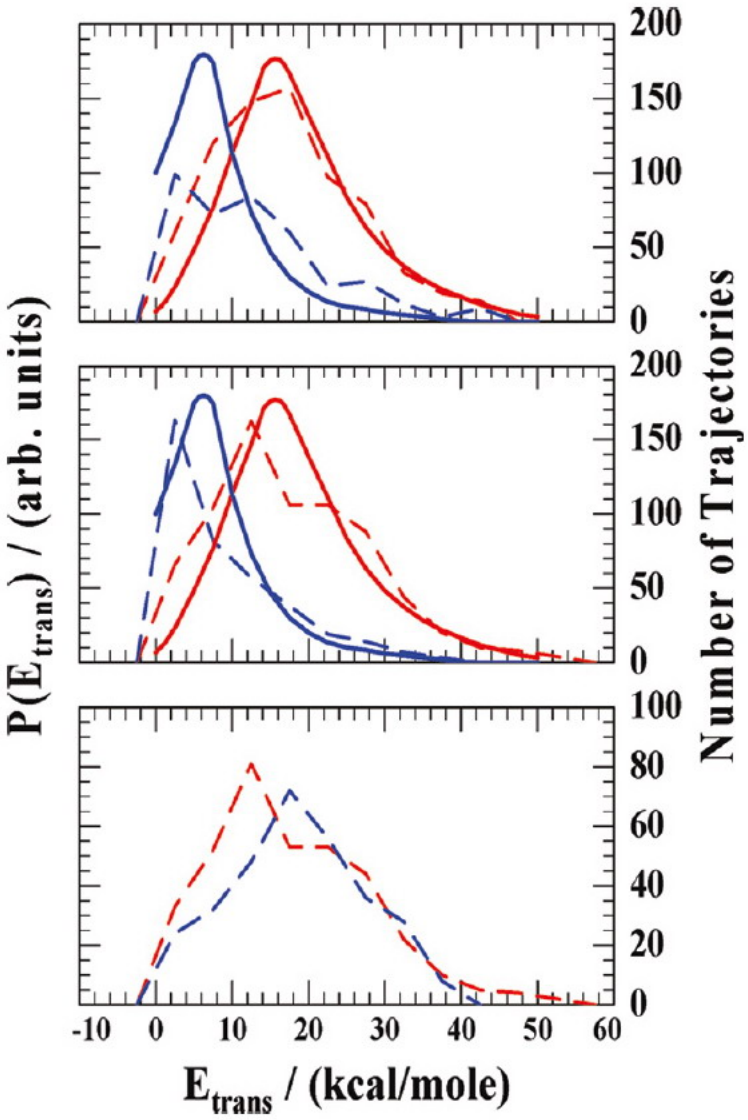

Figure 2.4: **Top Panel**: The solid curves give the experimental kinetic energy distributions for HCCH (blue) and DCCH (red) from ref. 20. The dashed curves give the corresponding distributions for trajectories starting at the allyl global minimum for C_3H_5 and producing HCCH (blue, ×3) and DCCH (red). **Middle Panel**: The heavy smooth curves are as in the top panel. The dashed curves are for methyl-producing trajectories starting in LM1 of Fig 2.1 (blue) and LM2 of Fig 2.1 (red). **Bottom Panel**: Comparison of the translational energy distributions for methyl-producing trajectories starting from LM2 of Fig 2.1 (red) or LM1 of Fig 2.1 (blue, ×4), where the latter trajectories included only those that undergo a second 1,2 shift; *i.e.*, vinylidene-producing trajectories were eliminated from the distribution.

Fig. 2.5 shows frames of a sample trajectory started from LM1 CH_3CCH_2 and dissociated to acetylene HCCH via the intermediate state of vinylidene H_2CC and CH_3. Frame 1 shows the formation of vinylidene, which occurred in ~1.2 fs from starting the trajectory. Frame 2 and Frame 3 show the migration, or roaming, process of the hydrogen atom to form acetylene from vinylidene while the two molecular fragments flying away from each other. As noted above, trajectories were also run for CH_2CDCH_2, equivalent to the experiment in Rome. As expected based on the results for CH_2CHCH_2, both double 1,2 shift and vinylidene mechanisms produced CDH_2 and HCCH. Thus, detection of the kinetic energy distributions by mass spectrometry would associate the detection of C_2H_2 to both mechanisms while associating the detection of DCCH to the 1,3 hydrogen shift mechanism.

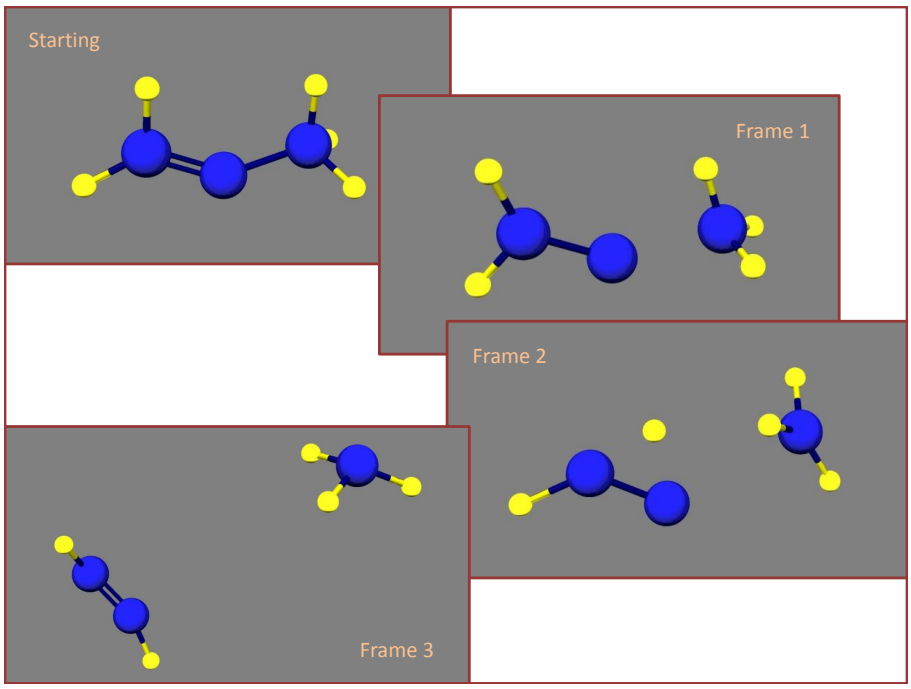

Figure 2.5: Frames of a sample trajectory started with CH_3CCH_2 and produced acetylene HCCH via the intermediate state of vinylidene H_2CC and CH_3 (**Frame 1**). **Frame 2** and **Frame 3** show the roaming mechanism of hydrogen atom producing acetylene from vinylidene.

It is important to investigate why the vinylidene mechanism is so important, even though this mechanism traverses a barrier that is 26.7 kcal/mole higher than the highest transition state of both hydrogen shift mechanisms (TS4 of Fig. 2.1). As a first step to elucidate this, we ran trajectories starting at LM1 as a function of total energy (instead of fixed 248 nm photon energy). We determined the total rate of reaction from LM1 and the quantum yields for dissociation to methyl via the vinylidene mechanism and the mechanism requiring a second 1,2 hydrogen shift. The rate for a specific mechanism is given by the product of the overall rate and the quantum yield for that mechanism. Fig. 2.6 plots the rates as functions of excitation energy for both double 1,2 hydrogen shift and vinylidene mechanisms. From this analysis, it is clear that the double 1,2 hydrogen shift mechanism dominates at very low energies, but at the higher energies (relevant to the 248 nm photodissociation and even higher excitation energy), the vinylidene channel dominates. This phenomenon can be interpreted by the activated complex theory, which states that the reaction rate from the same reactants at a given temperature is proportional to the total partition function (of all degrees of freedom) of the activated complex.[51] Quantum mechanically, the "width" of a potential well is directly proportional to the states being accessible within that well (at a given temperature) and the value of the partition function; since by definition a partition function is a measure of the extent to which a quantum mechanical substance is able to escape from the ground state within a potential well. This is schematically illustrated in Fig. 2.7 for one sample degree of freedom (not drawn in scale) of both vinylidene and the second 1,2 hydrogen shift mechanisms. At 248 nm photon energy, Fig. 2.6 indicates that the reaction rates are approximately the same for both mechanisms, so are the number of accessible states in both wells in Fig. 2.7, and thus so are

the activated partition functions. As the excitation energy increases, states in the "loose" vinylidene well become more quickly accessible than those in the "tight" TS4 well; this therefore leads to the difference in reaction rates as shown in Fig. 2.6. We attempted to find a transition state barrier between LM1 and the vinylidene formation, but it appeared that there was simply a monotonic increase in energy between the former and latter. Direct but limited *ab initio* calculations of the dissociation from LM1 to vinylidene indicated that this dissociation has no barrier beyond that imposed by the endoergicity.

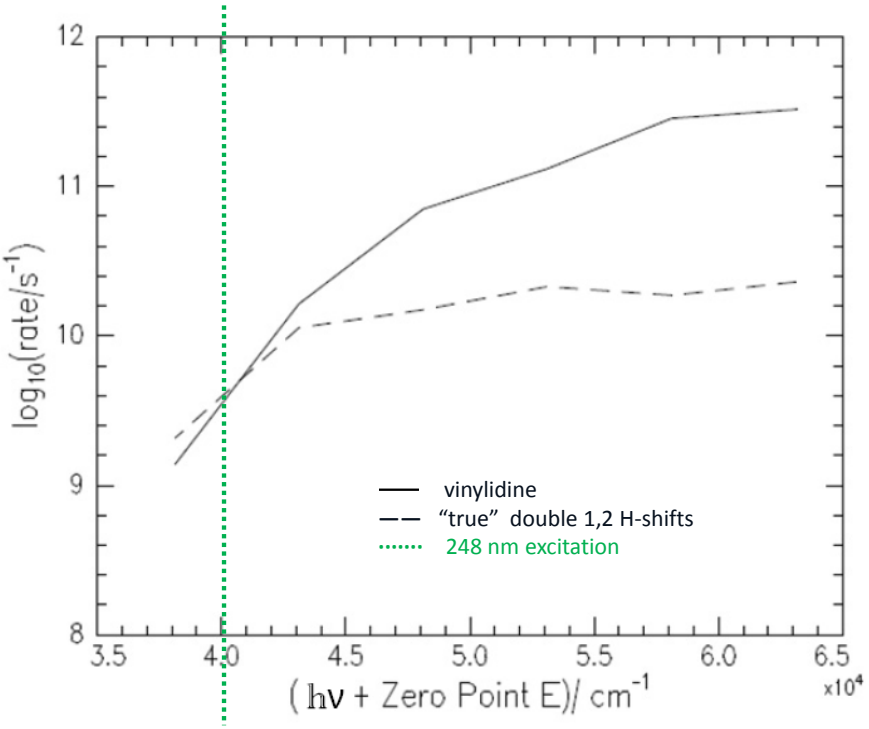

Figure 2.6: Comparison in reaction rates as functions of excitation energy of the double 1,2 hydrogen shift and vinylidene mechanisms.

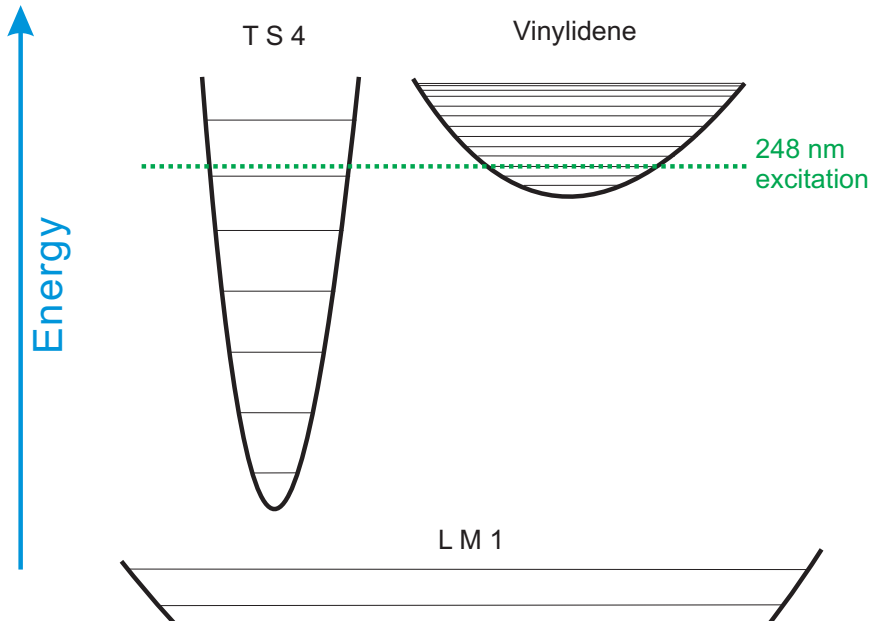

Figure 2.7: Schematic illustration of the difference between transition to the second 1,2 hydrogen shift and vinylidene formation in terms of excitation energy (not drawn in scale).

2.3.3 Angular Distributions and Anisotropy

The angular momentum distributions for methyl and acetylene formed from trajectories traversing the LM2 potential energy well (both 1,3 shift and double 1,2 shifts) are shown in Fig. 2.8. Also shown are calculated values of $\beta_0^0(22)$ for each of the two products. The acetylene was more rotationally excited than the methyl, and the peak of the acetylene rotational distribution is at $J \approx 28$. For rotational levels in which the rotation of methyl did not contribute, the rotation of the acetylene was balanced by the orbital angular momentum, so that $\beta_0^0(22)$ ≈ 0.5, indicating that **v** and **J** are nearly perpendicular.

The anisotropy parameter for dissociations producing methyl and acetylene from trajectories traversing the LM2 potential energy well was calculated to be β = 0.66. For dissociations producing methyl and acetylene from trajectories traversing the LM1 potential energy well (vinylidene and double 1,2 shift mechanisms) the value of the anisotropy parameter was also calculated to be β = 0.66.

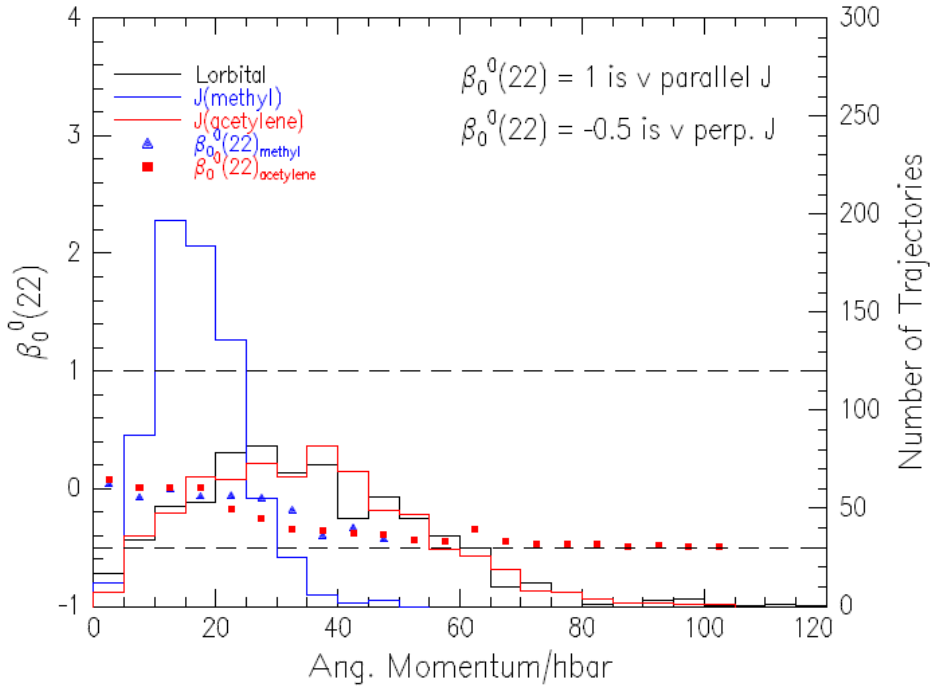

Figure 2.8: Angular momentum distribution and **v-J** correlation for methyl and acetylene produced by trajectories passing through LM2. The blue line is the methyl angular momentum distribution; the black line is the orbital angular momentum distribution, and the red line is the acetylene distribution. $\beta_0^0(22)$ values as a function of **J** are given for methyl (triangles) and acetylene (squares).

2.3.4 Dissociation Time Scale

The one experimental area where it was not easy to reconcile the trajectory results with experiment concerns the dissociation time scale. The top panel of Fig. 2.9 shows the distribution of number of trajectories (starting at allyl global minimum, including both hydrogen and methyl elimination channels) dissociated in each time interval of 0.12 fs, while the bottom panel shows the $1/e$ decay time fitting of the remaining undissociated trajectories after each time interval. The trajectories gave a $1/e$ lifetime of ~16 ps and a dissociation rate of 6.3×10^{10} s^{-1}. In contrast, Deyerl et al. [22,50] measured and calculated a rate on the order of 4.8×10^{8} s^{-1} and saw changes in the H-vs-D ratio for dissociation of 2-deuteroallyl at times as long as 100 ns. Although there is no obvious way to reconcile these measurements, which differ by several orders of magnitude, it should be noted that the trajectories were run on the ground state surface, whereas the initial excitation was to an excited surface. From the widths of rotational lines in the excitation spectra,[13,15,52] Minsek et al. estimated that the internal conversion takes on the order of 20 ps. It was conceivable that some fraction of the population proceeded through intersystem crossing to a long-lived quartet state measured by Deyerl et al.. However, to give a hydrogen signal that was still small on the nanosecond scale, the fraction of dissociations that followed this hypothetical path would have to be close to 100 %. This explanation would be at odds with the observations that dynamics on the ground state surface correctly predicted branching ratios. It should be noted that the dynamics on the excited state remains unknown, so that it was unclear where population was transferred from the excited state to the ground state. The trajectory calculations assumed that the initial geometry on the ground state was that of the global minimum. Dissociation lifetime analysis similar to Fig. 2.9 but

started at CH_2CDCH_2 global minimum gave $1/e$ lifetime of ~23 ps and dissociaton rate of 4.4×10^{10} s^{-1}.

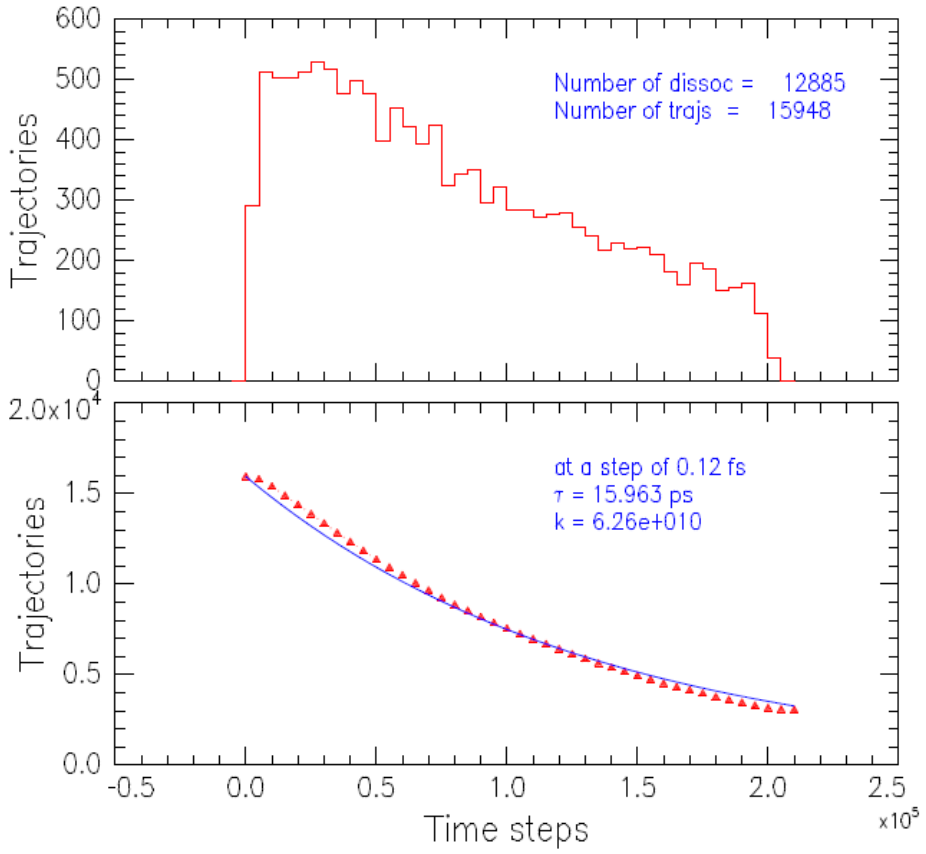

Figure 2.9: Dissociation time scale of allyl radical. (**Top**) Distribution of number of trajectories dissociated in each time interval of 0.12 fs. (**Bottom**) Fitting of remaining undissociated trajectories after each time interval.

2.3.5 "Roaming" Mechanisms

From a broader perspective, the allyl dissociation has similarities to a number of dissociations recently characterized by "roaming" mechanisms.[53–61] For example, in both formaldehyde and acetaldehyde, it was found that, in addition to direct dissociation over the lowest-energy barrier to form H_2 + CO or CH_4 + CO, a second channel opens up at somewhat higher energy in which the nearly dissociating fragment, H or CH_3, respectively, returns to abstract a hydrogen from HCO. The same products are formed but by different detailed reaction paths and with different internal energy distributions. What the H_2CC mechanism for allyl dissociation has in common with the roaming mechanisms in formaldehyde and acetaldehyde is a very loose transition state as discussed in the previous section. As soon as the energy is sufficient to reach this barrier, most of the trajectories dissociate via the path over that barrier, even though it is of higher energy.

CHAPTER 3

VELOCITY-MAP-IMAGING

3.1 Experimental

3.1.1 Overview

Fig. 3.1 (not drawn to scale) describes the velocity-map-imaging apparatus in **`time`** (viewed from left to right), *e.g.* the dissociation and REMPI lasers are spatially overlapped but with timing delay in between. The apparatus consists of a source chamber and a reaction chamber, separated by a 0.5 mm diameter skimmer, followed by a ~ 15 cm flight tube to the detector, which consists of a Chevron microchannel plate (MCP) assembly backed by a phosphor screen. When collecting data images, a charge-coupled device (CCD) Sony XC-EI50 camera is placed outside the reaction chamber with its focus on the phosphor output surface. The front face of the MCP ion detector is held at ~ 1000 V until the appropriate time for the signal of interest, *e.g.* CH_3 ions, arrive. It is then gated (up to 1900V depending on signal intensity with a 150 ns width) in order to accelerate the ions into the MCP and to detect only the ion of interest. When performing wavelength or timing scans, a photomultiplier tube which was assembled by previous members of the group, was placed directly outside the phosphor output surface. The source chamber is pumped by a 6-inch diffusion pump (Varian VHS-6), and the reaction chamber is pumped by a turbomolecular pump (Oerlikon TURBOVAC 600C) with a typical molecular "beam on" pressure of 1×10^{-6} torr.

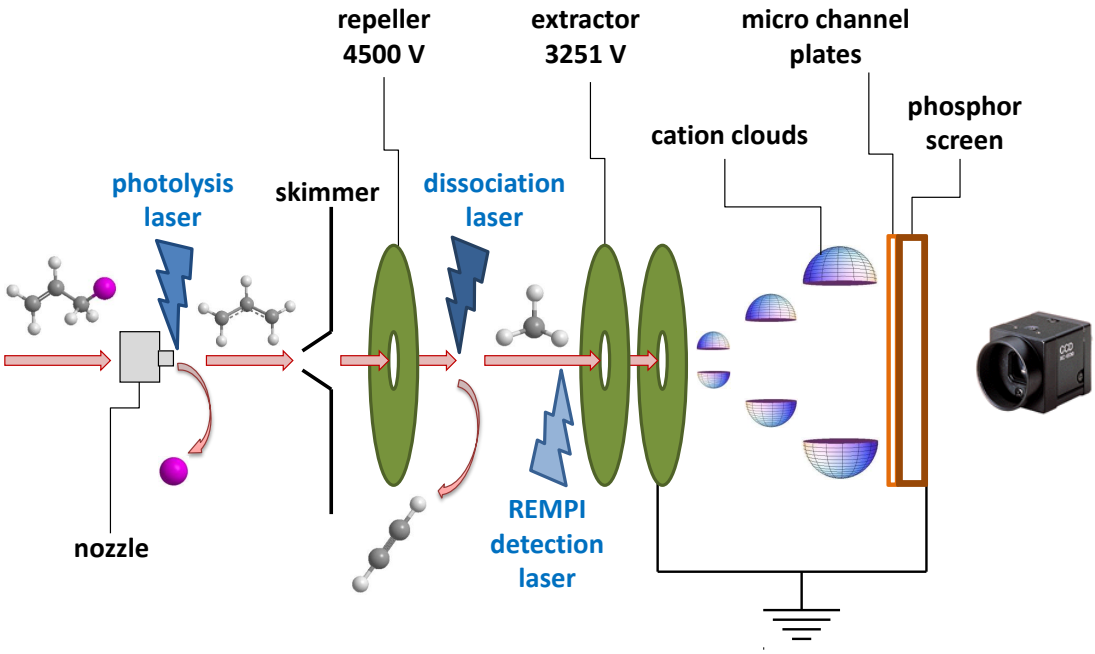

Figure 3.1: Schematic description of the velocity-map-imaging experiment on CH_3 from 248 nm dissociation of C_3H_5I in **time**, *e.g.* the dissociation and REMPI lasers are in reality spatially overlapped but with timing delay in between (not drawn to scale).

3.1.2 The Molecular Beam

The precursor, allyl iodide (m.p. = -99°C and b.p. ≈ 101°C), was obtained from Sigma Aldrich (98%) with no further purification and placed in a glass bubbler, which was stationed in a ice-cooled container. The molecular beam was produced by flowing He at pressure of 1 atm over allyl iodide through a pulsed 300 μm piezoelectric nozzle. The 250 μs, 500V pulse applied to the piezoelectric nozzle forming the molecular beam was directed into the dissociation chamber through a 0.5 mm diameter skimmer. The C-I bonds of allyl iodide were broken by a 266 nm photolysis laser pulse introduced at the tip of nozzle to produce

allyl radicals. This beam of allyl now entrained in the Helium carrier gas was skimmed by the skimmer 5 cm downstream from the nozzle. The reaction spot in the center of the reaction chamber was 12 cm away from the skimmer.

In order to monitor the effect of the 266 nm photolysis laser and the amount of allyl radicals arriving at the reaction spot, a one-laser allyl REMPI wavelength scanning experiment was first performed at the reaction spot with allyl iodide. The scanning laser (Lambda Physik Scanmate dye laser pumped by a Spectra-Physics Quanta-Ray DCR-3 YAG laser) was ~0.7 mJ/pulse during scanning and tightly focused in order to produce allyl radicals from allyl iodide and immediately ionize them. Fig. 3.2 shows the $\widetilde{B}\,12^1 \leftarrow \widetilde{X}\,^2\mathrm{A}_2$ 1+1 allyl REMPI spectrum. With the allyl 1+1 REMPI wavelength determined, the effect of the 266 nm photolysis laser (Spectra-Physics Quanta-Ray DCR-4 YAG laser) was verified by three laser timing scans plotted together in Fig. 3.3: (1) the red solid line shows the timing scan of the 266 nm photolysis laser at the tip of nozzle followed by 1+1 REMPI detection of allyl radicals in the center of the reaction chamber, (2) the blue dotted line gives the background signal caused by the REMPI laser to produce and ionize allyl radicals all by itself without the photolysis laser, and (3) the green dashed line confirms that the power of the photolysis laser (4 mJ/pulse) was adequate so that it did not further ionize allyl radicals after cleaving the C-I bonds. We found no significant difference in the results plotted in Fig. 3.3 as the polarization of the 266 nm laser varied from parallel to perpendicular to the molecular beam propagating direction.

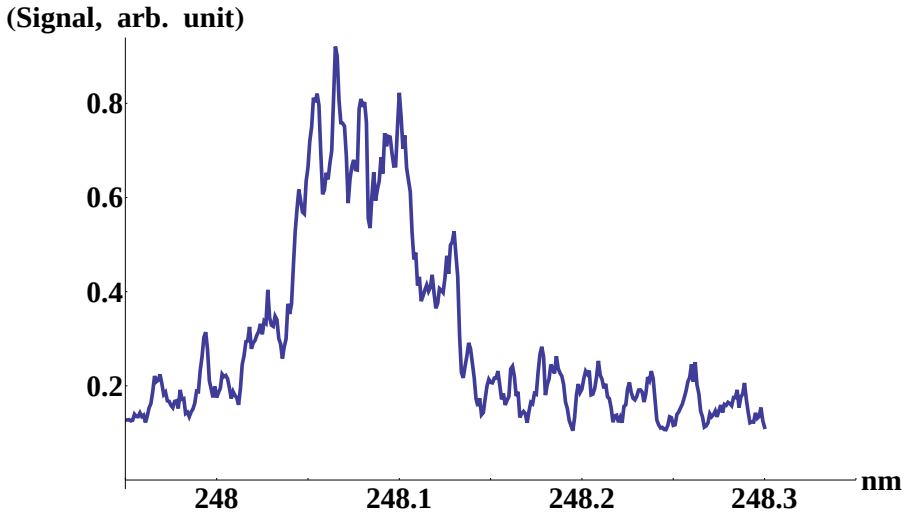

Figure 3.2: $\widetilde{B}\ 12^1 \leftarrow \widetilde{X}\ ^2A_2$ 1+1 allyl REMPI spectrum of one-laser interaction with allyl iodide in the center of the reaction chamber; peak at 248.065nm. The laser was ~0.7 mJ/pulse during the scan and tightly focused.

To determine the rotational temperature of the allyl radicals after the supersonic expansion, we simulated our allyl REMPI spectra, as the Chen group[16] did to their recent experimental results shown in Fig. 1.1 of this thesis, with the program named PGOPHER.[62] The most important parameters for rotational contour simulations are (1) the band origin, (2) the equilibrium rotational constants of the lower and upper vibronic state, and (3) the rotational temperature. The band origin depends totally on the accuracy in calibrating the dye laser grating and thus varies a little among different research groups; we simulated the spectra with the band origin at 40309.9 cm^{-1}. In Fig. 1.1 the simulations by the Chen group were performed by fitting the $\widetilde{B}\ 12^1$ state equilibrium rotational constants; however, we found the constants reported earlier by them[15] [A_e' = 1.619 cm^{-1}, B_e' = 0.351 cm^{-1}, C_e' = 0.288 cm^{-1}] suited our experimental spectra better. Fig. 3.4(a) shows two allyl $\widetilde{B}\ 12^1 \leftarrow \widetilde{X}\ ^2A_2$ 1+1 REMPI spectra: the blue-solid line resulted from the single laser experiment and is the same as Fig. 3.2;

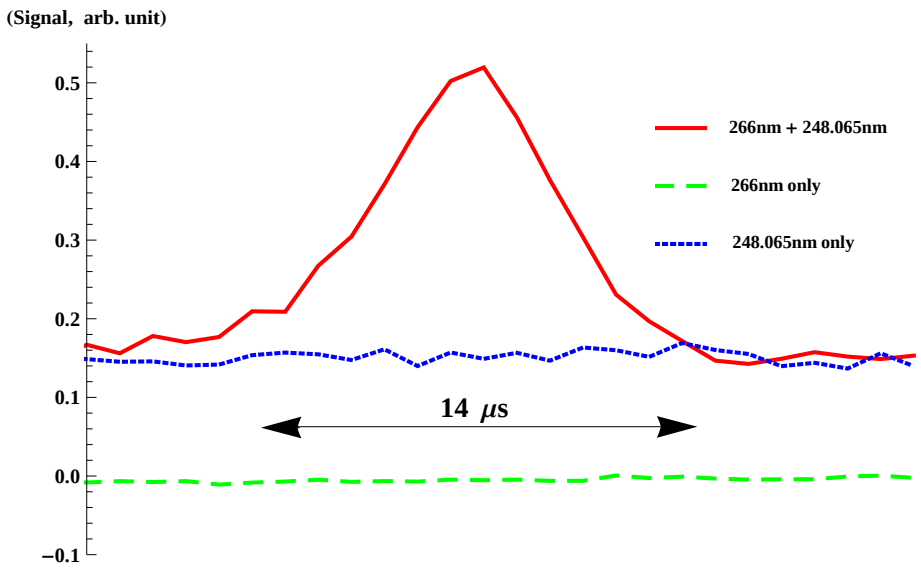

Figure 3.3: Timing scan of the 266 nm photolysis laser at the tip of nozzle as the resulting allyl radicals were probed in the center of the reaction chamber by 1+1 REMPI laser at 248.065 nm (see Fig. 3.2 for the allyl 1+1 REMPI spectrum). The dotted blue line above zero is the background signal from the REMPI laser breaking the C - I bonds then ionizing allyl radicals all by itself. The whole molecular beam width was typically ~250 μs.

the black-dotdashed line resulted from allyl radicals being generated from allyl iodide by the 266 nm photolysis process at the tip of nozzle prior to arriving in the center of the reaction chamber. We found these two REMPI spectra to be almost identical to each other, which indicated that both allyl iodide and free allyl radical were rotationally cooled by the supersonic expansion. Fig. 3.4(b), Fig. 3.4(c), and Fig. 3.4(d) show simulation of this REMPI process at three different rotational temperature, 5 K, 20 K, and 50 K; and we can easily follow the trend of spectral evolution from low to high T_{rot} by considering the T_{rot} = 264 K spectrum shown in Fig. 1.1 (mind the difference in abscissa units). By comparing all the parts in Fig. 3.4, we see that the overall bandwidth of the experimental REMPI spectrum corresponds to $T_{rot} \approx 20$ K, while the gap between

the central peak and the wings corresponds to $T_{rot} \approx 5$ K (as in Fig. 1.1(b)). We can thus at least be confident to say that the allyl radicals were rotationally cooled to $T_{rot} \leq 20$ K upon arriving in the center of the reaction chamber.

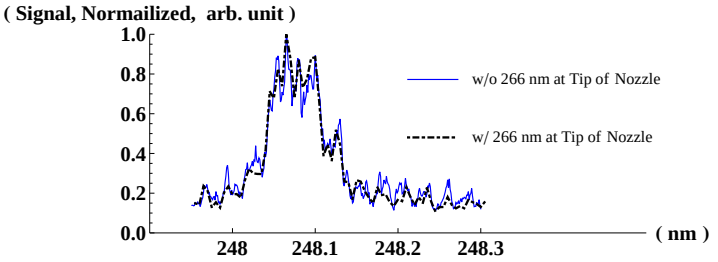

(a)

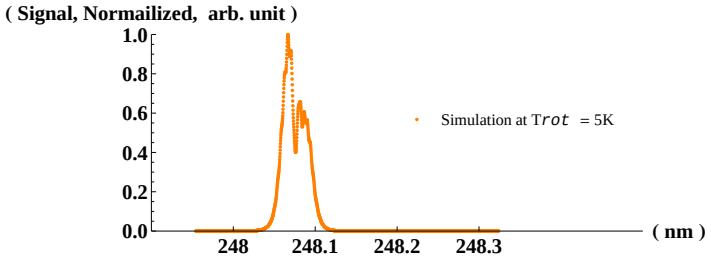

(b)

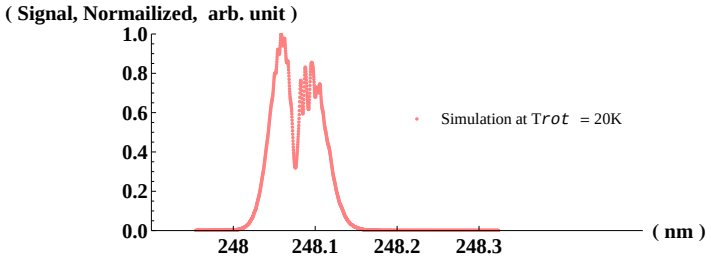

(c)

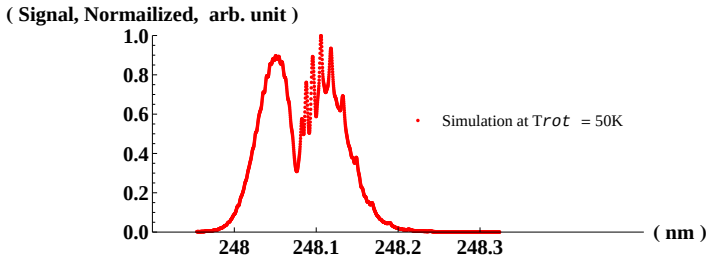

(d)

Figure 3.4: Experimental data and simulation of $\widetilde{B}\ 12^1 \leftarrow \widetilde{X}\ ^2A_2$ 1+1 REMPI spectra of allyl radical: (a) experimental data with and without interaction with 266 nm at tip of nozzle, (b) simulation at T_{rot} = 5 K, (c) simulation at T_{rot} = 20 K, and (d) simulation at T_{rot} = 50 K. See text for simulation parameters.

3.1.3 Methyl Radical Detection

We know from Fig. 3.3 that the 266 nm photolysis of allyl iodide at the tip of nozzle successfully generates a bundle of allyl radicals that would then undergo supersonic expansion through the skimmer. The process of 248 nm photodissociation of allyl is similar to that was performed in Rome[20] and will be discussed in Sec. 3.2.1. We focus here on the 2+1 REMPI detection scheme of the dissociation fragment of interest: the methyl radical. As discussed in Sec. 1.2, we are particularly interested in methyl radicals in the out-of-plane "umbrella" bending mode. The 2+1 REMPI spectra have been obtained previously by our group[25] as shown in Fig. 1.6 of this thesis. We have obtained the same 2+1 methyl $3p\ ^2\mathrm{A}_2'' \leftarrow 2p\ ^2\mathrm{A}_2''$ 0_0^0, 2_1^1, and 2_2^2 REMPI spectra of the 248 nm photodissociation of methyl iodide in the center of the reaction chamber. The 248 nm dissociation photon, ~2 mJ/pulse and unfocused, was provided by an excimer laser (Lambda Physik Compex 201) operating with KrF gas. It was necessary to first measure the correct timing for the 248 nm photon to arrive at the reaction spot. Since the 0_0^0 transition was strong and easy to obtain, a rough, tightly-focused one-laser REMPI scan was performed on methyl iodide to give the approximate peak wavelength of this 0_0^0 transition. A timing scan of the 248 nm laser was then performed with this methyl 0_0^0 probing wavelength. Finally, three detailed ($\Delta\lambda = 0.001$ nm) methyl $3p\ ^2\mathrm{A}_2'' \leftarrow 2p\ ^2\mathrm{A}_2''$ 2+1 REMPI spectra for the 0_0^0, 2_1^1, and 2_2^2 vibronic transition from the 248 nm dissociation of methyl iodide were obtained with the correct 248 nm laser timing and are shown in Figures 3.5, 3.6 and 3.7.

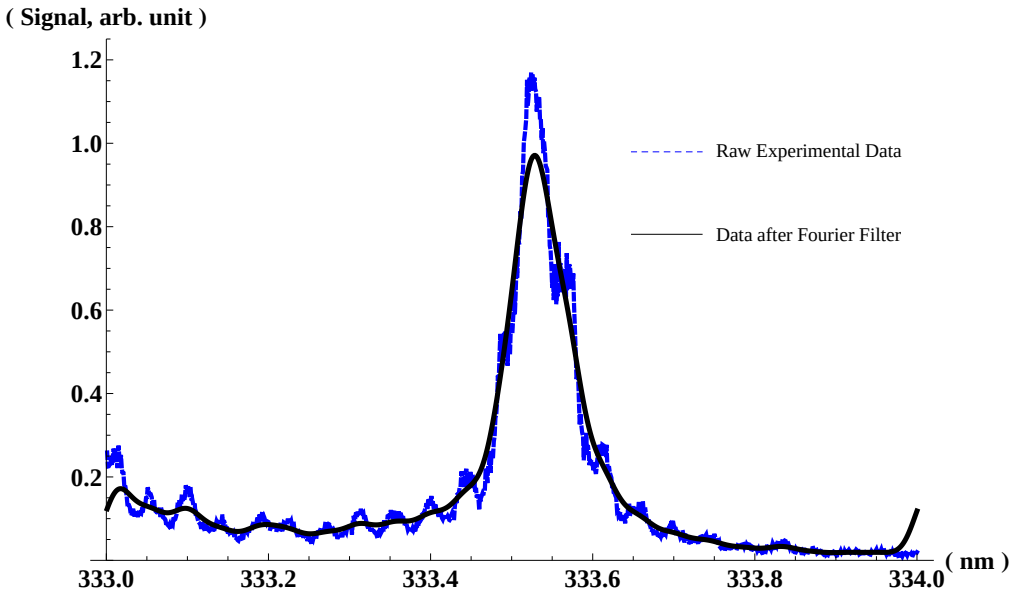

(a) 0_0^0 raw and Fourier filtered signal

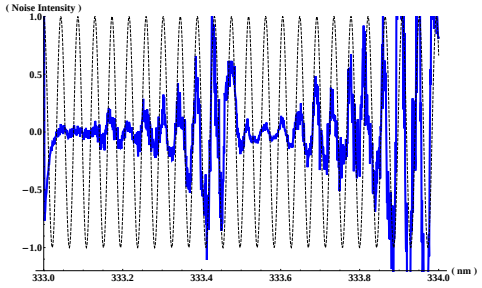

(b) 0_0^0 Fourier filtered noise

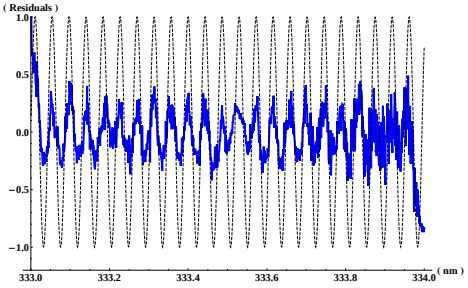

(c) 0_0^0 residuals

Figure 3.5: **(a)** Raw and Fourier filtered 2+1 REMPI spectra of methyl radical produced in the 248 nm photodissociation of CH_3I and probed on the $3p\ ^2A_2'' \leftarrow 2p\ ^2A_2''\ 0_0^0$ transition **(b)** Instrumental noise deleted by the Fourier filter and unweighted by filtered signal intensity. The dashed background is a frequency and phased matched sine function. **(c)** Residuals between the filtered and unfiltered signal and unweighted by filtered signal intensity. The dashed background is a frequency and phased matched sine function.

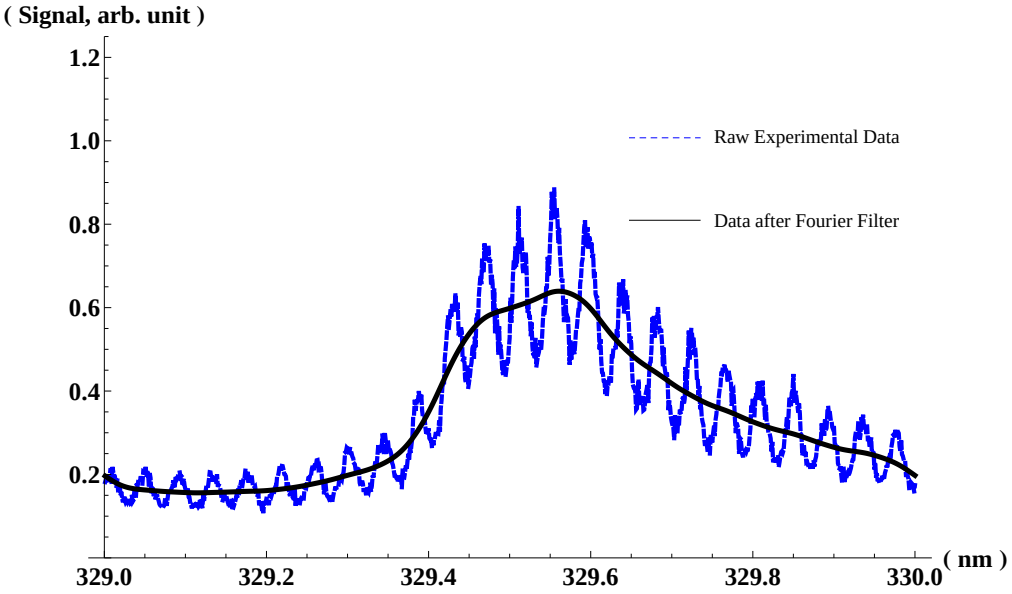

(a) 2_1^1 raw and Fourier filtered signal

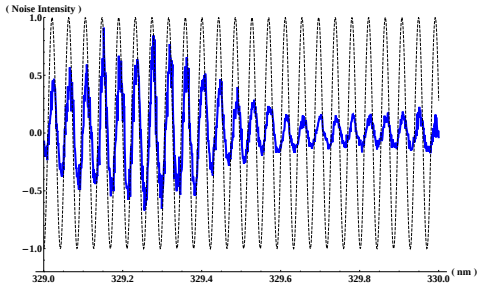

(b) 2_1^1 Fourier filtered noise

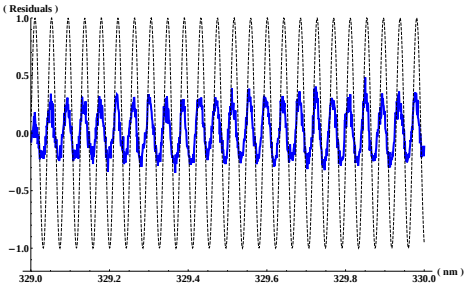

(c) 2_1^1 residuals

Figure 3.6: **(a)** Raw and Fourier filtered 2+1 REMPI spectra of methyl radical produced in the 248 nm photodissociation of CH_3I and probed on the $3p\ ^2A_2'' \leftarrow 2p\ ^2A_2''\ 2_1^1$ transition **(b)** Instrumental noise deleted by the Fourier filter and unweighted by filtered signal intensity. The dashed background is a frequency and phased matched sine function. **(c)** Residuals between the filtered and unfiltered signal and unweighted by filtered signal intensity. The dashed background is a frequency and phased matched sine function.

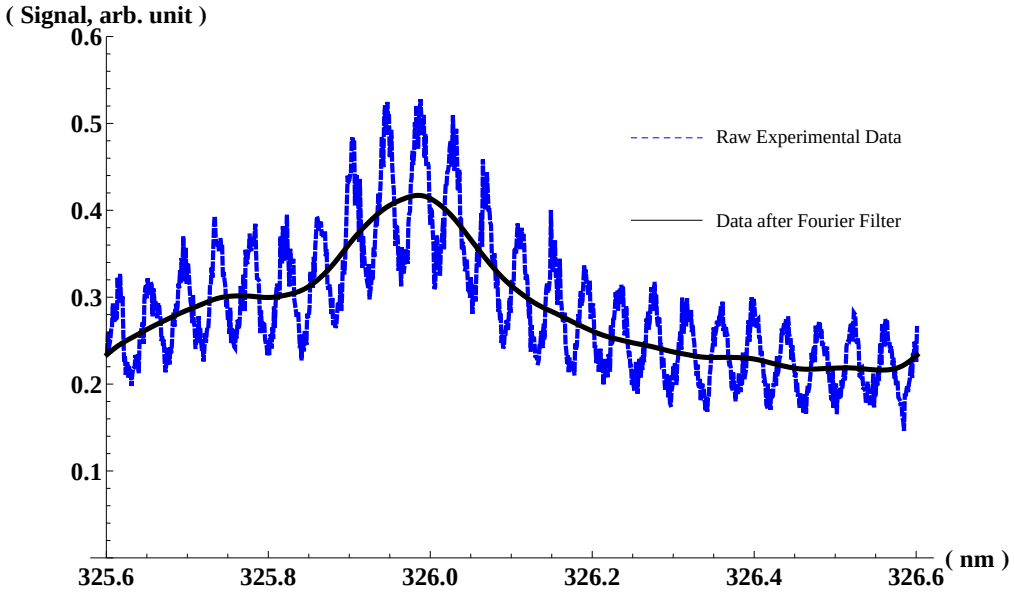

(a) 2_2^2 raw and Fourier filtered signal

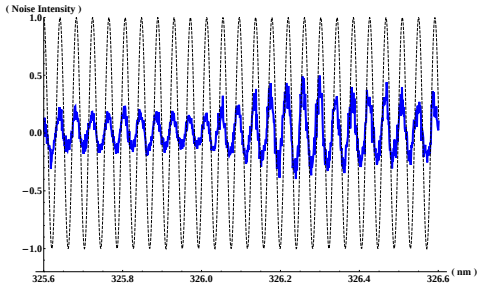

(b) 2_2^2 Fourier Filtered Noise

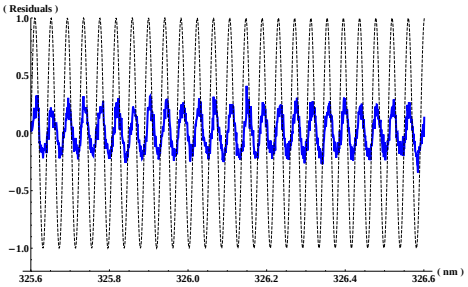

(c) 2_2^2 Residuals

Figure 3.7: **(a)** Raw and Fourier filtered 2+1 REMPI spectra of methyl radical produced in the 248 nm photodissociation of CH_3I and probed on the $3p\ ^2A_2'' \leftarrow 2p\ ^2A_2''\ 2_2^2$ transition **(b)** Instrumental noise deleted by the Fourier filter and unweighted by filtered signal intensity. The dashed background is a frequency and phased matched sine function. **(c)** Residuals between the filtered and unfiltered signal. The dashed background is a frequency and phased matched sine function.

One can easily recognize in all of the raw spectra in Figures 3.5(a), 3.6(a) and 3.7(a) that there was a high frequency oscillation embedded in the real signal. This instrumental noise remained existing in repeated scans and might possibly come from the motion of the grating of the dye laser or the doubling crystal, or even the correlation motion between the two while scanning. Since this pattern was not observed in the allyl REMPI spectrum around 248 nm shown in Fig. 3.2, it was highly possible that this instrumental noise was due to the motion of grating at this particular order corresponding to the methyl REMPI wavelength scanning range. It was thus necessary to use a Fourier transform filter to delete this noise and present the true signal. The Fourier filtration was performed by *Mathematica* 8.0[63] with the *Experimental Data Analyst 1.2* package. Because of the nature of three photon ionization, the noise and the residuals were also amplified by the intensity of the real signal. The noise (which was filtered out) and the residuals for each REMPI transition were unweighted by the true signal and also presented. To illustrate the regularity in oscillation of the noise and residuals, phase and frequency matched sine functions were plotted in the background, and all of these sine functions in Figures 3.5(b), 3.5(c), 3.6(b), 3.6(c), 3.7(b) and 3.7(c) had nearly identical frequency.

3.1.4 Detector Calibration

The most straightforward method to calibrate a new MCP/phosphor/CCD detector set is to image a simple photochemical process and physically measure the actual dimension of the image. If images of the same or similar process have already been obtained and reported in literature, we should be able to use them to double-check our measurement.

The photodissociation of methyl iodide $CH_3I + h\nu \longrightarrow CH_3 + (\ I \text{ and } I^*\ )$ is one of the the prototypical systems for molecular photodissociation dynamics, and since we obtained the methyl radical detection scheme from the 248 nm dissociation of methyl iodide, it was reasonable to calibrate the detector with this photochemical process. With the 248 nm polarization parallel to the detector surface, we took a 480×640 pixels image of methyl radicals with $v'' = 0$ using the REMPI spectrum shown in Fig. 3.5(a). With repeller voltage at 4500 V and extractor voltage at 3251 V, the CH_3 flight time from the moment of ionization to the moment of arrival at the MCP was 2.46 μs. The dimension of this image was physically measured and compared to the previous 266 nm photodissociation VMI study of methyl iodide by Eppink and Parker. Fig. 3.8(a) shows the raw image, and its kinetic energy release (KER) after transformation by pBasex is plotted in Fig. 3.8(b). There are two CH_3 fragmentation channels, one corresponds to I and the other corresponds to I*. The inner ring, the I* channel, gives a peak at 168.4 pixels on the KER plot and the outer ring, the I channel, gives a peak at 213.3 pixels. Fig. 3.8(c) shows the KER curves of various CH_3 vibrational levels obtained by Eppink and Parker [64] on the 266 nm photodissociation of CH_3I, and the detailed fit for the CH_3 $v'' = 0$ KER curve considering all the possible CH_3 and CH_3I rotations is shown in Fig. 3.8(d).

The experimentally determined C-I bond energy of CH_3I is 55.0 ± 0.3 kcal/mole,[65] and according to the Coherent Laser Company (former Lambda Physik) the spectral range of the 248 nm output photon from our Compex 201 excimer laser is ± 0.2 nm. The theoretical upper bound speed for CH_3 of the I* channel is thus 4,362 m/s. Physical measurement of the 480 × 640 pixels imaging area with a ruler (Fig. 3.8(e)) gives an estimate of 4.70 ± 0.05 cm / 640 pixels = 7.30 ± 0.08 $\times 10^{-5}$ m/pixel, which indicates the speed of CH_3 in the I* channel to be 5,090 ± 55 m/s.

Eppink and Parker also found that the maximum speed for the methyl in coincidence with I* was greater than that one would calculate from the bond dissociation energy and the photon energy. In Fig. 3.8(d) their experimental 266 nm dissociation KER of CH_3 $\nu_2 = 0$ in the I* channel is the -○-○ curve; and the E^*_{avl} is the theoretical upper bound KE for CH_3, which should have been the upper bound of the KER curve. The histograms underneath represent the experimentally determined[66,67] rotational energy state distributions for CH_3 in terms of (N',K') from CH_3I dissociation at 266 nm. Due to large mass difference between iodine and methyl, the parent CH_3I rotation about an axis perpendicular to the C-I bond appeared as an extra kinetic energy release. The inset in Fig. 3.8(d) shows an energy histogram for this extra energy release, for a molecular beam temperature of 20 K ($N''_{max} = 5$). Each set of energy histogram (N',K') was shifted for each value of N'' and then broadened for each state to a ~30 meV wide (FWHM) Gaussian peak to represent the apparatus function. The summation of all of these peaks appears as the dashed curve in Fig. 3.8(d). Quantitatively, this extra KER can be deduced from the difference between the upper end of the $\nu_2 = 0$ curve in Fig. 3.8(c) and E^*_{avl} to be 0.47 ± 0.05 eV. This would give our theoretical 248 nm dissociation CH_3 speed in the I* channel to be 4940

$\pm$ 40 m/s, which agrees with the physical measurement shown in Fig. 3.8(e). We thus adopt the conversion factor of $7.30 \pm 0.08 \times 10^{-5}$ m/pixel from the physical measurement for our future experimental studies.

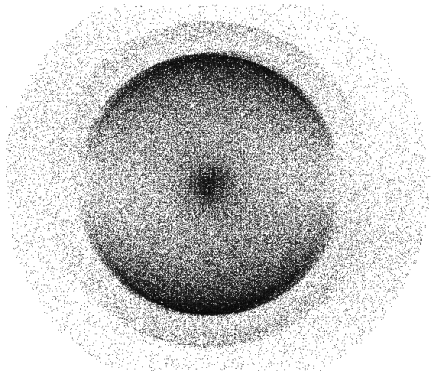

(a)

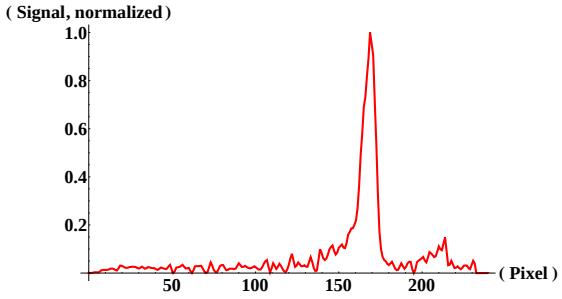

(b)

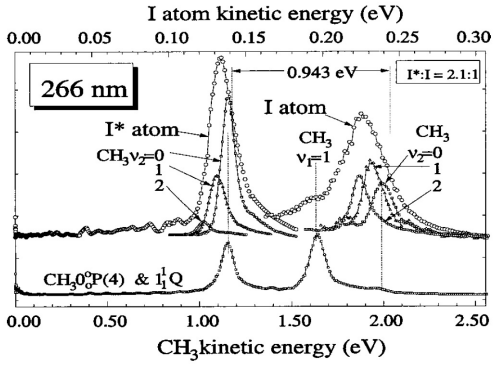

(c)

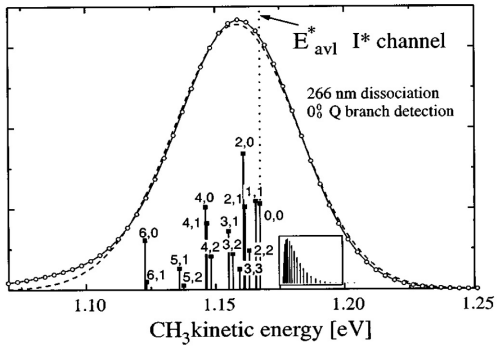

(d)

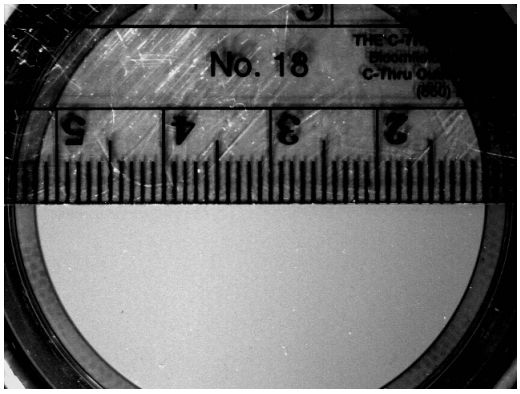

(e)

Figure 3.8: **(a)** Raw 480 × 640 pixels image of methyl radicals with ν_2 = 0 from 248 nm photodissociation of methyl iodide, **(b)** kinetic energy release plot of (a) transformed by pBasex, **(c)** composite kinetic energy release curves for CH_3I dissociation at 266 nm and state-selective detection of different product states,[64] **(d)** kinetic energy release curve for CH_3 ν_2 = 0 radicals formed in the I* channel from (c), and **(e)** physical measurement of the 480 × 640 pixels imaging area. See text for detail.

3.1.5 Image Transformation by PBASEX

The concepts behind the image transformation program PBASEX have be discussed in Section 1.3.2; here the procedural parameters in reconstructing our images, *e.g.* going from Fig. 3.8(a) to Fig. 3.8(b), are presented. A graphical user interface (GUI) version of PBASEX was installed in the cluster *fgate* of the mainframe *Center for Computational Molecular Science and Technology* of Georgia Institute of Technology.[68] After PBASEX loads a data image (in a form of 480 $\times$ 640 matrix), it allows users to manually select the center point of the image; and when it is necessary to enhance the contrast on the low-count areas of the image, it allows users to create a square instead of linear scale colormap display. Before performing the transformation, users need to specify the maximum order of the Legendre polynomials to be used and if it is necessary to include odd Legendre polynomials. As mentioned in Sec. 1.3.2, in our study of one 248 nm photon dissociation of allyl only two terms P_0 and P_2 are needed. The basis set with specified Legendre polynomial has to be created by PBASEX before performing inversion. After the basis set is loaded, the original image is converted to polar coordinates and the fitting of the basis functions to the image is performed. PBASEX generates three files after transformation. The first one is the transformed image which is still in a form of 480 $\times$ 640 matrix; the second one is the translational distribution in two columns, radius (in pixels) and the normalized intensity; and the third one is the angular distribution, which contains radial pixels in the first column, angular parameter A1 corresponding to P_1 in the second column, angular parameter A2 corresponding to P_2 in the third column . . . . etc. In our case, the angular distribution file contains only two columns, radial pixels and A2 parameters (same as β in Eq. 1.10).

3.2 Data Analysis and Discussion

3.2.1 Experimental Summary

Let us go back to Fig. 3.1 and summarize all the experimental components. The photolysis generation of allyl radical at the tip of nozzle by interacting allyl iodide with a 266 nm laser beam was discussed in Section 3.1.2. The timing between the 266 nm photolysis laser and the 248 nm dissociation laser was set according to Fig. 3.3. Allyl could not be properly ionized by the 248 nm beam from the KrF excimer laser as it was in Fig. 3.3 by the dye laser tuned to the peak of its REMPI spectrum (Fig. 3.2) since the excimer laser's spectral range of ± 0.2 nm was too wide. However, Fig. 3.3 could be reproduced by a focused excimer laser beam monitoring the $I^{\oplus}$ instead of allyl cation signal from allyl iodide, since iodine could be easily multi-photon ionized even the photons were not in resonance. In the next step, we set the relative timing between the 248 nm and the REMPI lasers in the center of the reaction chamber the same as the experiment in detecting CH_3 from 248 nm dissociation of methyl iodide (as discussed in Section 3.1.3), since the internal conversion of allyl from the $\widetilde{B}$ electronic state to the $\widetilde{X}$ ground state takes place in only about 22 ps.[21] The actual delay between these two lasers were measured by a photodiode next to the reaction chamber to be ≤ 30 ns (the jittering of the 248 nm laser beam from the KrF excimer laser is ± 5 ns). The polarization of the 248 nm laser was set to be parallel to the MCP surface, while that of the REMPI laser was set to be perpendicular to the MCP surface. We chose this polarization for the REMPI laser to avoid m/e = 15 signal in the image from other production channels of CH_3 caused by the focused REMPI laser (e.g. from the byproduct propyne

H_3C-C≡CH in the hydrogen elimination channel). The repeller and extractor voltages were indicated in Fig. 3.1.

3.2.2 CH_3 ν_2 = 0 Raw Velocity Mapped Images

Fig. 3.9 shows all the raw $\nu_2 = 0$ CH_3 velocity mapped images collected from 248 nm photodissociation of allyl radical and probed by the CH_3 $3p\ ^2A_2'' \leftarrow 2p\ ^2A_2''$ 0_0^0 2 + 1 REMPI. The tightness of focus of the REMPI laser at the reaction spot was varied, and the results are easily recognized from the very loosely focused image in the up-left corner to the rather focused image in the bottom-right corner. If the REMPI laser had been completely focused into the reaction spot, the center blur would have become too large to overshadow the rings. The necessity in increasing the tightness of the REMPI laser focus was simply because of the REMPI cross-section of CH_3 2_1^1 and 2_2^2 transitions are at least seven times smaller than the 0_0^0 transition as shown in Fig 1.6 of this thesis. We thus foresaw having to use a tighter focus for obtaining enough signal to probe methyl radicals with $\nu_2 = 1$ and $\nu_2 = 2$. The tightness of the 0_0^0 REMPI laser focus in obtaining the image shown in the up-left corner was set up by monitoring the CH_3 0_0^0 2 + 1 REMPI signal from 248 nm dissociation of CH_3I and starting de-focusing the REMPI laser step by step until no one-laser (REMPI) signal was detected. This condition would be unfeasible for the 2_1^1 and 2_2^2 2 + 1 REMPI detection of CH_3 from allyl. To avoid observation of anisotropy due to the Doppler effect, each image was collected while scanning the REMPI laser in the range of at least ±10 cm^{-1}.

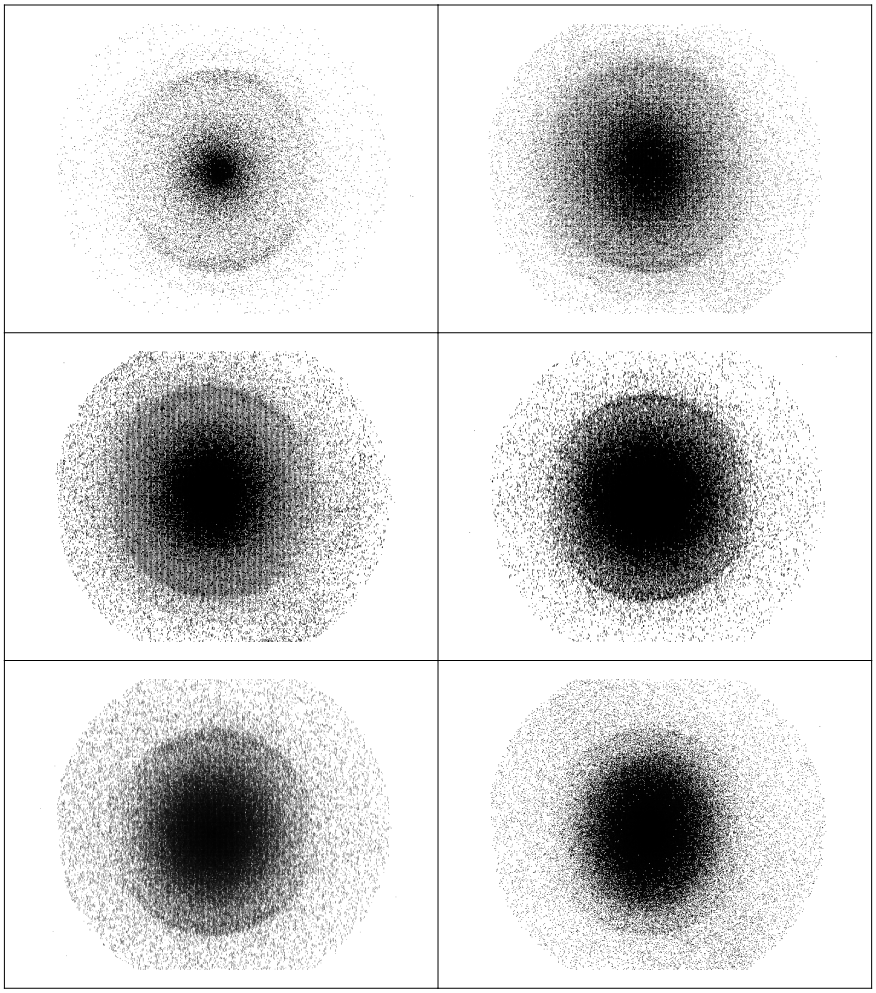

Figure 3.9: Raw CH_3 $\nu_2 = 0$ velocity mapped images from 248 nm photodissociation of allyl radical probed by the CH_3 $3p\ ^2A_2''\ \leftarrow\ 2p\ ^2A_2''\ 0_0^0$ 2 + 1 REMPI.

3.2.3 PBASEX Transformed CH_3 ν_2 = 0 VMI Data

The translational distribution of the CH_3 $\nu_2 = 0$ from 248 nm dissociation of allyl calculated by PBASEX with the lowest laser intensity image (the first one, in the up-left corner of Fig. 3.9) is plotted in Fig. 3.10. We choose this image because of its low signal-to-noise ratio in the translational distribution. In presenting the angular distribution (β), data from this image has rather high signal-to-noise ratio; we instead show the average of the total angular distribution calculated from all of the images in Fig. 3.9.

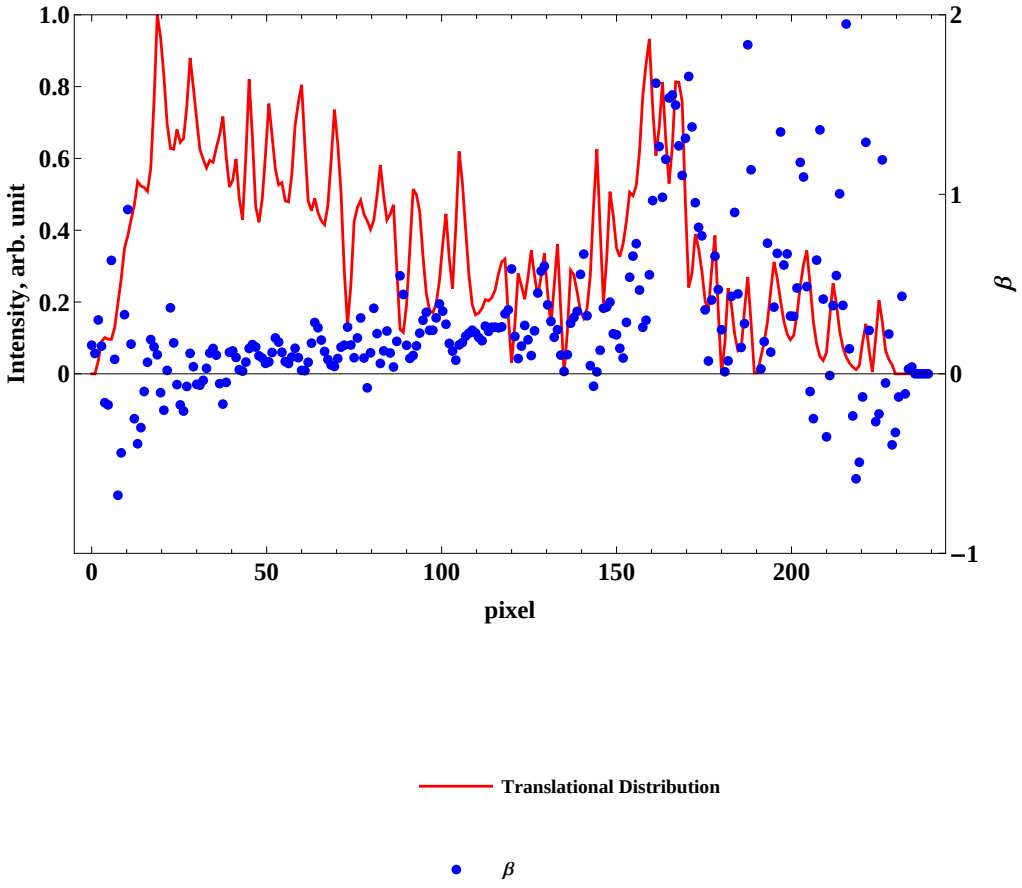

Figure 3.10: PBASEX transformed translational and anisotropy distribution of CH_3 $\nu_2 = 0$ from 248 nm photodissociation of allyl radical. The translational distribution was calculated based on the image with the the lowest laser intensity (the first one, in the up-left corner of Fig 3.9); while the angular distribution was calculated as the average of the total angular distribution from all of the images in Fig 3.9

3.2.4 Translational Distribution Fitting and Analysis

There are two major peaks in the translational distribution in Fig. 3.10; the first one crests at 19.0 pixel and the other crests at ~160 pixel. The first one, judging from the raw image, results from the center blur, *i.e.* the background REMPI noise since the REMPI laser was still somewhat focused for making the three-photon ionization. In fact, the presence of this "peak" was due to the fundamental assumption of PBASEX that all the images possess a cylindrical symmetry with the vertical symmetrical axis in the middle of the image. This assumption forced the transformed translational distribution to start at the origin, which in reality contradicts our background noise since as the raw image shows, the noise has highest intensity at the center. Therefore the pixel position of this noise peak has no scientific meaning, and without this assumption our translational distribution should have its highest point right at the origin. The second one, which represents the ring shown in the raw image, is the CH_3 $\nu_2 = 0$ fragment signal. The width corresponds to the internal energy distribution of the sibling fragment C_2H_2. We fitted this signal by a Gaussian function, and the result is shown in Fig. 3.11 (black dashed line) with the abscissa units converted (using the conversion factor of $7.30 \pm 0.08 \times 10^{-5}$ m/pixel and CH_3 flight time of 2.46 μs) to m/s. We also show the original PBASEX data (red dots) and the data smoothed by a simple average-weighted method (blue solid line). The fitting and smoothing was performed by *Mathematica* 8.0[63] with the *Experimental Data Analyst 1.2* package.

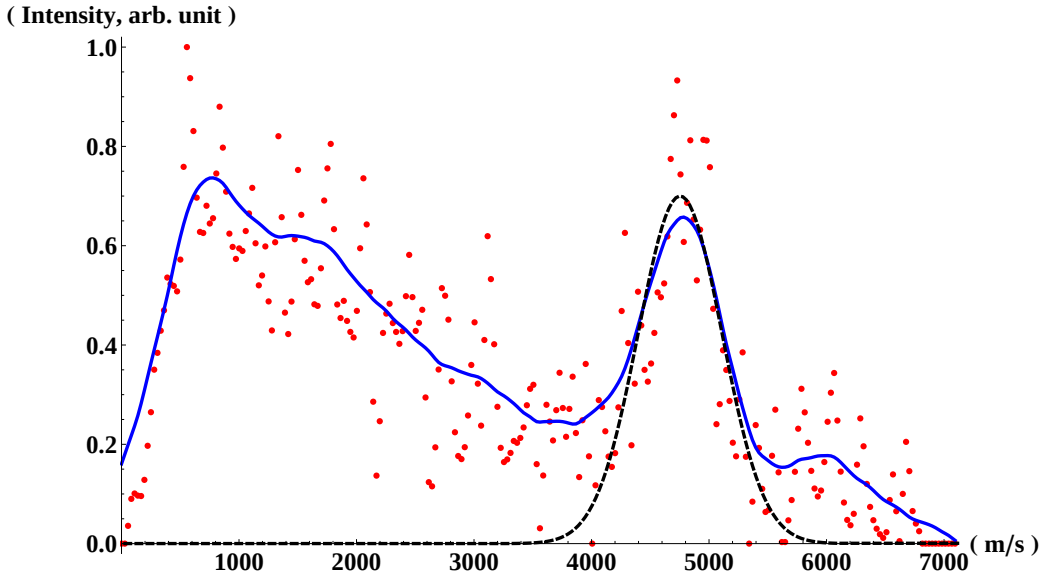

Figure 3.11: Fitting the PBASEX translational distribution of CH_3 $\nu_2 = 0$ from 248 nm photodissociation of allyl radical with a Gaussian function (black dashed line). Also shown are the original PBASEX data (red dots) and the data smoothed by a simple average-weighted method (blue solid line).

We see from the fitted Gaussian in Fig. 3.11 that the peak CH_3 $\nu_2 = 0$ speed is 4754 ± 52 m/s, which corresponds to KER[CH_3] = 40.5 ± 0.9 kcal/mole, and TKER (total kinetic energy release) = 63.9 ± 1.4 kcal/mole. The theoretical available CH_3 speed from the reaction C_3H_5 + 248 nm → CH_3 + C_2H_2 assuming no internal energy for both products is 4879 m/s. Care is needed in interpreting this observed phenomenon, and we here examine four possible cases that our experimental design might have led to:

1. **C_3H_5 + 248 nm → CH_3 + C_2H_2**

   This is the reaction we were seeking to examine, and if we assume no internal energy for both products, it was reasonable to see the observed CH_3 signal falling close to the upper bound of the theoretical available speed. The TKER of 63.9 ± 1.4 kcal/mole also falls on the upper limit in Fig 1.4. As discussed in Section 1.2.1, CH_3 is expected to possess certain vibrational energy in the $\nu = 2$ bending mode due to geometrical change from bent to planar structure; it is therefore not surprising to see that the population of ν_2 v" = 0 is very small compared to other vibrational levels detected in the TOF experiment. However, this means that the acetylene must also be vibrationally cold.

2. **(Highly vibrationally excited C_3H_5 by the 266 nm at the tip of nozzle) + 248 nm → CH_3 + C_2H_2**

   We expect the supersonic expansion to have cooling effect on rotational motions, but not on the vibrational ones. The extra KER[CH_3] could have come from the extra vibrational energy bestowed upon allyl by the 266 nm laser at the tip of nozzle. When we measured the effect of 266 nm laser at the tip of nozzle (Fig. 3.2 and Fig. 3.3) we only scanned the allyl 12^1_0

$\widetilde{B} \leftarrow \widetilde{X}$ transition at ~248 nm. However, in Fig. 2 of ref. 16 both 1 + 1 and 2 + 2 REMPI spectra for 266 nm photolysis generated allyl radicals were presented for a wider region of 39,000 to 45,000 cm^{-1} (256 to 222 nm), which covers the transition from the ground electronic state up to the $\widetilde{D}$ state. All significant transitions were assigned to start from ground v'' = 0 level. Also, in Fig. 3 of ref. 16 pyrolysis generated allyls were observed to be in the ν = 9 v'' = 1 and ν = 12 v'' = 1 levels. This observation leads to a contradiction that if we had observed higher TKER due to the 266 nm photolysis process, the pyrolysis distribution observed in Rome and shown in Fig 1.4 would have peaked at much higher energy.

3. **C_3H_5I + 248 nm → C_3H_5 + I (or I*)** followed by

   C_3H_5 + 248 nm → CH_3 + C_2H_2

   In this particular case we assume that 266 nm had no effect in generating free allyl radicals at the tip of nozzle; what we observed might have been allyl iodide arriving in the center of reaction chamber, followed by the C···I bond being cleaved by one 248 nm photon, and then the allyl radical being excited and dissociated by another 248 nm photon. In other words, the observed high TKE could contain the residual kinetic energy in breaking the C···I bond plus the kinetic energy in methyl dissociated from allyl. This possibility was investigated experimentally by collecting a CH_3 ν_2 = 0 image with all three lasers, immediately followed by collecting another image with equal duration without the 266 nm laser and keeping all the other experimental conditions the same. The results are shown in Fig. 3.12. Significant difference is observed between Fig. 3.12(a) and Fig. 3.12(b); and even there was a small peak resolved by PBASEX without 266 nm at ~172 pixel in Fig. 3.12(c), it has higher translational

energy. The theoretical available CH_3 speed for this two 248 nm photon process is 6580 m/s, which is too much for the reaction we were seeking for in case 1. This investigation concludes that the ring detected was from the free allyl radical generated by the 266 nm photolysis laser at the tip of nozzle.

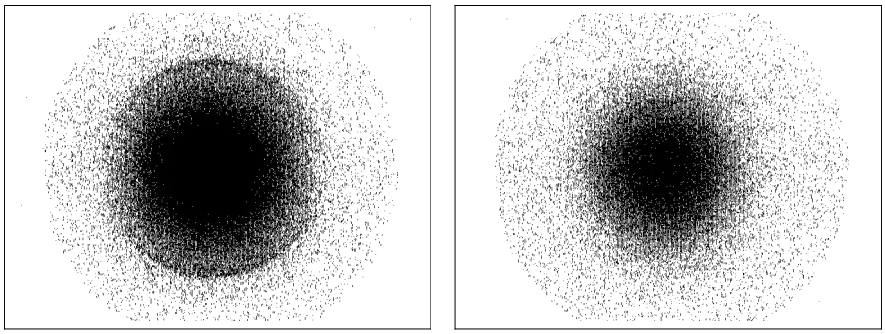

(a) with 266 nm (b) without 266 nm

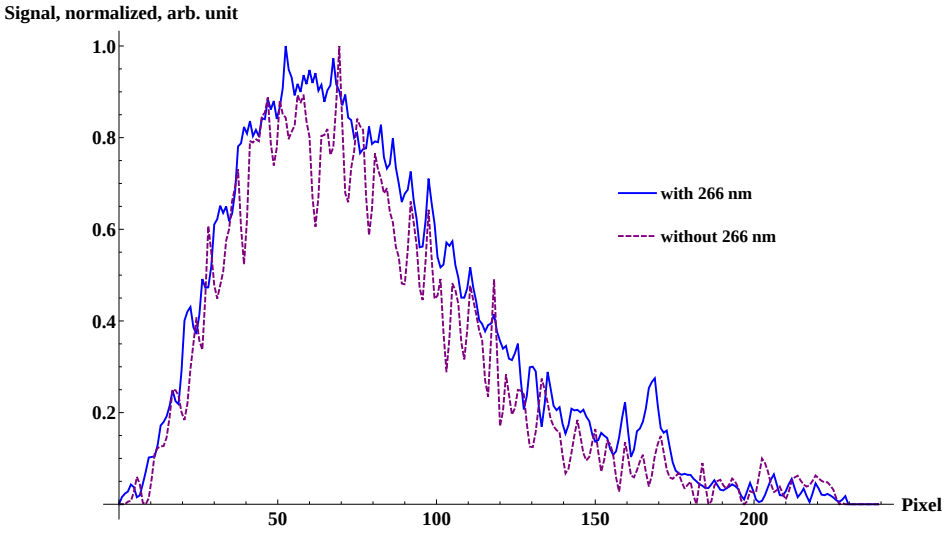

(c)

Figure 3.12: Effect of 266 nm photolysis laser at the tip of nozzle on the CH_3 $\nu_2 = 0$ images: (a) image collected with all three lasers, (b) image collected without 266 nm, and (c) comparison in the translational distribution of (a) and (b).

4. **C_3H_5I + 248 nm → (vibrationally excited C_3H_5) + I (or I*)** followed by **(vibrationally excited C_3H_5) → CH_3 + C_2H_2**

   We can easily exclude this process, since the available CH_3 speed is only 1637 m/s.

3.2.5 Angular Distribution and Anisotropy

The anisotropy parameter, β, can be observed experimentally in the case when the product recoil is fast compared to the parent molecule rotation about the axis perpendicular to the recoil velocity vector. The β values plotted in Fig. 3.10 began to deviate from zero around 160.0 pixel, which indicated that the observed $\nu_2 = 0$ CH_3 dissociation from allyl was anisotropic. To understand this observation, we need to compare the rotational time period of a given temperature T_{rot} in the allyl molecular beam with the dissociation time period. For each rotational degree freedom, this rotational period τ_{rot} (in the unit of second per cycle) can be calculated from the angular speed ω (in the unit of radians per second) by the simple equation $\tau_{rot} = 2\,\pi\,/\,\omega$. The angular speed is related to the rotational energy of a given temperature and the known moment of inertia I (or equivalently the rotational constant R_c) by

$$\varepsilon_{rot}^{1D} = \frac{1}{2}\, I\, \omega^2 = \frac{1}{2}\left(\frac{h}{8\pi c R_c}\right)\omega^2 \quad , \tag{3.1}$$

where c is the speed of light, h is the Planck's constant, and 1D indicates that this equation is for each rotational degree of freedom.

The total (3D) rotational energy can be obtained from the rotational parti-

tion function z_{rot} by

$$\varepsilon_{rot} = - k \frac{\mathrm{d} \ln z_{rot}}{\mathrm{d} \frac{1}{\mathrm{T}_{rot}}} \quad . \tag{3.2}$$

Care is needed in determining the rotational partition function, because quantum mechanically for a C_{2V}(M) near-prolate asymmetric top molecule (recall that the ground state allyl has degree of asymmetry κ = - 0.93 and $A_e \neq B_e \approx C_e$),[69]

$$z_{rot} \approx 2^{-1} \sum_{J=0}^{\infty} (2J + 1)\, e^{-J(J+1)\, \vartheta_{rot}^{B} / \mathrm{T}_{rot}} \sum_{\mathrm{k}_J=-J}^{J} e^{-(A_e - B_e)\, \mathrm{k}_J^2} \quad , \tag{3.3}$$

where the (2J+1) term in the first summation accounts for the space-fixed projection quantum number m_J which runs over the 2J+1 values from -J to J; likewise the molecule-fixed projection quantum number k_J (not to be confused with the Boltzmann constant k) is summed from -J to J, and ϑ_{rot}^{B} is defined by

$$\vartheta_{rot}^{B} = \frac{h \, \mathrm{c} \, B_e}{2 \, k} \quad . \tag{3.4}$$

If we are dealing with cases such as $\mathrm{T}_{rot} >> \vartheta_{rot}^{B}$, the summations in Eq.3.3 can be approximately replaced by integrals, and z_{rot} has a classical value of

$$z_{rot}^{classical} = \frac{\pi^{1/2}}{2} \left(\frac{\mathrm{T}_{rot}}{\vartheta_{A}^{rot}} \right)^{1/2} \left(\frac{\mathrm{T}_{rot}}{\vartheta_{B}^{rot}} \right) \quad , \tag{3.5}$$

and $\varepsilon_{rot}^{classical}$, by Eq. 3.2, becomes (3/2) $k\mathrm{T}_{rot}$ or (1/2) $k\mathrm{T}_{rot}$ per rotational degree of freedom. Otherwise in the cases where $\mathrm{T}_{rot} << \vartheta_{rot}$, we would need to expand

Eq. 3.3 and be worried about the nuclei being bosons or fermions in summing states with even or odd J values.

Since we used the rotational constants reported earlier by the Chen group[15] (A_e' = 1.619 cm^{-1}, B_e' = 0.351 cm^{-1}, C_e' = 0.288 cm^{-1}) to fit our allyl REMPI spectra in Fig. 3.4, here we again use them to calculate, by Eq. 3.4, ϑ_{rot}^{A} = 2.33 K, ϑ_{rot}^{B} = 0.505 K, and ϑ_{rot}^{C} = 0.414 K. For 248 nm dissociation of allyl, the transition moment is along the *y(a)* axis and it is a parallel transition, the fragment angular distribution would only be affected by parent molecule rotations about *z(b)* and *x(c)* axes. The rotational temperature, regardless of allyl being generated by photolysis or pyrolysis, would be therefore much higher than ϑ_{rot}^{B} or ϑ_{rot}^{C}. Three representative T_{rot} at 264 K (as in Fig. 1.1(a) of this thesis for pyrolytically generated allyl), 20 K (the estimated upper limit of our photolytically generated allyl), and 5.5 K (as in Fig. 1.1(b) for the photolytically generated allyl by the Chen group) give τ_{rot} values of 2.93 ps, 10.7 ps, and 20.4 ps for allyl rotations about the *z(b)* and *x(c)* axes. The same results hold even for dissociations from 1-propenyl (LM2 in Fig 2.1 of this thesis) and 2-propenyl (LM1 in Fig 2.1), since their rotational constants do not significantly differ from those of allyl. The simulated trajectories discussed in Chapter 2 mostly dissociated within 10 ps. Thus, if there was a preferred direction for CH_3 fragment ejection in the molecular frame and the parent molecule was rotationally cooled to $T_{rot} < 20$ K, we would observe some, if not all, anisotropy.

3.2.6 Methyl Fragment Rotational Distribution

Even though in Fig. 2.8 of this thesis we saw that, in theory, the methyl fragment was rotationally cold and basically most of the orbital angular momentum was carried away by the acetylene fragment, we would still like to verify this theoretical prediction experimentally. In this section we attempt to examine and compare the REMPI spectra for methyl radicals dissociated from methyl iodide and allyl radical using the program PGOPHER.[62] In Fig. 3.4 our goal was to use PGOPHER in comparing the overall appearances of the allyl 1+1 REMPI spectra and determining the rotational temperature of our allyl molecular beam. Our task here in this section involves more spectroscopic detail. CH_3 $3p\ ^2A_2^{''} \leftarrow 2p\ ^2A_2^{''}$ 2+1 REMPI spectra for the 0_0^0, and 2_1^1 vibronic transitions from the 248 nm dissociation of allyl are shown in Figures 3.13 and 3.14.

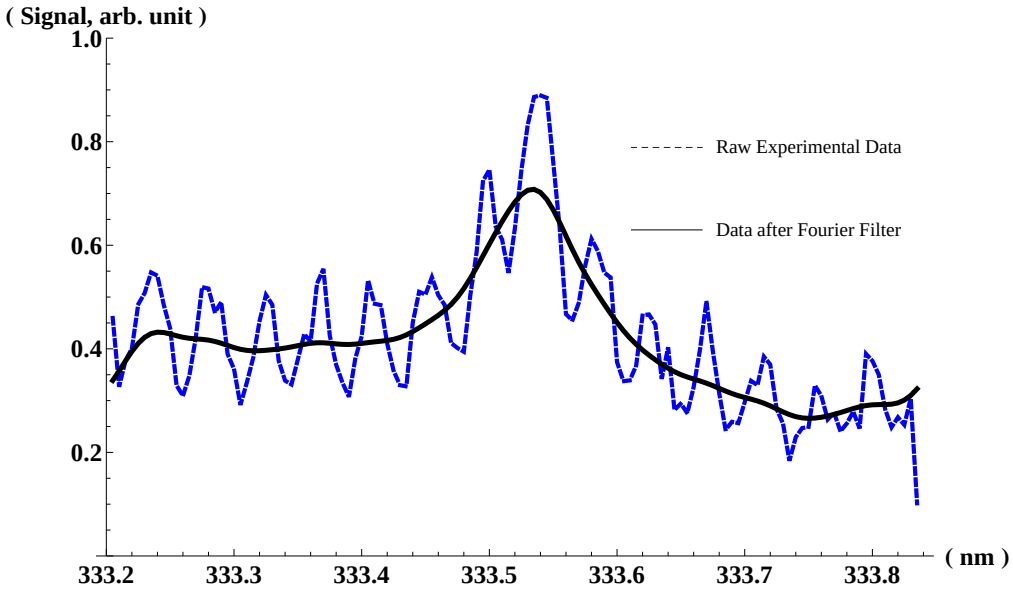

(a) 0_0^0 raw and Fourier filtered signal

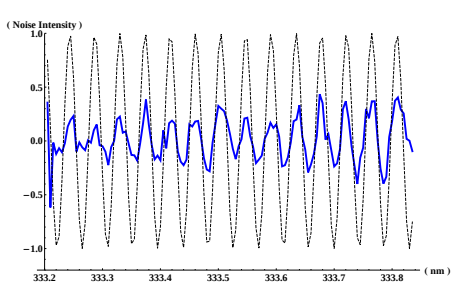

(b) 0_0^0 Fourier filtered noise

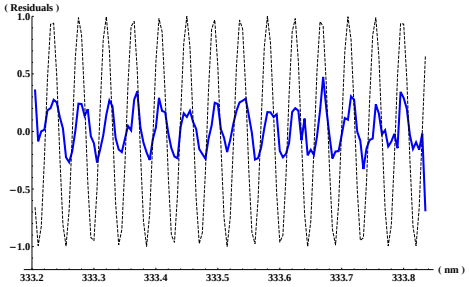

(c) 0_0^0 residuals

Figure 3.13: **(a)** Raw and Fourier filtered 2+1 REMPI spectra of methyl radical produced in the 248 nm photodissociation of allyl and probed on the $3p\ ^2A_2'' \leftarrow 2p\ ^2A_2''\ 0_0^0$ transition **(b)** Instrumental noise deleted by the Fourier filter and unweighted by filtered signal intensity. The dashed background is a frequency and phased matched sine function. **(c)** Residuals between the filtered and unfiltered signal and unweighted by filtered signal intensity. The dashed background is a frequency and phased matched sine function.

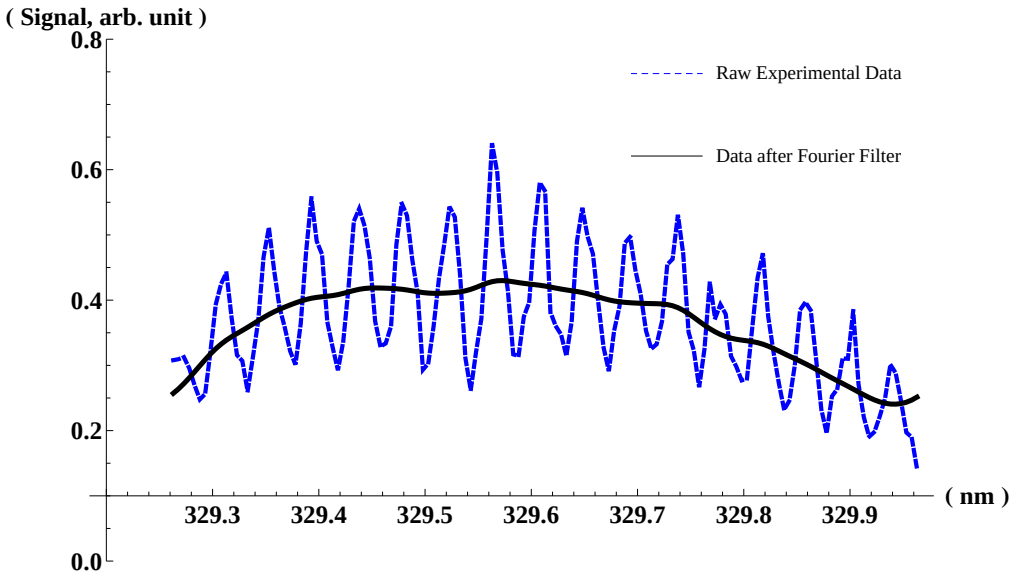

(a) 2_1^1 raw and Fourier filtered signal

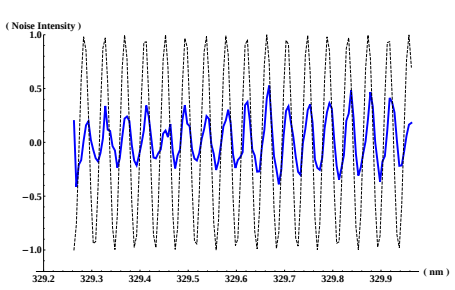

(b) 2_1^1 Fourier filtered noise

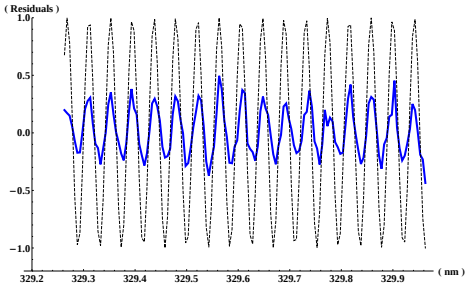

(c) 2_1^1 residuals

Figure 3.14: **(a)** Raw and Fourier filtered 2+1 REMPI spectra of methyl radical produced in the 248 nm photodissociation of allyl and probed on the $3p\ ^2A_2'' \leftarrow 2p\ ^2A_2''\ 2_1^1$ transition **(b)** Instrumental noise deleted by the Fourier filter and unweighted by filtered signal intensity. The dashed background is a frequency and phased matched sine function. **(c)** Residuals between the filtered and unfiltered signal and unweighted by filtered signal intensity. The dashed background is a frequency and phased matched sine function.

CH_3 is a planar symmetric top molecule which belongs to the D_{3h}(M) molecular symmetry group. In order to determine the correct O, P, Q, R, and S branch scales for CH_3 2+1 REMPI spectra of ν_2 = 0, 1, and 2, we would need to consider the nuclear spin statistics, transition selection rules, and the two-photon (instead of single-photon in the allyl case) transition to the resonant state. Simulations of the CH_3 $3p\ ^2A_2'' \leftarrow 2p\ ^2A_2''\ 0_0^0$ REMPI spectrum have been performed by previous members of our group[25] with their own written program code based on equations (1) and (2) of ref. 25 (mind that the 3-*J* symbol should be squared in equation (2) according to the original article). With PGOPHER, users can now easily perform the simulation by inputing the required parameters of the initial and final rovibronic states of the transition followed by pushing the "simulation" button. These parameters include not only the vibronic symmetries of the initial and final states but also the nuclear spin statistical weights and the transition di(multi)pole moments. We discuss in detail how these input parameters for PGOPHER are calculated, and how the selection rules are determined as PGOPHER performs the multi-photon spectroscopic simulation.

For the CH_3 $3p\ ^2A_2'' \leftarrow 2p\ ^2A_2''\ 0_0^0$ 2+1 REMPI transition, both initial and final Rydberg sates have the same vibronic symmetry $^2A_2''$ in D_{3h}(M) with electron spin of ½. The character table of D_{3h}(M) is given in Table 3.1.[18]

For most polyatomic molecules the coupling of the electron spin to the molecular framework is small and a good understanding of the energy level pattern is obtained using a Hund's case (b) basis.[18] This assumption was adopted in the previous CH_3 REMPI simulation[25] and will also be used in performing the simulation in this section. The procedure followed here in determining the nuclear spin statistical weights was discussed in detail in Chapter 8 of ref. 18.

Table 3.1: Molecular symmetry group and point group character table of D_{3h}(M) including the equivalent rotation operations.[18]

D_{3h}(M):	E	(123)	(23)	E^*	$(123)^*$	$(23)^*$	
	1	2	3	1	2	3	
D_{3h}:	E	$2C_3$	$3C_2$	σ_h	$2S_3$	$3\sigma_v$	
Equiv. rot.:	R^0	$R_z^{2\pi/3}$	R_0^{π}	R_z^{π}	$R_z^{-\pi/3}$	$R_{\pi/2}^{\pi}$	
A_1' :	1	1	1	1	1	1	: $\alpha_{zz}, \alpha_{xx}+\alpha_{yy}$
A_1'':	1	1	1	−1	−1	−1	: Γ^*
A_2' :	1	1	−1	1	1	−1	: $\hat{J}_z$
A_2'':	1	1	−1	−1	−1	1	: T_z
E' :	2	−1	0	2	−1	0	: $(T_x, T_y), (\alpha_{xx}-\alpha_{yy}, \alpha_{xy})$
E'':	2	−1	0	−2	1	0	: $(\hat{J}_x, \hat{J}_y), (\alpha_{xz}, \alpha_{yz})$

For the CH_3 $3p\ ^2A_2''$ ← $2p\ ^2A_2''$ 0_0^0 2+1 REMPI transition, we first construct the following eight hydrogen spin functions in Table 3.2, where ↑ is the |½, ½⟩ 'spin up' nuclear spin function for a proton, and ↓ is the |½, -½⟩ 'spin down' function:

Table 3.2: Proton nuclear spin functions of CH_3

m_I	Φ_{ns}		
$\frac{3}{2}$		↑↑↑	
$\frac{1}{2}$	↑↑↓	↑↓↑	↓↑↑
$-\frac{1}{2}$	↑↓↓	↓↑↓	↓↓↑
$-\frac{3}{2}$		↓↓↓	

The hydrogen nuclei are in the order 1, 2, and 3 in these functions, and $m_I = m_1 + m_2 + m_3$ is the total projection quantum number for the proton spins. Clearly both ↑↑↑ and ↓↓↓ are invariant to any permutation operation of the group and have symmetry A_1'. The three $m_I = ½$ spin functions are transformed amongst themselves by the elements of the group, and the representation of D_{3h}(M) generated by these three functions is

$$\begin{array}{cccccc} E & (123) & (23) & E^* & (123)^* & (23)^* \\ 3 & 0 & 1 & 3 & 0 & 1 \end{array} \quad , \tag{3.6}$$

where the operations (23) and (23)* leave the function ↓↑↑ along but interchange the other two, and the operations (123) and (123)* permute all three functions. This representation reduces to the following irreducible representations of D_{3h}(M):

$$A_1' \oplus E' \quad . \tag{3.7}$$

The three $m_I = -½$ spin functions generate the same representations of the D_{3h}(M) group. Therefore the representations generated by the eight hydrogen spin functions are

$$4\,A_1' \oplus 2\,E' \quad , \tag{3.8}$$

with the characters

$$\begin{array}{cccccc} E & (123) & (23) & E^* & (123)^* & (23)^* \\ 8 & 2 & 4 & 8 & 2 & 4 \end{array} \quad . \tag{3.9}$$

Since ^{12}C nucleus has a spin of zero and there is only a single nuclear spin function, the total representations generated by all eight nuclear spin functions of CH_3 are

$$\Gamma_{ns} = 4\,A_1' \oplus 2\,E' \quad . \tag{3.10}$$

The complete internal wavefunction Φ_{int} of CH_3 can only belong to either A_2' or A_2'', since (23) is an odd permutation of fermion nuclei and thus it changes the sign of Φ_{int}. To form a valid internal basis wavefunction we can only combine a rovibronic state Φ_{rve} having symmetry Γ_{rve} in the MS group with a nuclear spin state having symmetry Γ_{ns} in the MS group if the product of these symmetries contains a species Γ_{int} for Φ_{int} allowed by the statistical formula, *i.e.*

$$\Gamma_{\text{rve}} \otimes \Gamma_{\text{ns}} \subset \Gamma_{\text{int}} \quad . \tag{3.11}$$

We proceed by constructing Table 3.3 of all the possible six Γ_{rve} :

Table 3.3: Statistical weights (**sw**) of the rovibronic states of CH_3 in the D_{3h}(M) group.

Γ_{rve}	Γ_{ns}		Γ_{int}		**sw**	Γ_{rve}	Γ_{ns}		Γ_{int}		**sw**
A_1'			A_2'	A_2''	0	A_1''			A_2'	A_2''	0
A_2'	$4A_1'$		A_2'	A_2''	4	A_2''		$4A_1'$	A_2'	A_2''	4
E'	$2E'$		A_2'	A_2''	2	E''		$2E'$	A_2'	A_2''	2

For the first row in Table 3.3, none of the nuclear spin species can be coupled with A_1' or A_1'' of Γ_{rve} to produce either A_2' or A_2'' for Γ_{int}, which leads to statistical weights (**sw**) of zero. In the second row, since A_1' of Γ_{ns} is totally symmetric, it couples with $\Gamma_{rve} = A_2'$ or $\Gamma_{rve} = A_2''$ to give $\Gamma_{int} = A_2'$ or $\Gamma_{int} = A_2''$ with **sw** = 4. Similarly in the third row **sw** = 2 can be deduced if we decompose the following symmetry products:

$$E' \otimes E'' = \{ \; 4 \;\; 1 \;\; 0 \;\; 4 \;\; 1 \;\; 0 \; \} = A_1' \oplus \mathbf{A_2'} \oplus E' \quad , \tag{3.12}$$

and

$$E'' \otimes E' = \{ \; 4 \;\; 1 \;\; 0 \;\; -4 \;\; -1 \;\; 0 \; \} = A_1'' \oplus \mathbf{A_2''} \oplus E'' \quad . \tag{3.13}$$

We have so far considered all the six possible rovibronic symmetries in D_{3h}(M) but only know the vibronic symmetries of the initial and final states of this 0_0^0 transition. The rotational symmetry behind each spectral line determines the selection rule and is yet to be determined. The effect of each operation in D_{3h}(M) on the Euler angles can be deduced from the result of each corresponding equivalent rotation in Table 3.1. Using the notation of Chapter 12 in ref. 18, R_α^π rotates the molecule-fixed (x, y, z) axes through π radians about an axis in the xy plane making an angle α with the z axis (α is measured in a right handed sense about the z axis) and changes the Euler angles from (θ, ϕ, χ) to (π - θ, ϕ + π, 2π - 2α - χ). The rotation R_z^β by β radians about the z axis (measured in a right handed sense about the z) changes the Euler angles to ($\theta, \phi, \chi + \beta$). The representation generated by the symmetric top wavefunction $| J \; 0 \; 0 \rangle$ in D_{3h}(M) is thus (from eq. (12-48) of ref. 18)

$$\begin{array}{cccccc} E & (123) & (23) & E^* & (123)^* & (23)^* \\ 1 & 1 & (-1)^J & 1 & 1 & (-1)^J \end{array} \quad . \tag{3.14}$$

For the pair of functions $| J\ K\ m \rangle$ and $| J\ -K\ m \rangle$ the representation generated is (from eq. (12-49) of of ref. 18)

$$\begin{array}{cccccc} E & (123) & (23) & E^* & (123)^* & (23)^* \\ 2 & 2cos(2\pi\ K/3) & 0 & 2(-1)^K & 2cos(-\pi\ K/3) & 0 \end{array} \quad . \tag{3.15}$$

These representations can be written in terms of the irreducible representations of D_{3h}(M), and these symmetry species, as a function of J and $K = | k |$, are shown in Table 12-5 of ref. 18 and given below in Table 3.4:

Table 3.4: Symmetry species of the rotational wavefunctions of CH_3 in the D_{3h}(M) group.

K	D_{3h}(M)
0 with J even	A_1'
0 with J odd	A_2'
6n ± 1	E''
6n ± 2	E'
6n ± 3	$A_1'' \oplus A_2''$
6n ± 6	$A_1' \oplus A_2'$

In Hund's case (b), the rovibronic and electron spin (rves) symmetry Γ_{rves} of the levels of vibrationless electronic state $^2A_2''$ can be determined by Table 3.4 and is shown in Fig. 18-3 of ref. 18 and Fig. 3.15 of this thesis:

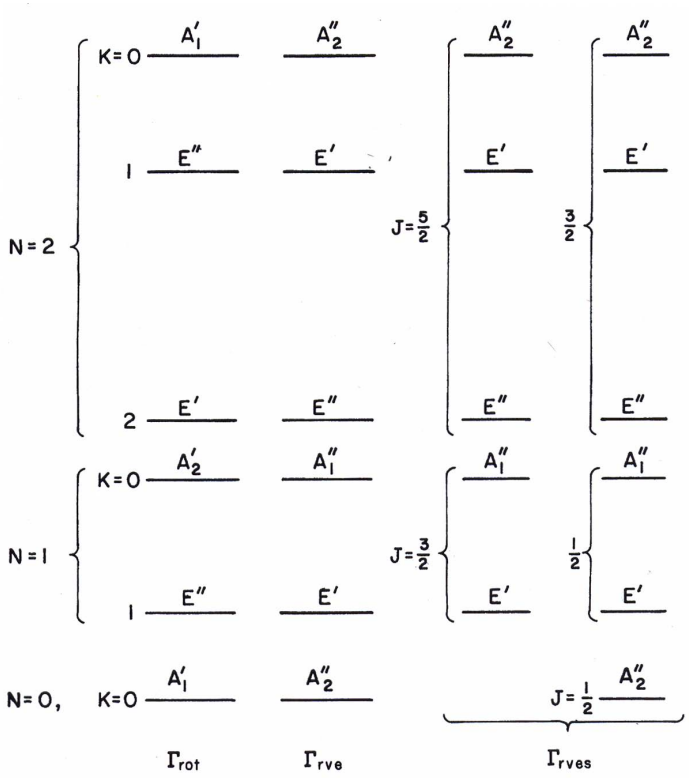

Figure 3.15: The symmetry labels Γ_{rves} for the rovibronic-electron spin energy levels of CH_3 in a $^2A_2''$ vibronic state using Hund's case (b) electron spin functions.[18]

For the two-photon $3p\ ^2A_2'' \leftarrow 2p\ ^2A_2''$ transition it is necessary to have $\Gamma_{ve}' \otimes \Gamma_r' \otimes \Gamma_{ve}'' \otimes \Gamma_r'' = \Gamma_r' \otimes \Gamma_r'' \subset \Gamma^{(s)} = A_1'$ (since both vibronic states have the same symmetry). This requirement leads to the two-photon selection rules from the ground $2p\ ^2A_2''$ vibronic state of methyl radical with Γ_r'' and Γ_r' determined from Fig. 3.15. These rules have been previously determined[70] and is shown in Table 3.5 (we currently are only interested in final vibronic state with A_2'' symmetry):

Table 3.5: Optical selection rules for transitions from the vibrationless $\widetilde{X}\ ^2A_2''$ state of CH_3 to the excited states of other symmetries.[70]

Final vibronic ($\psi_e\psi_v$) state symmetry species	Number of simultaneously absorbed identical photons		
	One photon	Two photons	Three photons
$^2A_1'$	$\Delta K = 0$ $K = 0;\ \Delta N = \pm 1$ $K \neq 0;\ \Delta N = 0, \pm 1$	f[b]	$\Delta K = 0$ $K = 0;\ \Delta N = \pm 1, \pm 3$ $K \neq 0;\ \Delta N = 0, \pm 1, \pm 2, \pm 3$
$^2A_1''$	f	$\Delta K = 0$ $K = 0;\ \Delta N = \pm 1$ $K \neq 0;\ \Delta N = 0, \pm 1, \pm 2$	$\Delta K = \pm 3$ $K'' = 0;\ \Delta N = \pm 1, \pm 3$ $K'' \neq 0;\ \Delta N = 0, \pm 1, \pm 2, \pm 3$
$^2A_2'$	f	f	$\Delta K = 0$ $K = 0;\ \Delta N = 0, \pm 2$ $K \neq 0;\ \Delta N = 0, \pm 1, \pm 2, \pm 3$
$^2A_2''$	f	$\Delta K = 0$ $K = 0;\ \Delta N = 0, \pm 2$ $K \neq 0;\ \Delta N = 0, \pm 1, \pm 2$	$\Delta K = \pm 3$ $K'' = 0;\ \Delta N = 0, \pm 2$ $K'' \neq 0;\ \Delta N = 0, \pm 1, \pm 2, \pm 3$
E'	f	$\Delta K = \Delta l = \pm 1$ $\Delta N = 0, \pm 1, \pm 2$	$\Delta K = 2\,(-\Delta l) = \pm 2$ $\Delta N = 0, \pm 1, \pm 2, \pm 3$
E''	$\Delta K = \Delta l = \pm 1$ $\Delta N = 0, \pm 1$	$\Delta K = 2(-\Delta l) = \pm 2$ $\Delta N = 0, \pm 1, \pm 2$	$\Delta K = \Delta l = \pm 1$ $\Delta N = 0, \pm 1, \pm 2, \pm 3$

[a]Hund's case (b) notation. [b]f = forbidden process.

The last piece of information that needs to be determined before using PGOPHER is the transition moment. Since our current case is not a single photon excitation, we cannot simply use a Cartesian dipole moment. For the CH_3 $3p\ ^2A_2''$ $\leftarrow$ $2p\ ^2A_2''$ 0_0^0 two-photon transition, the transition moment must be totally symmetric in D_{3h}(M). PGOPHER was designed to accept these multi-photon transition moments in terms of the irreducible spherical tensor operators; and the expressions of these operators are given (up to rank 2) in equations (14-109) - (14-114) of ref. 18. These expressions were written in the notation of **Q** in the context of electric quadrupole moments, and symmetries of their corresponding Cartesian components are given in the notation of α in the D_{3h}(M) character table of Table 3.1 of this thesis. As discussed in section 14.3 of ref. 18, we would need to consider six possible tensor operators $\alpha^{(0\ 0)}$, $\alpha^{(2\ 0)}$, $\alpha^{(2\ \pm1)}$, $\alpha^{(2\ \pm2)}$ for the two-photon transition. From Table 3.1 of this thesis, we see that only $\alpha^{(0\ 0)}$ and $\alpha^{(2\ 0)}$, which consist of $\alpha_{\sigma\sigma}$ (σ = x, y, or z), are totally symmetric. The relative strength between $\alpha^{(0\ 0)}$ and $\alpha^{(2\ 0)}$ needs to be determined by actually fitting the experimental data with PGOPHER.

The above discussion is about the CH_3 $3p\ ^2A_2''$ $\leftarrow$ $2p\ ^2A_2''$ 0_0^0 transition, and similar parameters such as the selection rules can be determined for the 2_1^1 and 2_2^2 transitions by the same procedure and noting that the ν_2 our-of-plane bending motion has the vibrational symmetry A_2'' in D_{3h}(M).[71] Equilibrium rotational constants for the ground and several excited Rydberg states of CH_3 can be found in ref. 71.

The bottom panel of Fig. 3.16 shows the experimental data from Fig. 3.5(a) of this thesis (blue-solid curve) and PGOPHER simulation (red-dashed curve) of CH_3 $3p\ ^2A_2''$ $\leftarrow$ $2p\ ^2A_2''$ 0_0^0 REMPI spectrum from 248 nm dissociation of CH_3I; while the top panel shows the theoretical O, P, Q, R, and S branch locations calculated by PGOPHER. The PGOPHER fitting was performed with rotational temperature of 120 K and Gaussian / Lorentzian line width broadening of 10 cm^{-1}. These values were determined in a similar experimet in ref. 25 of 266 nm dissociation of CH_3I and fitted our experimental data well. The relative strength of $\alpha^{(0\ 0)}$: $\alpha^{(2\ 0)}$ was set to be 1.0 : 0.6, and no higher order coupling, *e.g.* centrifugal distortion or Coriolis coupling, was considered. The ordinate of the top panel is quantum number N (which is the same as *J* in Hund's case (b)); and for the Q branches all the K" values were plotted for each N. Besides the dominant Q branch, R(1), R(2), R(3) and S(0) transitions were also observed between 60,000 and 60,050 cm^{-1}.

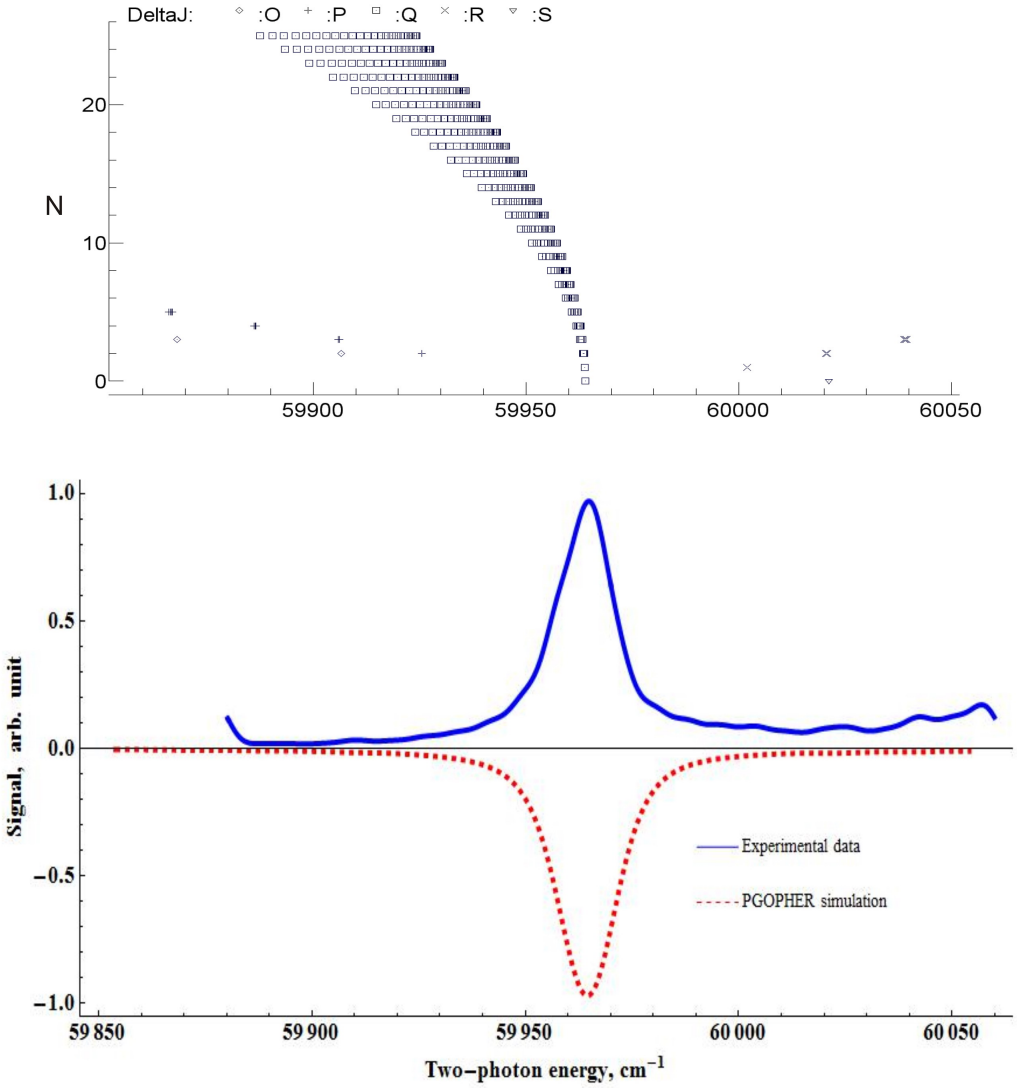

Figure 3.16: Experimental data (blue-solid curve in the bottom panel) and PGOPHER simulation (red-dashed curve in the bottom panel) of CH_3 $3p\ ^2A_2''$ ← $2p\ ^2A_2''$ 0_0^0 REMPI spectrum from 248 nm dissociation of CH_3I. The top panel shows the PGOPHER assignments of the rotational transition branches.

Similarly, CH_3 $3p\ ^2A_2''$ $\leftarrow$ $2p\ ^2A_2''$ 0_0^0 REMPI spectrum from 248 nm dissociation of allyl is given in Fig. 3.17 using the same $\alpha^{(0\ 0)} : \alpha^{(2\ 0)}$ ratio and line width broadening values as Fig. 3.16. The signal to noise ratio in Fig. 3.17 is higher than Fig. 3.16, which corresponds to the difference in the center background blur of the images collected; *c.f.* Fig. 3.8(a) and Fig. 3.9. However, the rotational temperature in Fig. 3.17 was fitted as 400 K instead of 120 K, which indicated rotationally hotter methyl from allyl dissociation than from CH_3I dissociation. In Fig. 2.8 of this thesis, the methyl fragment rotation peaked at $J\approx10$ and vanished at $J\approx28$ in the trajectory calculations. Experimentally in Fig. 3.17, the Q branch peaks at $J\approx6$ and vanishes at $J\approx18$. In fact, the true rotational distribution should vanish at even lower J value due to the line width broadening effect.

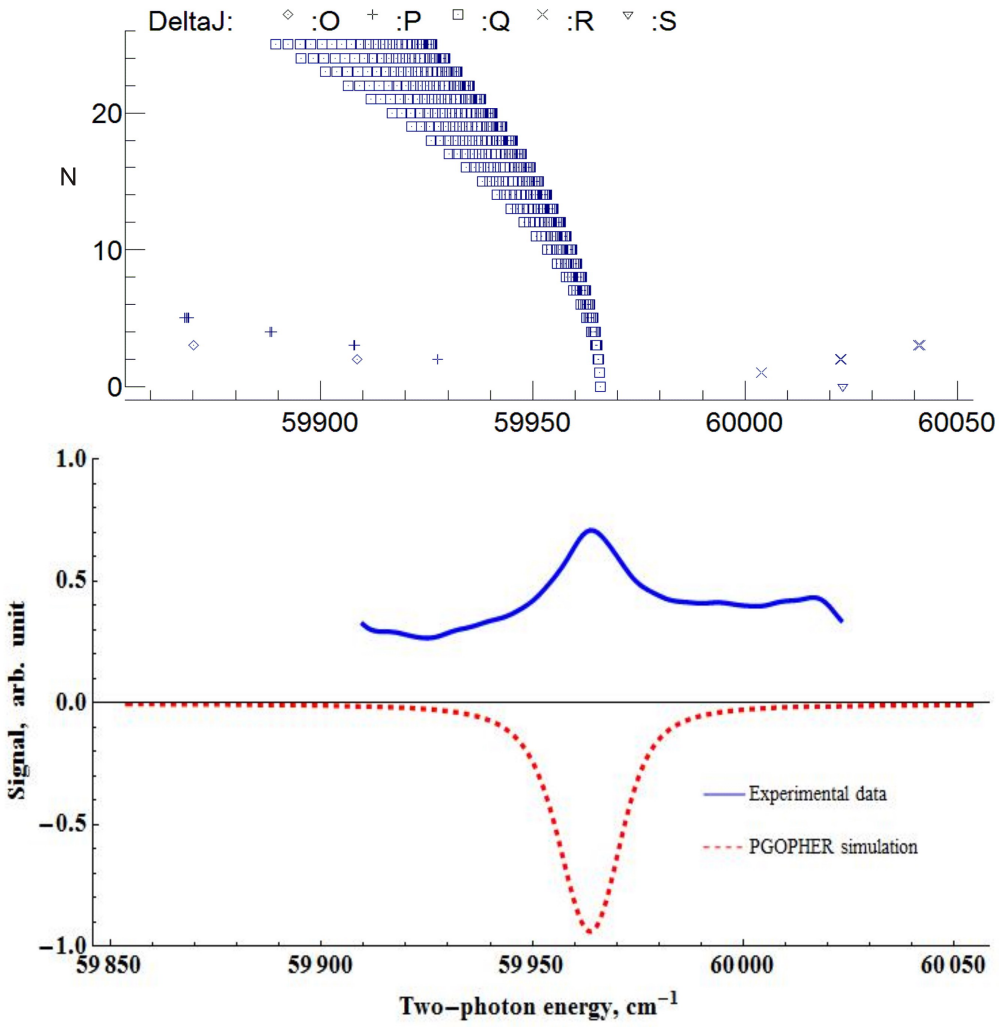

Figure 3.17: Experimental data (blue-solid curve in the bottom panel) and PGOPHER simulation (red-dashed curve in the bottom panel) of CH_3 $3p\ ^2A_2'' \leftarrow 2p\ ^2A_2''$ 0_0^0 REMPI spectrum from 248 nm dissociation of allyl. The top panel shows the PGOPHER assignments of the rotational transition branches.

3.2.7 CH_3 Fragment with higher ν_2 vibrations

CH_3 with ν_2 = 1 and 2 were observed in the 2+1 REMPI studies of 248 nm dissociation of CH_3I in Figures 3.6 and 3.7; and as expected based on previously published measurements,[25] they were a lot weaker than the 0_0^0 REMPI transition. We measured the same 2+1 REMPI spectrum of CH_3 with ν_2 = 1 from 248 nm dissociation of allyl in Fig. 3.14, and the signal to noise ratio turned out to be even lower than that of the CH_3I dissociation. Thus no meaningful analysis by PGOPHER can be made with this low S/N ratio.

No PBASEX resolvable CH_3 ν_2 = 1 velocity mapped images from 248 nm dissociation of allyl has been collected after numerous attempts with different combination of REMPI laser power and focus. It is thus even more difficult to collect the CH_3 ν_2 = 2 images from allyl dissociation.

3.2.8 The Acetylene Fragment

In Sec. 3.2.4 we calculated the experimentally observed CH_3 $\nu_2 = 0$ with KER $\approx$ 40.5 kcal/mole and TKER $\approx$ 63.9 kcal/mole. These values lead us to the C_2H_2 KER of ~23.4 kcal/mole (conservation of translational momentum) and total available internal energy for both fragments of ~3.24 kcal/mole (248 nm photon energy minus TKER minus C$\cdots$C bond energy). Without pinpointing the actual internal energy held by CH_3, which could possibly be distributed in other various vibrational modes than ν_2, we can not reach a definite conclusion of how much internal energy the C_2H_2 fragment possesses. However, even we assume no internal energy being held by CH_3, there is still not much internal energy available for C_2H_2. It would be ideal if we could probe CH_3 in all of the different vibrational states in the VMI experiment and reconstruct the kinetic distribution obtained in Rome, which eventually would lead us to the internal energy distribution for C_2H_2. Nevertheless, based on the available $\nu_2 = 0$ VMI data, we found that internally cold CH_3 was produced in coincidence with internally cold C_2H_2, and all of the available energy was deposited into the kinetic degree of freedom.

CHAPTER 4

CONCLUSION

4.1 Conclusion for the Trajectory Simulations

An accurate and complete potential energy surface, which includes all the possible transition structure that a given initial state can have access to in running a trajectory simulation, certainly can help one understand the experimentally observed unusual phenomenon. If the allyl ground PES had not been complete, *i.e.* if vinylidene had not been included in the construction process of the PES, our simulation would have not explained the observed energy distribution which contradicted the RRKM prediction. For the methyl elimination channel of allyl dissociation on the electronic ground PES, both 1,3 and double 1,2 hydrogen shift mechanisms are indeed important, and so is the vinylidene mechanism. We now understand that this previously neglected route to products was the cause of the difference in kinetic energy distributions experimentally observed in Rome. Although the threshold for the vinylidene route is higher than those for the other mechanisms, it still plays an important role because the transition state is relatively loose. The experiment in Rome used 248 nm excitation to study allyl dissociation because allyl has a relatively high absorption cross section around this wavelength; however, if it were possible to have allyl excited by a higher energy photon, the observed kinetic energy distributions would be even more different due to the dominance of the vinylidene mechanism, as the results of our trajectory simulation would predict. It is also clear from the present study that the role of high-energy isomers of stable molecules should be kept in mind when interpreting the high-energy dissociation processes.

Results of the hydrogen elimination channel simulations can be found in the article published in the *Journal of Physical Chemistry A* and noted in Section 2.1.

4.2 Conclusion for the Velocity-Map-Imaging Experiment

We designed this velocity map imaging experiment on CH_3 fragment from 248 nm dissociation of allyl for two major purposes: (1) to investigate the angular distribution of CH_3 dissociated from rotationally cooled allyl and (2) to monitor CH_3 fragments with different internal energy in the ν_2 out-of-plane bending mode. The spectrum of 266 nm photolytically generated allyl radical was fitted theoretically to be at rotational temperature of ≤ 20 K. The CH_3 $\nu_2 = 0$ images collected were proved to be dependent on all of the three (photolysis, dissociation and probing) lasers. Anisotropy of the CH_3 fragment was first observed experimentally from this cold source of allyl, in comparison to the isotropic results previously reported from experiments with hot (~264K) pyrolytically generated allyl.

Both literature and our preparatory study showed that CH_3 has a strong 2+1 0_0^0 but rather weak 2_1^1 and 2_2^2 REMPI transitions. No resolvable velocity mapped images of CH_3 $\nu_2 = 1$ or 2 have be successfully collected. The CH_3 $\nu_2 = 0$ images gave a very high kinetic energy distribution, which indicated that internally cold CH_3 was produced in coincidence with internally cold C_2H_2. Comparing this observation with the kinetic distribution collected in Rome, it was conceivable that the population of CH_3 $\nu_2 = 0$ was rather small as one would expect CH_3 to dissociate from allyl in high ν_2 modes. It was the ionization process that limited us to detect these CH_3 with higher internal energy by proper ionization.

REMPI spectrum of CH_3 $\nu_2 = 0$ from 248 nm dissociation of allyl were collected and theoretically fitted. The experimental CH_3 $\nu_2 = 0$ rotational distribution peaked at $J \approx 6$, which was comparable to the trajectory prediction of peaking at $J \approx 10$.

REFERENCES

[1] Tulloch, J.; Macpherson, M.; Morgan, C.; Pilling, M. *J. Phys. Chem.* **1982**, *86*, 3812–3819.

[2] Marinov, N.; Pitz, W.; Westbrook, C.; Castaldi, M.; Senkan, S. *Combust. Sci. Technol.* **1996**, *116*, 211–287.

[3] Fernandes, R.; Giri, B.; Hippler, H.; Kachiani, C.; Striebel, F. *J. Phys. Chem. A* **2005**, *109*, 1063–1070.

[4] Nonhebel, D.; Walton, J. *Free-radical chemistry; structure and mechanism*; Cambridge University Press, 1974.

[5] Hucknall, D. *Chemistry of hydrocarbon combustion*; Chapman & Hall, 1985.

[6] Fischer, I.; Chen, P. *J. Phys. Chem. A* **2002**, *106*, 4291–4300.

[7] DeSain, J.; Thompson, R.; Sharma, S.; Curl, R. *J. Chem. Phys.* **1998**, *109*, 7803–7809.

[8] Uy, D.; Davis, S.; Nesbitt, D. *J. Chem. Phys.* **1998**, *109*, 7793.

[9] Currie, C.; Ramsay, D. *J. Chem. Phys.* **1966**, *45*, 488.

[10] Castiglioni, L.; Bach, A.; Chen, P. *Phys. Chem. Chem. Phys.* **2006**, *8*, 2591–2598.

[11] Hudgens, J.; Dulcey, C. *J. Phys. Chem.* **1985**, *89*, 1505–1509.

[12] Sappey, A.; Weisshaar, J. *J. Phys. Chem.* **1987**, *91*, 3731–3736.

[13] Minsek, D.; Chen, P. *J. Phys. Chem.* **1993**, *97*, 13375–13379.

[14] Callear, A.; Lee, H. *Trans. Faraday Soc.* **1968**, *64*, 308–316.

[15] Minsek, D.; Blush, J.; Chen, P. *J. Phys. Chem.* **1992**, *96*, 2025–2027.

[16] Gasser, M.; Frey, J.; Hostettler, J.; Bach, A.; Chen, P. *J. Phys. Chem. A* **2010**, *114*, 4704–4711.

[17] Gasser, M.; Schulenburg, A.; Dietiker, P.; Bach, A.; Merkt, F.; Chen, P. *J. Chem. Phys.* **2009**, *131*, 014304.

[18] Bunker, P. R.; Jensen, P. *Molecular Symmetry and Spectroscopy*, 2nd ed.; NRC Research Press, Canada, 1998.

[19] Stranges, D.; Stemmler, M.; Yang, X.; Chesko, J.; Suits, A.; Lee, Y. *J. Chem. Phys.* **1998**, *109*, 5372.

[20] Stranges, D.; OKeeffe, P.; Scotti, G.; Di Santo, R.; Houston, P. *J. Chem. Phys.* **2008**, *128*, 151101.

[21] Schultz, T.; Fischer, I. *J. Chem. Phys.* **1997**, *107*, 8197.

[22] Deyerl, H.; Fischer, I.; Chen, P. *J. Chem. Phys.* **1999**, *110*, 1450.

[23] Davis, S.; Law, C.; Wang, H. *J. Phys. Chem. A* **1999**, *103*, 5889–5899.

[24] Baer, T.; Hase, W. *Unimolecular Reaction Dynamics: Theory and Experiments*; Oxford University Press, USA, 1996.

[25] Ogorzalek Loo, R.; Haerri, H.; Hall, G.; Houston, P. *J. Chem. Phys.* **1989**, *90*, 4222.

[26] Hase, W. L.; Duchovic, R. J.; Hu, X.; Komornicki, A.; Lim, K. F.; Lu, D.; Peslherbe, G. H.; Swamy, K. N.; Linde, S. R. V.; Varandas, A. et al.Hase, W. L. and Duchovic, R. J. and Hu, X. and Komornicki, A. and Lim, K. F. and Lu, D. and Peslherbe, G. H. and Swamy, K. N. and Linde, S. R. V. and Varandas, A. and others *QCPE Bull* **1996**, *16*, 43.

[27] Bylaska, E. J.; de Jong, W. A.; Govind, N.; Kowalski, K.; Straatsma, T. P.; Valiev, M.; Wang, D.; Apra, E.; Windus, T. L.; Hammond, J. et al.Bylaska, E. J. and de Jong, W. A. and Govind, N. and Kowalski, K. and Straatsma, T. P. and Valiev, M. and Wang, D. and Apra, E. and Windus, T. L. and Hammond, J. and others *Pacific Northwest National Laboratory, Richland, Washington* **2007**, 99352–0999.

[28] Chandler, D.; Houston, P. *J. Chem. Phys.* **1987**, *87*, 1445.

[29] Eppink, A.; Parker, D. *Rev. Sci. Instrum.* **1997**, *68*, 3477.

[30] *Imaging in Molecular Dynamics: Technology and Applications: A user's Guide*; Whitaker, B., Ed.; Cambridge University Press, UK, 2003.

[31] Schmiedl, R.; Dugan, H.; Meier, W.; Welge, K. *Z. Phys. A.* **1982**, *304*, 137–142.

[32] Garcia, G. A.; Nahon, L.; Powis, I. *Rev. Sci. Instrum.* **2004**, *75*, 4989.

[33] Dribinski, V.; Ossadtchi, A.; Mandelshtam, V. A.; Reisler, H. *Rev. Sci. Instrum.* **2002**, *73*, 2634.

[34] Zare, R. N.; Herschbach, D. R. *Proc. IEEE* **1963**, *51*, 173–182.

[35] Zare, R. N. *Mol. Photochem.* **1972**, *4*, 1.

[36] Bersohn, R. What Have We Learned from β ? *ACS SYMPOSIUM SERIES*, 2001; pp 19–33.

[37] Houston, P. L. *J. Phys. Chem.* **1987**, *91*, 5388–5397.

[38] Houston, P. L. *Acc. Chem. Res.* **1989**, *22*, 309–314.

[39] Hall, G. E.; Houston, P. L. *Annu. Rev. Phys. Chem.* **1989**, *40*, 375–405.

[40] Dixon, R. *J. Chem. Phys.* **1986**, *85*, 1866.

[41] Hall, G. E.; Sivakumar, N.; Chawla, D.; Houston, P. L.; Burak, I. *J. Chem. Phys.* **1988**, *88*, 3682.

[42] Eppink, A.; Parker, D.; Janssen, M.; Buijsse, B.; Van der Zande, W. *J. Chem. Phys.* **1998**, *108*, 1305.

[43] Brown, A.; Braams, B.; Christoffel, K.; Jin, Z.; Bowman, J. *J. Chem. Phys.* **2003**, *119*, 8790.

[44] Huang, X.; Braams, B.; Bowman, J. *J. Chem. Phys.* **2005**, *122*, 044308.

[45] Xie, Z.; Braams, B.; Bowman, J. *J. Chem. Phys.* **2005**, *122*, 224307.

[46] Werner, H.-J. et al. *MOLPRO, version 2006.1, a package of ab initio programs*, 2006.

[47] Chang, N.; Shen, M.; Yu, C. *J. Chem. Phys.* **1997**, *106*, 3237.

[48] Shepler, B.; Braams, B.; Bowman, J. *J. Phys. Chem. A.* **2008**, *112*, 9344.

[49] Zare, R. N. *Angular momentum*; Wiley New York, 1988.

[50] Deyerl, H.; Gilbert, T.; Fischer, I.; Chen, P. *J. Chem. Phys.* **1997**, *107*, 3329.

[51] Houston, P. L. *Chemical kinetics and reaction dynamics*; McGraw-Hill New York, 2001.

[52] Blush, J.; Minsek, D.; Chen, P. *J. Phys. Chem.* **1992**, *96*, 10150–10154.

[53] Townsend, D.; Lahankar, S.; Lee, S.; Chambreau, S.; Suits, A.; Zhang, X.; Rheinecker, J.; Harding, L.; Bowman, J. *Science* **2004**, *306*, 1158.

[54] Bowman, J.; Zhang, X. *Phys. Chem. Chem. Phys.* **2005**, *8*, 321–332.

[55] Suits, A. *Acc. Chem. Res* **2008**, *41*, 873–881.

[56] Goncharov, V.; Lahankar, S.; Farnum, J.; Bowman, J.; Suits, A. *J. Phys. Chem. A.* **2009**, *113*, 15315–15319.

[57] Houston, P.; Kable, S. *Proc. Natl. Acad. Sci. U.S.A.* **2006**, *103*, 16079.

[58] Bowman, J. *Proc. Natl. Acad. Sci. U.S.A.* **2006**, *103*, 16061.

[59] Rubio-Lago, L.; Amaral, G.; Arregui, A.; Izquierdo, J.; Wang, F.; Zaouris, D.; Kitsopoulos, T.; Banares, L. *Phys. Chem. Chem. Phys.* **2007**, *9*, 6123–6127.

[60] Heazlewood, B.; Jordan, M.; Kable, S.; Selby, T.; Osborn, D.; Shepler, B.; Braams, B.; Bowman, J. *Proc. Natl. Acad. Sci. U.S.A.* **2008**, *105*, 12719.

[61] Harding, L.; Georgievskii, Y.; Klippenstein, S. *J. Phys. Chem. A.* **2009**, *114*, 765–777.

[62] Western, C. *PGOPHER, a program for simulating rotational structure*, University of Bristol, 2007.

[63] Wolfram Research Inc., *Mathematica: Version 7.0*, Champaign, IL, 2008.

[64] Eppink, A.; Parker, D. *J. Chem. Phys.* **1999**, *110*, 832.

[65] Continetti, R. E.; Balko, B. A.; Lee, Y. T. *J. Chem. Phys.* **1988**, *89*, 3383–3384.

[66] Janssen, M.; Parker, D.; Sitz, G.; Stolte, S.; Chandler, D. *J. Phys. Chem.* **1991**, *95*, 8007–8013.

[67] Chandler, D. et al.Chandler, D.W. and others *Chem. Phys. Lett.* **1989**, *156*, 151–158.

[68] `http://www.ccmst.gatech.edu/wiki/`, Accessed Feb. 2011.

[69] Kayser Jr, R.; Kilpatrick, J. *J. Chem. Phys.* **1978**, *68*, 1511.

[70] Hudgens, J.; DiGiuseppe, T.; Lin, M. *J. Chem. Phys.* **1983**, *79*, 571.

[71] Jacox, M. *Journal of Physical and Chemical Reference Data* **2003**, *32*, 1.